2017

IMPROVEMENTS IN INVERTER MODELING AND CONTROL

Xiao Liu
University of Kentucky, xiaol457@gmail.com
Digital Object Identifier: https://doi.org/10.13023/ETD.2017.332

STUDENT AGREEMENT:

I represent that my thesis or dissertation and abstract are my original work. Proper attribution has been given to all outside sources. I understand that I am solely responsible for obtaining any needed copyright permissions. I have obtained needed written permission statement(s) from the owner(s) of each third-party copyrighted matter to be included in my work, allowing electronic distribution (if such use is not permitted by the fair use doctrine) which will be submitted to UKnowledge as Additional File.

I hereby grant to The University of Kentucky and its agents the irrevocable, non-exclusive, and royalty-free license to archive and make accessible my work in whole or in part in all forms of media, now or hereafter known. I agree that the document mentioned above may be made available immediately for worldwide access unless an embargo applies.

I retain all other ownership rights to the copyright of my work. I also retain the right to use in future works (such as articles or books) all or part of my work. I understand that I am free to register the copyright to my work.

REVIEW, APPROVAL AND ACCEPTANCE

The document mentioned above has been reviewed and accepted by the student's advisor, on behalf of the advisory committee, and by the Director of Graduate Studies (DGS), on behalf of the program; we verify that this is the final, approved version of the student's thesis including all changes required by the advisory committee. The undersigned agree to abide by the statements above.

Xiao Liu, Student

Dr. Aaron M. Cramer, Major Professor

Dr. Caicheng Lu, Director of Graduate Studies

Improvements in Inverter Modeling and Control

DISSERTATION

A dissertation submitted in partial fulfillment of the
requirement for the degree of Doctor of Philosophy in the
College of Engineering at the University of Kentucky

By

Xiao Liu

Lexington, Kentucky

Director: Dr. Aaron M. Cramer, Associate Professor of Electrical Engineering

Lexington, Kentucky

2017

ABSTRACT OF DISSERTATION

Improvements in Inverter Modeling and Control

In this dissertation, the generalized averaging method models for inverters, reactive power control methods for photovoltaic inverters, and a noise immunity improvement for hybrid position observers for brushless dc motor drives are studied.

Models of inverters and other converters based on averaging have been widely used in numerous simulation applications. Generalized averaging can be applied to model both average and switching behavior of converters while retaining the faster run times associated with average-value models. Herein, generalized average models for single- and three-phase pulse width modulation inverters are proposed. The modulation signal for the proposed model could be either a sinusoidal waveform without high order harmonics or a sinusoidal waveform with third-harmonic injection. And this generalized average models also can apply for modeling three-phase pulse width modulation inverters with varying modulation signal frequency in the reference frame. These models are based on a quasi-Fourier series representation of the switching functions that includes fundamental and switching frequency components as well as sideband components of the switching frequency. The proposed models are demonstrated both in simulation and experimentally and are found to accurately portray both the fundamental and the switching behavior of the inverter. In particular, the use of sideband components allows accurate representation of the variation in switching ripple magnitude that occurs in the steady state. The generalized average models are found to have simulation run times that are significantly faster than those associated with detailed models. Therefore, the proposed generalized average models are suitable for simulation applications in which both accuracy (including the switching behavior) and fast run times are required (e.g., long simulation times, systems with multiple converters, and repeated simulations).

Variations in the output power of intermittent renewable sources can cause significant fluctuations of distribution system voltage magnitudes. Reactive power control methods that employ the reactive power capability of photovoltaic three-phase inverters to mitigate these fluctuations are proposed. These control methods cause the three-phase inverters to substitute reactive output power for real output power when fluctuations in the solar power are experienced, allowing the fluctuations to be controlled. Performance metrics for assessing the ability of these controllers to

perform this mitigation are defined. The controllers are examined using the IEEE 123-bus feeder distribution system, and it is found that the controllers can effectively mitigate voltage magnitude fluctuations and that the appropriate choice of controller depends on the performance metrics of interest.

Finally, a noise immunity improvement for hybrid position observers for brushless dc motor drives is proposed. A finite state machine is used to detect Hall-effect sensor transitions to determine if these transitions are true transitions or the result of momentary glitches. This filter causes a delay in the detection of the Hall-effect sensors that is compensated in the proposed observer. The proposed observer is compared in simulations with the original hybrid position observer under both non-noisy and noisy conditions for both constant and variable speed operation, and it has good performance even under high noise and variable speed conditions.

KEYWORDS: inverter, mathematical model, distributed power generation, reactive power control, brushless dc motor drive, observer

Xiao Liu

July 26^{th}, 2017

Improvements in Inverter Modeling and Control

By

Xiao Liu

Aaron M. Cramer
Director of Dissertation

Caicheng Lu
Director of Graduate Studies

July 26^{th}, 2017
Date

In memory of my grandfather, Zhiming Liu and my grandmother, Wanhua Xiong.

Acknowledgements

I would like to thank my parents, my wife, and my son for their love.

I would like to thank my advisor Prof. Cramer for his encouragement and inspiration. Without his patience, I would not make so much progress in my Ph.D. program.

I would like to thank Prof. Walcott for his enlightenment in the control theory.

I would like to thank my committees Prof. Liao and Prof. Sottile for their insightful comments.

I would like to thank my outside examiner Prof. Renfro for his valuable time.

I would like to thank Prof. Ionel for his professional suggestions.

I would like to thank my fellow colleagues Fei Pan, Hanling Chen, Mengmei Liu and Yuqi Zhang for their help for the lab experiments.

This work was funded in part by the Office of Naval Research (ONR) through the United States Naval Academy, N00189-14-P-1197, and through the ONR Young Investigator Program, N00014-15-1-2475, and by the Southeastern Center for Electrical Engineering Education, SCEEE-14-003.

Contents

List of Tables

List of Figures

Chapter 1

Introduction

1.1 Introduction

The pulse width modulation (PWM) inverter has been widely used in renewable energy integration [1–4], motor drive [5–8], and other applications (e.g., [9]). The PWM inverter can transfer the dc to the ac by controlling the switching devices in the circuit. Models are necessary for analyzing the dynamic behavior of inverters in different simulation applications. Various controllers are designed for inverters to meet different requirements of the steady-state and dynamic behavior.

Models of inverters and other converters based on averaging have been developed for numerous simulation applications. Detailed models represent every switching action of an inverter, resulting in very accurate simulation results. However, the simulation of such models is time consuming because the simulation time step is limited by the switching period of the inverter. This can be particularly problematic when systems require long simulation times, contain large numbers of power converters, and/or require many repeated simulations with different parameters, e.g., simulating a photovoltaic (PV) inverter system over the interval of a cloud transient [10], simulating multi-converter systems such as electrical railway systems [11], shipboard power

systems [12], distribution systems with high penetrations of renewable energy generation [13], and microgrids with many power converters [14], or parameter tuning by genetic algorithm [15]. Furthermore, the detailed models of power converter are time-varying systems without stationary equilibrium points, which makes them generally unsuitable for controller design. Models based on state-space averaging (SSA) [16] can reduce the run time of the simulation by replacing the switching function with its fast average. SSA is a very common approach for modeling power electronic circuits [17, 18] and is a useful tool for controller design [19, 20]. However, the improved run times available from SSA models come at the cost of reduced model accuracy. In particular, such models are incapable of representing the switching ripple present in the inverter. Models based on the generalized averaging method (GAM) use a quasi-Fourier series (QFS) representation of waveforms in order to represent both the fundamental behavior and the switching harmonics. GAM models represent a compromise between the high model fidelity available from detailed models and the fast simulation run times available with SSA models. Such models make it possible to investigate the steady-state and dynamic characteristics of the switching ripple without incurring the runtime penalty associated with detailed models, making them particularly appropriate in the cases mentioned above (i.e., long simulation times, systems with multiple converters, and repeated simulations). In this dissertation, the GAM is extended to model PWM inverters including both their fundamental and switching behavior. QFS representations for the switching functions of PWM inverters are used to construct GAM models of single- and three-phase inverters. In the proposed GAM models, the state variables are represented using not only the fundamental component of the modulation signal and components corresponding to multiples of the switching frequency, but also sideband components of multiples of the switching frequency.

The third-harmonic injection is used in the modulation signal for the three-phase inverters to increase the inverter maximum output voltage while avoiding overmodulation, which results in undesirable low-frequency harmonics. Third-harmonic injection does not change the fundamental component of the switching frequency components in a balanced three-phase system, but it changes the higher-order harmonics. As a result, the QFS representation of the switching functions for the three-phase inverter with third-harmonic injection must include the third harmonics. In this dissertation, the GAM is also extended to model three-phase PWM inverters with third-harmonic injection.

The reference frame is used to analyze the electric machine and inverter systems [21–24]. By transferring *abc* variables to the reference frame, time-varying inductances of the electrical machines can be eliminated and ac variables can be converted to dc variables [25]. In this dissertation, the GAM is also extended to model three-phase PWM inverters in the reference frame with varying modulation signal frequency. In a balanced three-phase system, it can be found that the reference frame transformation does not change the magnitude of the harmonic components, but it changes the frequency of the harmonic components in the reference frame. The QFS representation of the switching functions in the reference frame is derived from that for *abc* variables and used to construct the GAM model for three-phase inverters in the reference frame.

There are significant technical challenges at every level associated with the integration of renewable energy sources. One significant challenge is managing variations in distribution system voltage magnitudes caused by fluctuations in the output power of intermittent sources such as PV generation. Distributed generation can cause the voltage magnitudes in distribution systems to rise. However, the output power of these sources can fluctuate rapidly. For example, PV sources use maximum power point tracking (MPPT) to make most effective use of the incident sunlight. Conse-

quently, the output power of such sources can vary rapidly in response to passing clouds. Irradiance changes of as much as 60% per second have been observed during such cloud transients [26, 27]. These transients can have significant impacts on the voltage magnitudes in distribution systems, and these impacts can be expected to increase with increasing renewable penetration. Such transients also occur too rapidly for traditional distribution system regulation equipment, such as tap changing transformers and switched capacitor banks, to respond to them in an appropriate manner. Herein, various reactive power control methods are studied in which the PV inverter responds to variations in its real power output by varying its reactive power output. The control methods involve the inverter substituting reactive power production for real power production when solar power changes.

The High-performance operation of brushless dc motors with sinusoidal references requires knowledge of the electrical rotor position with relatively high accuracy. Electromagnetic resolvers and optical encoders can provide sufficient position accuracy, but they require larger installation volumes and entail higher costs. Much work has be conducted on sensorless drive techniques (e.g., [28–32]). Generally, sensorless techniques require detailed motor parameters [28], and the initial rotor position must be estimated for startup [29]. Hall-effect sensors are widely installed in brushless dc motors and provide a reliable and cheap way to obtain the electrical rotor position. Observers have been developed to find the electrical rotor position based on binary Hall-effect sensors [33–36]. However, this observer can not find the correct electrical rotor position if there is a short sensor glitch. Herein, a noise immunity improvement for the hybrid position observer is proposed to address experimentally observed Hall-effect sensor noise.

1.2 Thesis Outline

The remainder of this dissertation is organized as follows: Chapter 2 described the background and literature review about the inverter modeling and control. In Chapter 3, the GAM models for the single- and three-phase inverters with sinusoidal modulation signal are described. In Chapter 4, the GAM is applied to model the three-phase inverter with third-harmonic injection in the modulation signal. In Chapter 5, the GAM models for the three-phase inverter in the reference frame with varying modulation signal frequency are proposed. The reactive power control methods for the PV inverter system to mitigate the grid voltage magnitude fluctuations due to solar power variation are discussed in Chapter 6. The noise immunity improvement for the hybrid position observer is discussed in Chapter 7. Conclusions and avenues of future work are discussed in Chapter 8.

Chapter 2

Background and Literature Review

This chapter gives the background information on the PWM, single- and three-phase inverters, and reference frame theory. The existing inverter models, reactive power control methods for renewable source integration, and rotor position observers are also discussed in the following sections.

2.1 Pulse Width Modulation

PWM is used to generate the switching signal for the voltage-source inverters. It compares the duty cycle $d(t)$ with the PWM carrier signal $c(t)$ to generate the switching function $q(t)$. The PWM carrier signal could be a sawtooth waveform or triangular waveform. The duty cycle could be naturally sampled or regular sampled. For the naturally sampled PWM with triangular carrier, whenever the value of $d(t)$ is larger than the PWM carrier signal $c(t)$, the switching function $q(t)$ is equal to 1; otherwise, the switching function $q(t)$ is equal to 0. Normally, the frequency of PWM carrier signal is much larger than that of modulation single. So, the switching function generated by the PWM has fundamental harmonic components and switching frequency harmonic components.

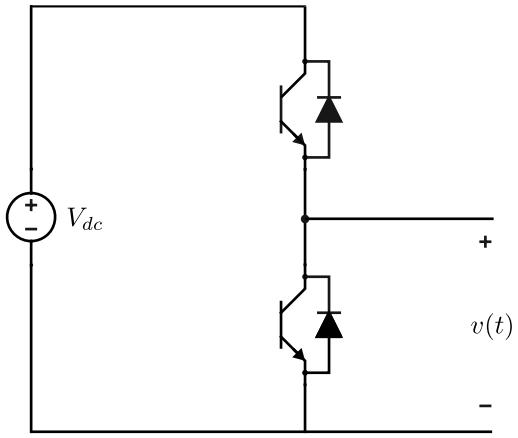

Figure 2.1: Inverter branch

2.2 Single-Phase and Three-Phase Inverter

As mentioned in Chapter 1, inverters are widely used in the renewable energy integration, motor drive, and other applications. It can convert the dc to the ac by turning on and off the switching devices. One branch for inverter is shown in Figure 2.1. It can be seen that there are two switches for this branch. For each branch, only one switch can be on at the same time. Otherwise, the voltage source is shorted which can cause damage to the circuit. If two switches are ideal switches, the output voltage $v(t)$ for a single branch is equal to dc source voltage when the upper power switch is on and is equal to zero when the lower switch in on. So, the output voltage of a single branch can be given by

$$v(t) = V_{dc}q(t). \tag{2.1}$$

The single-phase full-bridge inverter is shown in Figure 2.2. It can be seen that the single-phase full-bridge inverter has two branches. A load is connected to the output of the single-phase full-bridge inverter. The output voltage of the single-phase full-bridge inverter can be found by

$$v(t) = V_{dc}\left(q_{+}(t) - q_{-}(t)\right), \tag{2.2}$$

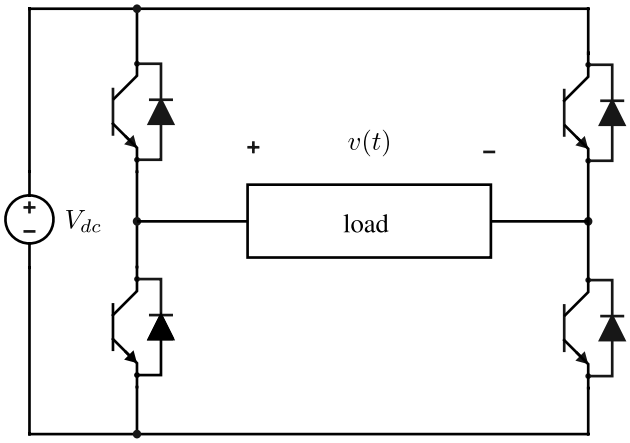

Figure 2.2: Single-phase full-bridge inverter

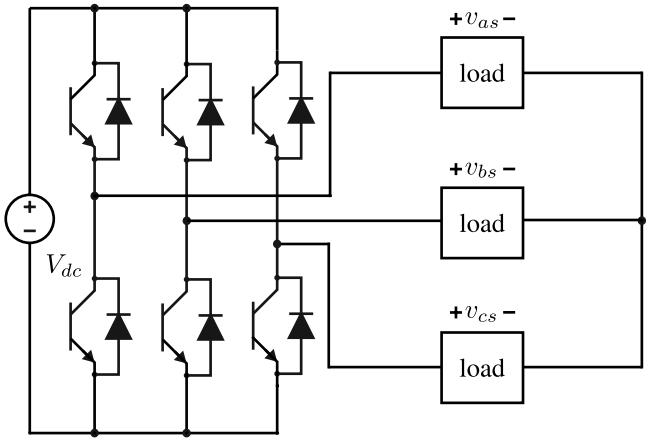

Figure 2.3: Three-phase inverter

where $q_+(t)$ is the switching function of the left branch and $q_-(t)$ is the switching function of the right branch. It is noticed that $v(t)$ can vary from $-V_{dc}$ to V_{dc}. As a result, by changing the duty cycle, the altering current can be generated on the load.

The three-phase inverter is shown in Figure 2.3. It can be seen that the three-phase inverter has three branches. A three-phase load is connected to the output of the three-phase inverter. The three-phase line-to-ground output voltages can be

found by

$$v_{ag}(t) = V_{dc} q_a(t) \tag{2.3}$$

$$v_{bg}(t) = V_{dc} q_b(t) \tag{2.4}$$

$$v_{cg}(t) = V_{dc} q_c(t), \tag{2.5}$$

where $q_a(t)$, $q_b(t)$, and $q_c(t)$ are the three-phase switching functions. By using KVL, the relationship among the three-phase line-to-neutral voltages, three-phase line-to-ground voltages, and neutral-to-ground voltage can be found by

$$v_{as}(t) = v_{ag}(t) - v_{ng} \tag{2.6}$$

$$v_{bs}(t) = v_{bg}(t) - v_{ng} \tag{2.7}$$

$$v_{cs}(t) = v_{cg}(t) - v_{ng}, \tag{2.8}$$

where v_{ng} is the neutral-to-ground voltage. If the three-phase system is balanced, the sum of three-phase line-to-neutral output voltages is equal to zero. By adding (2.6), (2.7), and (2.8), the neutral-to-ground voltage v_{ng} can be found by

$$v_{ng} = \frac{v_{ag}(t) + v_{bg}(t) + v_{cg}(t)}{3}. \tag{2.9}$$

So, the line-to-neutral output voltage can be calculated from the switching function and dc source voltage as the following equations:

$$v_{as}(t) = V_{dc} \left(\frac{2}{3} q_a(t) - \frac{1}{3} q_b(t) - \frac{1}{3} q_c(t) \right) \tag{2.10}$$

$$v_{bs}(t) = V_{dc} \left(\frac{2}{3} q_b(t) - \frac{1}{3} q_a(t) - \frac{1}{3} q_c(t) \right) \tag{2.11}$$

$$v_{cs}(t) = V_{dc} \left(\frac{2}{3} q_c(t) - \frac{1}{3} q_a(t) - \frac{1}{3} q_b(t) \right). \tag{2.12}$$

2.3 Reference Frame

The reference frame is commonly used for inverter controller design [37–40]. In the three-phase system, the three-phase waveforms can be transferred to an arbitrary reference frame by using the transformation matrix. Those waveforms could be three-phase switching functions, voltages, and currents. For a given three-phase waveforms f_a, f_b, and f_c, their value in the reference frame can be found by

$$\begin{bmatrix} f_q \\ f_d \\ f_0 \end{bmatrix} = \mathbf{K} \begin{bmatrix} f_a \\ f_b \\ f_c \end{bmatrix}. \tag{2.13}$$

The transformation matrix $\mathbf{K}$ is given by

$$\mathbf{K} = \frac{2}{3} \begin{bmatrix} \cos(\theta(t)) & \cos(\theta(t) - \frac{2\pi}{3}) & \cos(\theta(t) + \frac{2\pi}{3}) \\ \sin(\theta(t)) & \sin(\theta(t) - \frac{2\pi}{3}) & \sin(\theta(t) + \frac{2\pi}{3}) \\ \frac{1}{2} & \frac{1}{2} & \frac{1}{2} \end{bmatrix}, \tag{2.14}$$

where

$$\theta(t) = \int_0^t \omega(t)dt + \phi_0. \tag{2.15}$$

The stationary reference frame, rotor reference frame, and synchronous reference frame are the three commonly used reference frames. The angular frequency $\omega(t)$ of the stationary reference frame, rotor reference frame, and synchronous reference frame are equal to 0, rotor angular velocity, electrical angular velocity, respectively.

2.4 Inverter Modeling

Different inverter models have been developed for different circuit topologies and simulation applications [41–44]. These models are useful tools for analyzing and

predicting the dynamic behavior of the inverter. Examples include using models to analyze inverter power loss [41] and to design feedback controllers for grid-tie inverters [42]. To overcome the difficulties associated with detailed models (i.e., slower run times and lack of stationary equilibrium points), SSA models have been applied to a variety of types of converters [45–48]. Such an approach has its limitations with respect to inverter modeling. The cross-coupling effect of the switching ripple can cause offsets in the lower frequency components of state variables [49, 50], and it is possible that the switching ripple can be resonantly amplified in the LCL filter of a grid-tie inverter system. Furthermore, the effect of the PWM is not considered in SSA models, e.g., a low-order harmonic can be produced in the inverter with uniformly sampled PWM [51]. In [52], an average-value model with switching ripple estimation is discussed. However, the switching ripple must be calculated by an iterative algorithm for each switching cycle, and the time step of this average-value model is still limited by the switching frequency.

The GAM has been developed broadly [49, 53–56] with wide application in dc-dc converters. The GAM encompasses conceptually similar ideas, sometimes referred to as generalized SSA and multifrequency averaging, but it can not be applied to model inverters directly. Unlike GAM models for dc-dc converters, the switching functions for the inverters involve two frequencies: the frequency of the sinusoidal modulation signal and the switching frequency associated with the carrier signal. In order to find the GAM model of the inverter, the QFS representation of the switching function for sinusoidal modulation signal is necessary. The Fourier series representation of periodic switching functions of PWM inverter is discussed in [51] and used herein. A GAM-like model for three-phase inverters is proposed in [57], but this model uses a QFS representation for only the fundamental components, neglecting the switching harmonics and producing results analogous to an SSA model. A GAM model for class-E inverters is proposed in [58], but the switching duty cycle is a constant in

steady state for this topology, and, as a result, the state variables in the GAM model only represent the switching harmonics. In [59], a model of a naturally sampled PWM modulator with the non-periodical modulation signal is proposed to reduce simulation run time. In each sampling period, the switching function is represented by a Fourier series approximation based on the sampled modulation signal. However, the sampling frequency of the modulation signal must be much larger than the PWM carrier signal frequency to achieve an accurate result.

2.5 Reactive Power Control Methods for Renewable Source Integration

It is well understood that the reactive power capability of inverter-based distributed generation can be used to improve distribution system operation (e.g., [60–65]). In [66–69], the integration of MPPT with real and reactive power control of the PV inverter is discussed. In [70, 71], the control of reactive power is optimized to reduce the system losses. Reactive power can be dispatched as part of the volt/var control strategy of the distribution system [72–78]. In [79], both real and reactive power are controlled to keep the voltage magnitude in the acceptable range. In [80], a local linear controller is used to inject balanced three-phase reactive power into the grid.

In this dissertation, several reactive power control methods of the form proposed in [80] are proposed. In these methods, the reactive power output is a linear function of the instantaneous solar power. Unlike methods in other studies [81–86], the reactive power controller does not require high-bandwidth communication to improve voltage quality. These methods only require local information in order to function.

2.6 Hall-effect Sensors Based Electrical Rotor Position Observer

Hall-effect sensors are widely installed in brushless dc motors and provide a reliable and cheap way to obtain the electrical rotor position. Observers have been developed to find the electrical rotor position based on binary Hall-effect sensors [33–35]. In [33], a vector-tracking observer with harmonics decoupling is developed, which has good performance in steady state and during transients. However, this method requires a high accuracy estimate of the load torque, is sensitive to the moment of inertia, and needs careful tuning of the observer parameters. In [34], a hybrid observer for high-performance brushless dc motor drives is discussed. Its simple implementation provides a good estimate of the instantaneous rotor position without requiring machine parameter estimates. In [35], a method which is similar to the hybrid observer is proposed: the electrical angle is reset at each Hall-effect sensor transition, and the instantaneous rotor position is estimated by assuming the speed is constant between two Hall-effect sensor transitions.

In [33–35], it is assumed that no fault exists in the output of the Hall-effect sensors. However, it is possible that there are some sensor faults in practice. In particular, high-frequency switching can induce short sensor glitches in brushless dc motor drive systems. Even such short glitches in the output of the Hall-effect sensors can cause large estimation errors, and these errors can persist for a significant interval after the noise is removed. The estimation of the electrical rotor position under sensor faults has been widely studied. In [87], the rotor position can be estimated when there is one or two permanent faults in three Hall-effect sensors. In [88], a periodic timer interrupt function is used to check the output of the Hall-effect sensor to avoid noise between sampling periods. However, a glitch that is longer than one period of the

timer or that occurs at the time when the Hall-effect sensor is sampled can still cause errors in the observer.

Chapter 3

Generalized Average Method for Time-Invariant Modeling of Inverters

In this chapter, GAM is extended to model PWM inverters including both their fundamental and switching behavior. The work described in this chapter has been published in [89]. QFS representations for the switching functions of PWM inverters are used to construct GAM models of single- and three-phase inverters. In the proposed GAM models, the state variables are represented using not only the fundamental component of the modulation signal and components corresponding to multiples of the switching frequency, but also sideband components of multiples of the switching frequency. The proposed models are demonstrated both in simulation and experimentally and are found to accurately portray both the fundamental and the switching behavior of the inverter. Furthermore, the proposed GAM models are time invariant, resulting in state variables that are constant in the steady state and simulation run times that are considerably smaller than those that can be achieved with a detailed model. The contributions of this work are the application of QFS representations

of the switching functions in PWM inverters for constructing GAM models of PWM single- and three-phase inverters and the demonstration of the proposed GAM models in simulation and experimentally.

The remainder of this chapter is organized as follows. The general approach to construct GAM inverter models and the QFS representation of the switching functions of PWM inverters are described in Section 3.1. In Section 3.2, the GAM models for single- and three-phase inverters are proposed, and an estimation technique for assessing the accuracy of such models is discussed. The proposed models are compared with detailed and SSA inverter models in Section 3.3. In Section 3.4, the GAM models are demonstrated by comparing their simulation results with experimentally measured waveforms. Finally, conclusions are drawn in Section 3.5.

3.1 Generalized Averaging Method for Inverters

The general approach for constructing GAM models is as follows. Starting with a system of ordinary differential equations representing a detailed model, a new system of ordinary differential equations is constructed wherein the instantaneous state variables are represented using a QFS representation. In particular, for a PWM inverter, a waveform $x(t)$ is represented as

$$x(t) = x_{0,0} + x_{0,1c}\cos(\bar{\omega}t) + x_{0,1s}\sin(\bar{\omega}t) + \sum_{n=1}^{\infty}\sum_{i=-\infty}^{\infty} x_{n,ic}\cos(n\hat{\omega}t + i\bar{\omega}t) + \sum_{n=1}^{\infty}\sum_{i=-\infty}^{\infty} x_{n,is}\sin(n\hat{\omega}t + i\bar{\omega}t), \quad (3.1)$$

where $\bar{\omega}$ is the angular frequency of the fundamental component and $\hat{\omega}$ is the angular switching frequency. While the waveform $x(t)$ varies with time, each of the coefficients of the QFS representation (e.g., $x_{0,0}$, $x_{n,ic}$, and $x_{n,is}$) are constant in steady state. It is assumed that the waveform can be approximated by index-0, index-n_1i_1c, index-n_1i_1s,

index-$n_2 i_2 c$, index-$n_2 i_2 s$,..., index-$n_o i_o c$, and index-$n_o i_o s$ QFS components, where n_k is the order of the kth selected $\hat{\omega}$ component and i_k is the corresponding order of kth selected $\bar{\omega}$ component for $k \in \{1, 2, \ldots o\}$ and that the unselected harmonic components are negligible. In this case, the waveform $x(t)$ can be represented by an average vector of length $2o + 1$ that is constructed from the QFS coefficients:

$$\mathbf{x} = [x_{0,0}\ x_{n_1,i_1 c}\ x_{n_1,i_1 s}\ \ldots\ x_{n_o,i_o c}\ x_{n_o,i_o s}]^{\mathrm{T}}. \tag{3.2}$$

The instantaneous value of the waveform can be approximated as

$$x(t) \approx \mathbf{C}(t)\mathbf{x}, \tag{3.3}$$

where

$$\mathbf{C}(t) = \begin{bmatrix} 1 \\ \cos(n_1\hat{\omega}t + i_1\bar{\omega}t) \\ \sin(n_1\hat{\omega}t + i_1\bar{\omega}t) \\ \vdots \\ \cos(n_o\hat{\omega}t + i_o\bar{\omega}t) \\ \sin(n_o\hat{\omega}t + i_o\bar{\omega}t) \end{bmatrix}^{\mathrm{T}}. \tag{3.4}$$

A GAM model is a system of ordinary differential equations constructed in terms of these average vectors and their time derivatives.

Certain mathematical properties of signals approximated by QFS representations are straightforward. One necessary property for constructing GAM models is the relationship between the QFS representation of a signal's time derivative and the time derivative of the QFS representation of the signal. The derivative with respect

Table 3.1: Relevant Quasi-Fourier Series Relationships

Instantaneous signal	Average vector
$x(t)$	$\mathbf{x}$
$ax(t)$	$a\mathbf{x}$
$x(t)+y(t)$	$\mathbf{x}+\mathbf{y}$
$\frac{dx(t)}{dt}$	$\left(\mathbf{T}\mathbf{x}+\frac{d\mathbf{x}}{dt}\right)$

to time of a QFS-approximated signal can be given by

$$\begin{aligned}\frac{dx(t)}{dt} &\approx \frac{d}{dt}(\mathbf{C}(t)\mathbf{x}) \\ &= \frac{d\mathbf{C}(t)}{dt}\mathbf{x}+\mathbf{C}(t)\frac{d\mathbf{x}}{dt} \\ &= \mathbf{C}(t)\left(\mathbf{T}\mathbf{x}+\frac{d\mathbf{x}}{dt}\right),\end{aligned} \tag{3.5}$$

where $\mathbf{T}$ is a $(2o+1)\times(2o+1)$ matrix that is constructed such that all elements are zero except for the $(2k, 2k+1)$ elements with values $n_k\hat{\omega}+i_k\bar{\omega}$ and the $(2k+1, 2k)$ elements with values $-(n_k\hat{\omega}+i_k\bar{\omega})$ for $k\in\{1,2,\ldots o\}$. A summary of relevant QFS relationships is given in Table 3.1.

In order to model PWM inverters, a QFS representation of the switching functions of the inverters is necessary. It is assumed that the inverter modulation signal is a sinusoidal waveform without high order harmonics. The modulation signal can be expressed by

$$m(t) = m_{0,1c}\cos(\bar{\omega}t)+m_{0,1s}\sin(\bar{\omega}t), \tag{3.6}$$

where $m_{0,1c}$ and $m_{0,1s}$ are real-valued QFS coefficients. The instantaneous duty cycle can be expressed as

$$d(t) = \frac{1}{2}(m(t)+1). \tag{3.7}$$

The relationship among the PWM carrier $c(t)$, the duty cycle $d(t)$, and the switching function $q(t)$ is shown in Figure 3.1. Whenever the value of $d(t)$ is larger than the

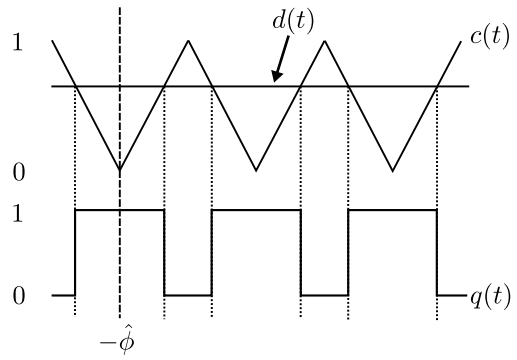

Figure 3.1: Relationship of the PWM carrier, the duty cycle and the switching function

PWM carrier signal, the switching function is equal to 1; otherwise, the switching function is equal to 0.

It has been shown in [53] that for relatively slowly varying duty cycle, the general periodic switching function can be expressed as the following Fourier series:

$$q(t) = d(t) + \frac{2}{\pi}\sum_{n=1}^{\infty}\frac{\sin(n\pi d(t))}{n}\cos(n\hat{\omega}t + n\hat{\phi}), \tag{3.8}$$

where $\hat{\phi}$ is the switching function phase as shown in Figure 3.1. It is assumed that $\bar{\omega} \ll \hat{\omega}$, i.e., that modulation signal changes slowly with respect to the switching frequency. By expanding (3.8), the general QFS representation of the switching function for sinusoidal modulation signals can be expressed by

$$\begin{aligned} q(t) = q_{0,0} + q_{0,1c}\cos(\bar{\omega}t) + q_{0,1s}\sin(\bar{\omega}t) \\ + \sum_{n=1}^{\infty}\sum_{i=-\infty}^{\infty} q_{n,ic}\cos(n\hat{\omega}t + i\bar{\omega}t) \\ + \sum_{n=1}^{\infty}\sum_{i=-\infty}^{\infty} q_{n,is}\sin(n\hat{\omega}t + i\bar{\omega}t), \end{aligned} \tag{3.9}$$

where

$$q_{0,0} = \frac{1}{2} \tag{3.10}$$

$$q_{0,1c} = \frac{1}{2} m_{0,1c} \tag{3.11}$$

$$q_{0,1s} = \frac{1}{2} m_{0,1s} \tag{3.12}$$

$$q_{n,ic} = \frac{2}{n\pi} \sin\left(\frac{\pi(n+i)}{2}\right) J_i(y_n) \cos(n\hat{\phi} + i\bar{\phi}) \tag{3.13}$$

$$q_{n,is} = -\frac{2}{n\pi} \sin\left(\frac{\pi(n+i)}{2}\right) J_i(y_n) \sin(n\hat{\phi} + i\bar{\phi}) \tag{3.14}$$

$$y_n = \frac{n\pi}{2} \sqrt{m_{0,1c}^2 + m_{0,1s}^2} \tag{3.15}$$

$$\bar{\phi} = \arg(m_{0,1c} - j m_{0,1s}). \tag{3.16}$$

The function $J_i(x)$ is the Bessel function of the first kind of integer order i. Similar analyses of the spectral content of PWM waveforms can be found in [51]. It is noted that $\bar{\phi}$ is the modulation signal phase. The coefficients calculated by (3.10)–(3.14) have been found to be highly accurate when $\hat{\omega}/\bar{\omega} \geq 10$. These expressions are valid for naturally sampled PWM, but other modulation techniques have similar QFS representations of their switching functions.

The most significant components of the Fourier spectrum of two switching functions are shown in Figure 3.2. These switching functions, produced when a 10-kHz carrier signal is modulated by two different 60-Hz modulation signals, are sampled at 30 MHz, and discrete Fourier transforms are performed. It can be seen that the high-order harmonic amplitudes change when the magnitude of the modulation signal changes. It is observed from (3.13) and (3.14) that the $q_{n,ic}$ and $q_{n,is}$ terms vanish when the sum $n + i$ is even. As a result, no components at 9.94 kHz, 10.06 kHz, 20 kHz, 19.88 kHz, and 20.12 kHz are present in Figure 3.2. The magnitudes of the components shown in Figure 3.2 correspond to those calculated using (3.10)–(3.14). The

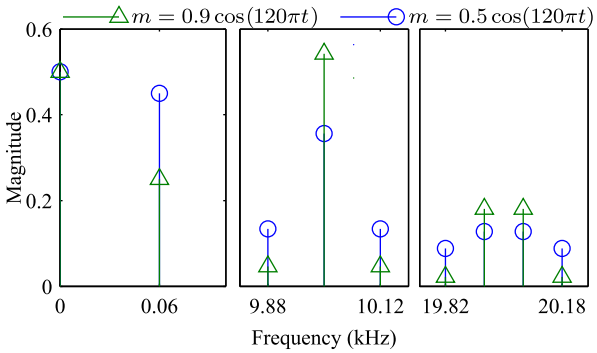

Figure 3.2: Discrete Fourier transform of switching functions

relative magnitudes of the components at different frequencies are used to determine which components are most significant to include in a GAM model.

By combining the properties of QFS-represented signals with the QFS representation of inverter switching functions, it is possible to construct GAM models for various PWM inverter systems as shown in the following section.

3.2 Inverter Generalized Averaging Method Models

The inverter topologies considered herein are described in the subsections below. The topologies span single-phase and three-phase and grid-connected and standalone, and each topology has an output filter. It is noted that the particular filter is not a limiting characteristic of the modeling approach, and GAM models can be easily described for other types of output filter.

3.2.1 Single-phase inverter

The single-phase full bridge inverter with LC filter and resistive load is shown in Figure 3.3. For each switch branch, either the upper or lower switch can be on. The

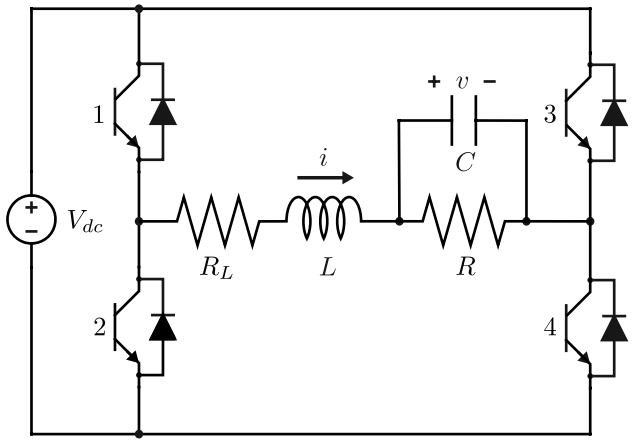

Figure 3.3: Single-phase inverter

state equations for the detailed model are given by

$$\frac{di(t)}{dt} = \frac{V_{dc}}{L}\left(q_+(t) - q_-(t)\right) - \frac{R_L}{L}i(t) - \frac{1}{L}v(t) \tag{3.17}$$

$$\frac{dv(t)}{dt} = \frac{1}{C}i(t) - \frac{1}{RC}v(t), \tag{3.18}$$

where $q_+(t)$ is equal to 1 when switch 1 is on and switch 2 is off and equal to 0 when switch 1 is off and switch 2 is on and where $q_-(t)$ is equal to 1 when switch 3 is on and switch 4 is off and equal to 0 when switch 3 is off and switch 4 is on. By representing $i(t)$ with $\mathbf{i}$, $v(t)$ with $\mathbf{v}$, $q(t)_+$ with $\mathbf{q}_+$, and $q(t)_-$ with $\mathbf{q}_-$, the following state equations for the GAM model are found:

$$\frac{d\mathbf{i}}{dt} = \frac{V_{dc}}{L}(\mathbf{q}_+ - \mathbf{q}_-) - \left(\frac{R_L}{L}\mathbf{I} + \mathbf{T}\right)\mathbf{i} - \frac{1}{L}\mathbf{v} \tag{3.19}$$

$$\frac{d\mathbf{v}}{dt} = \frac{1}{C}\mathbf{i} - \left(\frac{1}{RC}\mathbf{I} + \mathbf{T}\right)\mathbf{v}, \tag{3.20}$$

where $\mathbf{I}$ is the identity matrix. If $q_+(t)$ and $q_-(t)$ are complementary (as considered herein), (3.19) can be simplified to

$$\frac{d\mathbf{i}}{dt} = \frac{V_{dc}}{L}(2\mathbf{q}_+ - [1\ 0\ 0 \ldots\ 0]^{\mathrm{T}}) - \left(\frac{R_L}{L}\mathbf{I} + \mathbf{T}\right)\mathbf{i} - \frac{1}{L}\mathbf{v}. \tag{3.21}$$

From Figure 3.2, it can be seen that the important components of the switching function include dc, the fundamental frequency $\bar{\omega}$ and the switching frequency $\hat{\omega}$. It is noted that the component magnitudes shown in Figure 3.2 are independent of $\bar{\omega}$ and $\hat{\omega}$. From (3.10) and (3.21), it can be seen that the dc components are not excited and can be excluded if their initial values are zero. So, the average vectors can be given by

$$\mathbf{x} = [x_{0,1c}\ x_{0,1s}\ x_{1,0c}\ x_{1,0s}]^{\mathrm{T}}, \tag{3.22}$$

where $x \in \{i, v, q_+\}$ and $\mathbf{x}$ is the corresponding average vector. This representation is referred to as Configuration 1 in Subsection 3.3.1 below.

It is also possible to represent more components in the GAM model. Depending on the magnitude of the modulation signal, the next most significant components shown in Figure 3.2 are the second-order sideband components of the switching frequency $\hat{\omega} \pm 2\bar{\omega}$. If these components are also included, the average vectors can be given by

$$\mathbf{x} = [x_{0,1c}\ x_{0,1s}\ x_{1,0c}\ x_{1,0s}\ x_{1,-2c}\ x_{1,-2s}\ x_{1,2c}\ x_{1,2s}]^{\mathrm{T}}. \tag{3.23}$$

This representation is referred to as Configuration 2 in Subsection 3.3.1 below. It could be expected that including more components in the QFS representations will result in more accurate simulation results, and this relationship is described more formally in Subsection 3.2.3.

It is possible to generalize the original system of ordinary differential equations in (3.17) and (3.18) to include various non-ideal effects (e.g., on-state voltage drop or passive component ESR). Using the properties in Table 3.1, these modifications can also be included in the GAM model in (3.20) and (3.21), resulting in improved accuracy (e.g., low-voltage, high-current inversion).

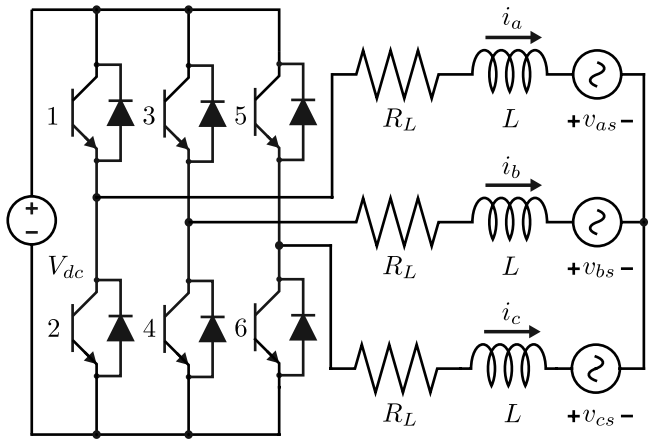

Figure 3.4: Three-phase inverter

It is noted that other modulation strategies can be considered with the proposed GAM models. For example, the first-order switching harmonic and associated sideband harmonics vanish under three-level modulation [51]. So, the first-order sidebands associated with double switching frequency can be selected to construct such inverter GAM models (i.e., $2\hat{\omega} \pm \bar{\omega}$ components).

3.2.2 Three-phase inverter

The three-phase grid-tie inverter is shown in Figure 3.4. The state equations for the detailed model are given by

$$\frac{di_a(t)}{dt} = \frac{V_{dc}}{L}\left(\frac{2}{3}q_a(t) - \frac{1}{3}q_b(t) - \frac{1}{3}q_c(t)\right) - \frac{R_L}{L}i_a(t) - \frac{v_{as}}{L} \tag{3.24}$$

$$\frac{di_b(t)}{dt} = \frac{V_{dc}}{L}\left(\frac{2}{3}q_b(t) - \frac{1}{3}q_a(t) - \frac{1}{3}q_c(t)\right) - \frac{R_L}{L}i_b(t) - \frac{v_{bs}}{L} \tag{3.25}$$

$$\frac{di_c(t)}{dt} = \frac{V_{dc}}{L}\left(\frac{2}{3}q_c(t) - \frac{1}{3}q_a(t) - \frac{1}{3}q_b(t)\right) - \frac{R_L}{L}i_c(t) - \frac{v_{cs}}{L}, \tag{3.26}$$

where $q_a(t)$ is equal to 1 when switch 1 is on and switch 2 is off and equal to 0 when switch 1 is off and switch 2 is on, $q_b(t)$ is equal to 1 when switch 3 is on and switch 4 is off and equal to 0 when switch 3 is off and switch 4 is on, and $q_c(t)$ is equal to 1 when switch 5 is on and switch 6 is off and equal to 0 when switch 5 is off and

switch 6 is on. By representing $i_y(t)$ with $\mathbf{i}_y$, $v_{ys}(t)$ with $\mathbf{v}_{ys}$, $q_y(t)$ with $\mathbf{q}_y$, where $y \in \{a, b, c\}$, the following state equations for the GAM model are found:

$$\frac{d\mathbf{i}_a}{dt} = \frac{V_{dc}}{L}\left(\frac{2}{3}\mathbf{q}_a - \frac{1}{3}\mathbf{q}_b - \frac{1}{3}\mathbf{q}_c\right) - \left(\mathbf{T} + \frac{R_L}{L}\mathbf{I}\right)\mathbf{i}_a - \frac{1}{L}\mathbf{v}_{as} \tag{3.27}$$

$$\frac{d\mathbf{i}_b}{dt} = \frac{V_{dc}}{L}\left(\frac{2}{3}\mathbf{q}_b - \frac{1}{3}\mathbf{q}_a - \frac{1}{3}\mathbf{q}_c\right) - \left(\mathbf{T} + \frac{R_L}{L}\mathbf{I}\right)\mathbf{i}_b - \frac{1}{L}\mathbf{v}_{bs} \tag{3.28}$$

$$\frac{d\mathbf{i}_c}{dt} = \frac{V_{dc}}{L}\left(\frac{2}{3}\mathbf{q}_c - \frac{1}{3}\mathbf{q}_a - \frac{1}{3}\mathbf{q}_b\right) - \left(\mathbf{T} + \frac{R_L}{L}\mathbf{I}\right)\mathbf{i}_c - \frac{1}{L}\mathbf{v}_{cs}. \tag{3.29}$$

Again from Figure 3.2, it can be seen that the most significant components of the switching function include dc, the fundamental frequency $\bar{\omega}$, the switching frequency $\hat{\omega}$, and the second-order sideband components of the switching frequency $\hat{\omega} \pm 2\bar{\omega}$. It is noted from (3.13) and (3.14) that if the three-phase modulation signals are balanced and compared with the same PWM carrier $c(t)$, the $q_{n,0c}$ and $q_{n,0s}$ components in the three-phase switching functions are equal to each other. From (3.27)-(3.29), it can be seen that the $x_{n,0c}$ and $x_{n,0s}$ components are not excited and can be excluded if their initial values are zero. So, the average vector can be given by

$$\mathbf{x} = [x_{0,1c}\ x_{0,1s}\ x_{1,-2c}\ x_{1,-2s}\ x_{1,2c}\ x_{1,2s}]^{\mathrm{T}}, \tag{3.30}$$

where $x \in \{i_a, i_b, i_c, v_{as}, v_{bs}, v_{cs}, q_a, q_b, q_c\}$ and $\mathbf{x}$ is the corresponding average vector. This representation is referred to as Configuration 1 in Subsection 3.3.2 below.

As with the single-phase inverter, it is possible to represent more components in the GAM model. The next most significant components shown in Figure 3.2 are the first-order sideband components of double the switching frequency $2\hat{\omega} \pm \bar{\omega}$. If these components are also represented, the average vector can be given by

$$\mathbf{x} = [x_{0,1c}\ x_{0,1s}\ x_{1,-2c}\ x_{1,-2s}\ x_{1,2c}\ x_{1,2s}\ x_{2,-1c}\ x_{2,-1s}\ x_{2,1c}\ x_{2,1s}]^{\mathrm{T}}, \tag{3.31}$$

and this representation is referred to as Configuration 2 in Subsection 3.3.2 below. As with the single-phase inverter, it could be expected that including more components in the QFS representations will result in more accurate simulation results.

If the grid voltages are purely sinusoidal, the grid voltage vectors are given by

$$\mathbf{v}_y = [v_{y,0,1c}\ v_{y,0,1s}\ 0\ \ldots\ 0]^{\mathrm{T}}, \tag{3.32}$$

where $y \in \{as, bs, cs\}$.

In the proposed single- and three-phase GAM models, it can be shown that the real part of the eigenvalues associated with different harmonic components of a state variable are the same, which means that the settling time of high-order switching harmonic components is the same as that of the fundamental component for a given state variable and that the dynamics associated with the switching harmonic components are significant in the transient response.

3.2.3 Accuracy of generalized averaging method models

A natural question arising from the use of truncated QFS representations for waveforms is that of the accuracy associated with these representations. The various fundamental and switching frequency components and sideband components of the switching frequency arise from the components of the switching function in (3.9). It can be seen in Figure 3.2 that these components have varying magnitudes depending on operating condition. Also, these components will be affected by the system in different ways depending on their frequencies. If a particular signal is of interest (e.g., the inductor current), it is possible to derive the transfer function from the switching function to the signal of interest. For example, in the single-phase inverter model

given above, the switching-function-to-inductor-current transfer function is

$$H_{Q_+I}(s) = \frac{2V_{dc}}{R_L + sL + \frac{1}{sC}||R} \tag{3.33}$$

Each component of the switching function (i.e., (3.9)) can be expressed as

$$q_{+,n,i}(t) = |Q_{+,n,i}| \cos(n\hat{\omega}t + i\bar{\omega}t + \angle Q_{+,n,i}), \tag{3.34}$$

where $Q_{+,n,i} = q_{+,n,ic} - jq_{+,n,is}$. The corresponding steady-state component of the signal of interest can be expressed as

$$i_{n,i}(t) = |I_{n,i}| \cos(n\hat{\omega}t + i\bar{\omega}t + \angle I_{n,i}), \tag{3.35}$$

where $I_{n,i} = H_{Q_+I}(j(n\hat{\omega} + i\bar{\omega}))Q_{+,n,i}$.

The instantaneous steady-state deviation associated with excluding some of the infinite terms from the truncated QFS representation can be calculated by

$$\Delta i(t) = \sum_{(n,i) \text{ not selected for QFS}} i_{n,i}(t). \tag{3.36}$$

As the magnitudes of the switching frequency components rapidly decay with increasing frequency and the transfer function has limited bandwidth, selection of a few relatively low-frequency components can achieve suitable accuracy. The maximum absolute deviation can be estimated by sampling (3.36) at a sufficiently high sampling rate (1 MHz used herein) over a sufficiently long window (0.05 s used herein) and including a sufficiently large number of terms in the summation ($n \in \{0, \ldots, 20\}$ and $i \in \{-20, \ldots, 20\}$ used herein). Specific examples of these accuracy estimates are provided in the sections below.

3.3 Simulation Results

In order to examine the proposed inverter GAM models, simulations of single- and three-phase inverters are discussed in this section. All of the models are simulated by the ode32tb Simulink solver with a default relative tolerance of 10^{-3} in MATLAB 2013a. The Bessel function of the first kind is implemented using the MATLAB interpreter. The simulation time for each simulation study is 2 s. In each simulation study, a detailed model, an SSA model, and the configurations of the GAM model are compared. Plots comparing simulation waveforms on the order of the fundamental period and on the order of the switching period are shown. The maximum absolute deviations (with respect to the detailed model) are calculated from the final steady state using a sampling rate of 1 MHz over one period. The run time of the simulation is reported as the mean run time over 100 simulations. The initial values of the state variables in all of the simulations are equal to the corresponding steady state values.

3.3.1 Single-phase inverter simulation results

The structure of the single-phase inverter for the simulation is shown in Figure 3.3. The parameters of the single-phase inverter are listed in the Table 3.2. A step load resistance change is considered. Two configurations of the single-phase inverter GAM model are considered. In Configuration 1, the waveforms of the GAM model are represented using a 60-Hz fundamental component and a 10-kHz switching frequency component. In Configuration 2, the components of Configuration 1 are used as well as 9.88-kHz and 10.12-kHz sideband components. Each of these configurations is compared with a detailed model that models the detailed behavior of each switch.

Figs. 3.5 (a) and 3.6 (a) show the inductor current and capacitor voltage during the first two fundamental periods predicted by the detailed model, Configuration 1 of the GAM model, and the SSA model. Figs. 3.5 (b) and 3.6 (b) show these waveforms in

Table 3.2: Single-Phase Inverter Simulation Parameters

Input voltage, V_{dc}	220 V
Inductance of LC filter, L	0.276 mH
Inductor resistance, R_L	0.05 Ω
Capacitance of LC filter, C	8 µF
Switching frequency, $\hat{f}$	10 kHz
Switching function phase, $\hat{\phi}$	$\pi/2$ rad
Modulation signal frequency, $\bar{f}$	60 Hz
Modulation signal magnitude	0.9
Modulation signal phase, $\bar{\phi}$	1 rad
Initial load resistance, R	2 Ω
Final load resistance, R	5 Ω
Load resistance step time	16.7 ms

closer proximity to the step resistance change. From Figure 3.5, it can be seen that the fundamental component of the current waveform matches the detailed model current waveform and the SSA model current waveform. However, the magnitude of the current ripple predicted by Configuration 1 of the GAM model shown in Figure 3.5 does not change during steady state. As a result, the current ripple predicted by the GAM model is larger than that predicted by the detailed model when the current is high and smaller than that predicted by the detailed model when the current is near 0 A. It also can be seen that the voltage ripple magnitude predicted by Configuration 1 of the GAM model shown in Figure 3.6 does not vary in the same way as that predicted by the detailed model. In the steady state, the average vectors are constant and the switching ripple is represented by a 10-kHz sinusoidal waveform. As a result, the capacitor voltage and inductor current ripple magnitudes predicted by Configuration 1 do not vary as those predicted by the detailed model. It is noted that the change of the load resistance R affects the transfer functions (e.g., (3.33)). Thus, the switching ripple magnitudes of the inductor current and the capacitor voltage predicted by the GAM model change after step load change.

Figs. 3.7 (a) and 3.8 (a) show the inductor current and capacitor voltage during the first two fundamental periods predicted by the detailed model, Configuration 2 of

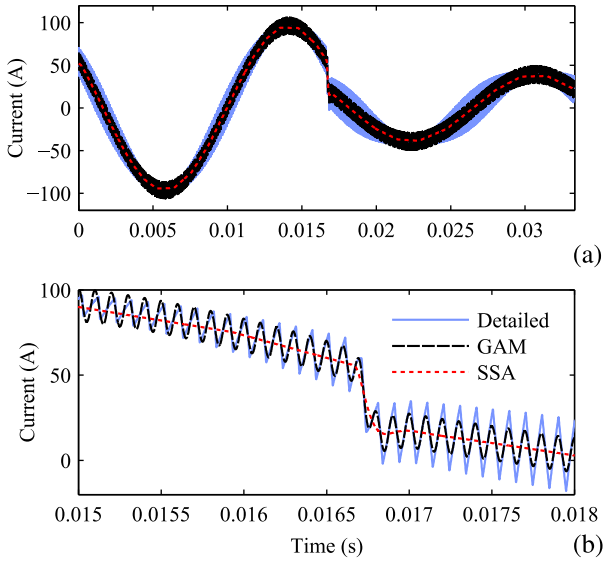

Figure 3.5: Configuration 1 (without sidebands) single-phase inverter inductor current

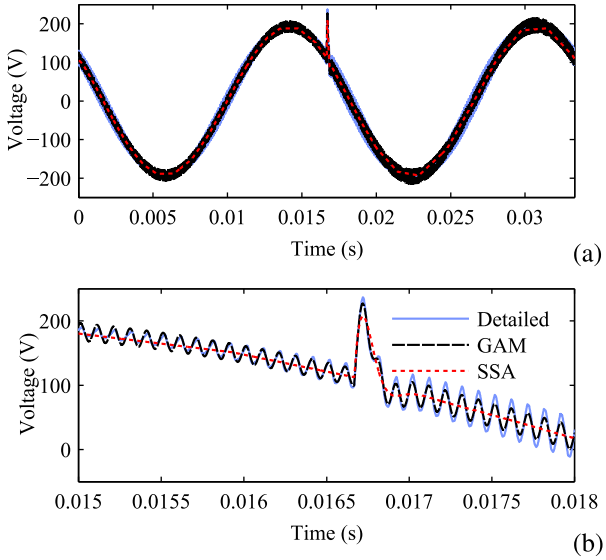

Figure 3.6: Configuration 1 (without sidebands) single-phase inverter capacitor voltage

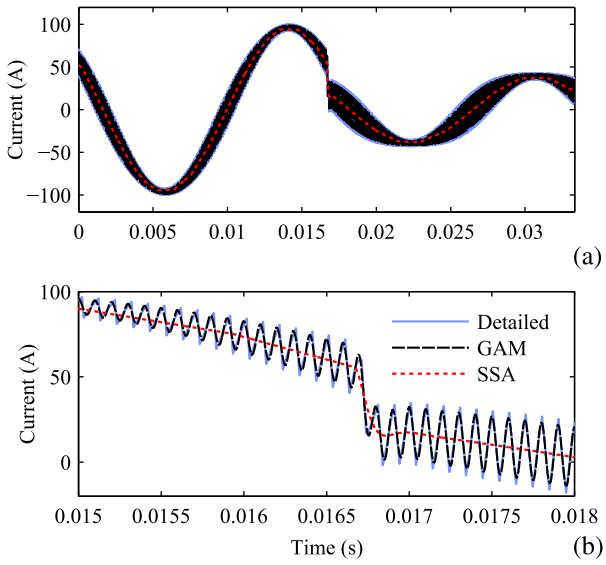

Figure 3.7: Configuration 2 (with sidebands) single-phase inverter inductor current

the GAM model, and the SSA model. Figs. 3.7 (b) and 3.8 (b) show these waveforms in closer proximity to the step resistance change. From Figure 3.7, it can be seen that the magnitude of the inductor current ripple predicted by Configuration 2 of the GAM model follows the variation of that predicted by the detailed model during both steady-state and transient conditions. The voltage ripple magnitude predicted by Configuration 2 of the GAM model also changes in the same manner as that predicted by the detailed model as shown in Figure 3.8.

Figs. 3.5–3.8 show that the fundamental components of the inductor current and capacitor voltage waveforms always match the corresponding detailed model fundamental components and the corresponding SSA model waveforms. However, the SSA model does not represent the switching ripple.

To assess the accuracy of the two configurations, the maximum absolute deviations of the inductor current and the capacitor voltage for the condition following the step load change are determined from the simulation and from the estimation technique presented in Subsection 3.2.3. The results are listed in Table 3.3. The maximum absolute deviations of the inductor current and the capacitor voltage between the

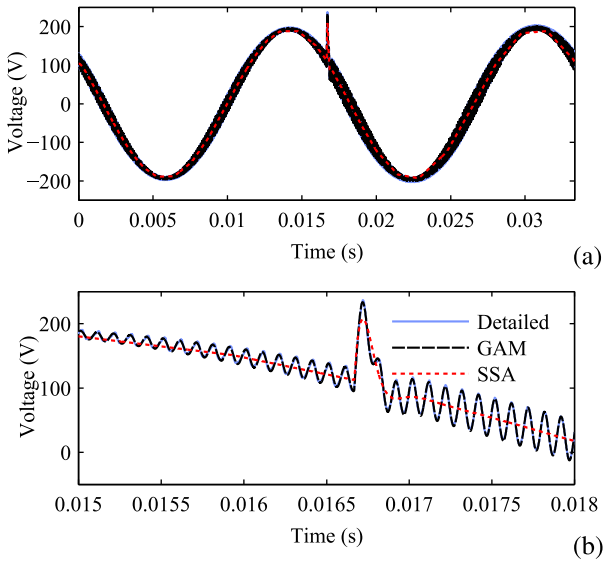

Figure 3.8: Configuration 2 (with sidebands) single-phase inverter capacitor voltage

Table 3.3: Single-Phase Maximum Absolute Deviation of Steady-State Capacitor Voltage and Inductor Current

Variable	Model	Maximum absolute deviation	
		Simulation	Estimate
Inductor current	SSA	21.9 A	
	Configuration 1	11.7 A	11.2 A
	Configuration 2	7.13 A	6.70 A
Capacitor voltage	SSA	35.5 V	
	Configuration 1	14.6 V	14.8 V
	Configuration 2	4.49 V	4.54 V

SSA model and the detailed model from simulation are also listed in Table 3.3. The maximum absolute deviations of the two GAM configurations are significantly smaller than those of the SSA model. It can be seen that the maximum absolute deviations of the GAM model are decreased by including more harmonic components in the waveform representations. It is also observed that the accuracy estimates correspond with the deviations observed in the simulation results.

The run times of the SSA model, Configurations 1 and 2 of the GAM model, and the detailed model are shown in Table 3.4. The normalized run times of those models are shown in Figure 3.9, wherein the run times are normalized by the run time of the detailed model. It can be seen that average simulation speeds of both configurations

Table 3.4: Single-Phase Inverter Simulation Run Time

Model	Run time (ms)
SSA	29.8
Configuration 1	33.5
Configuration 2	43.1
Detailed	4590

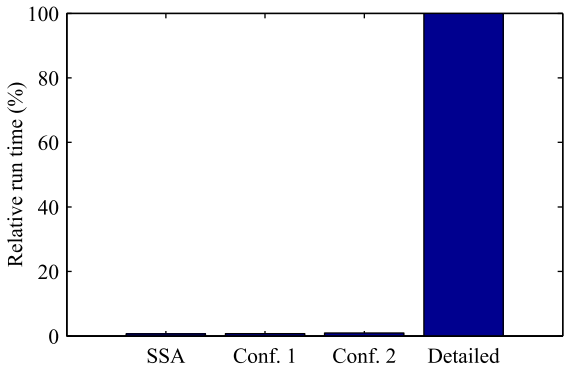

Figure 3.9: Normalized single-phase inverter simulation run time. Conf. 1 and Conf. 2 indicate Configuration 1 and Configuration 2 of the single-phase GAM model, respectively.

of the GAM model are more than 100 times faster than that of the detailed model and less than two times slower than that of the SSA model. They each also predict the switching ripple components of the waveforms like the detailed model, but Configuration 2 provides better predictions of these components; the SSA model does not attempt to represent these components. The run time of Configuration 2 of the GAM model is larger than the run time of Configuration 1 because of the additional complexity associated with including the sideband components. This results in a trade off between simulation run time and accuracy, which should be addressed based on the requirements of a given simulation study.

3.3.2 Three-phase inverter simulation results

The structure of the three-phase inverter for the simulation is shown in Figure 3.4. The parameters of the three-phase inverter are listed in the Table 3.5. The three-

Table 3.5: Three-Phase Inverter Simulation Parameters

Input voltage, V_{dc}	220 V
Grid line-to-line rms voltage	120 V
Inductance of L filter, L	0.276 mH
Inductor resistance, R_L	0.05 Ω
Switching frequency, $\hat{f}$	10 kHz
Switching function phase, $\hat{\phi}$	0 rad
Grid voltage frequency, $\bar{f}$	60 Hz
Initial modulation signal, $m(t)$	$0.911\cos(\bar{\omega}t + 0.0441)$
Final modulation signal, $m(t)$	$0.875\cos(\bar{\omega}t + 0.0561)$
Modulation signal step time	16.7 ms

phase grid voltages and the three-phase output voltages of the inverter are balanced. The phase angle of the a-phase line-to-neutral grid voltage v_{as} is equal to 0 rad. A step change in modulation signal is studied. Two configurations of the three-phase GAM model are considered. In Configuration 1, the waveforms of the GAM model are represented using 60-Hz components and 9.88-kHz and 10.12-kHz components that are sidebands to the 10-kHz switching frequency. In Configuration 2, the components of Configuration 1 are used as well as 19.94-kHz and 20.06-kHz components that are sidebands to double the switching frequency. Each of these configurations is compared with a detailed model that models the detailed behavior of each switch.

Figure 3.10 (a) shows the three-phase inductor currents during the first two fundamental periods predicted by the detailed model, Configuration 1 of the GAM model and the SSA model. Figure 3.10 (b) shows these waveforms in closer proximity to the modulation signal step change. It can be seen that the current ripple predicted by Configuration 1 of the GAM model matches that predicted by the detailed model during the steady state and transient conditions.

Figure 3.11 (a) shows the three-phase inductor currents during the first two fundamental periods predicted by the detailed model, Configuration 2 of the GAM model and the SSA model. Figure 3.11 (b) shows these waveforms in closer proximity to the modulation signal step change. It can be seen that the inductor currents pre-

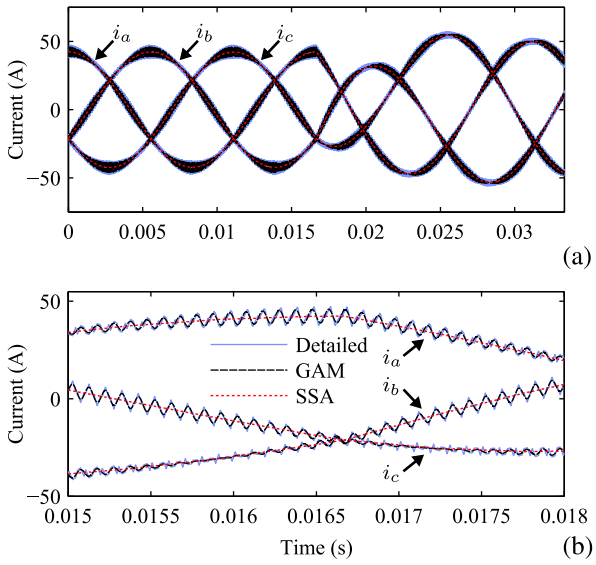

Figure 3.10: Configuration 1 (with sidebands of 10 kHz) three-phase inverter inductor currents

dicted by the Configuration 2 of the GAM model fit inductor currents predicted by detailed model better than those predicted by the Configuration 1 of the GAM model, especially when the current ripple is small (e.g., i_b at approximately 16 ms).

Figs. 3.10 and 3.11 show the fundamental components of the three-phase inductor currents of both configurations match those of the detailed model and the three-phase inductor currents of the SSA model.

The maximum absolute deviations of the three-phase inductor currents for the condition following the step modulation signal change are determined from the simulation and from the estimation technique, and the results are listed in Table 3.6. The maximum absolute deviations of the three-phase inductor currents between the SSA model and the detailed model from simulation are also listed in Table 3.6. It can be seen that the accuracy of the GAM model can be increased by adding more harmonic components in the average vectors, and that the estimates correspond well with the simulation results. Both configurations of the GAM model have better accuracy than the SSA model because of their representation of the switching components.

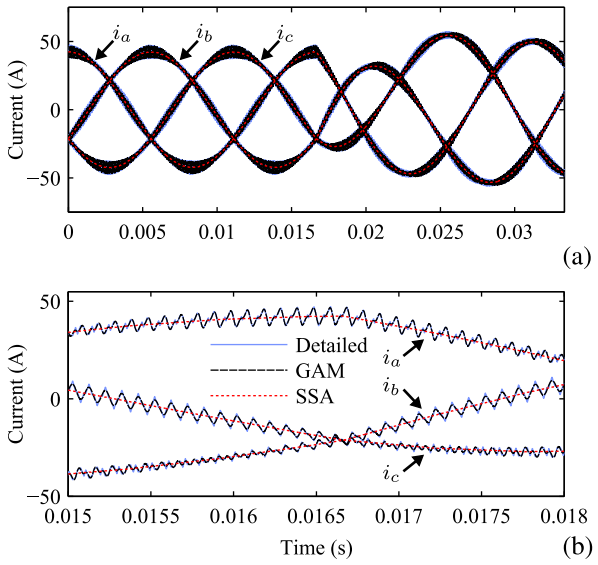

Figure 3.11: Configuration 2 (with sidebands of 10 kHz and 20 kHz) three-phase inverter inductor currents

Table 3.6: Three-Phase Maximum Absolute Deviation of Steady-State Inductor Currents

Variable	Model	Maximum absolute deviation	
		Simulation	Estimate
a-phase inductor current	SSA	5.15 A	
	Configuration 1	2.49 A	2.39 A
	Configuration 2	1.78 A	1.62 A
b-phase inductor current	SSA	5.24 A	
	Configuration 1	2.50 A	2.39 A
	Configuration 2	1.79 A	1.62 A
c-phase inductor current	SSA	5.24 A	
	Configuration 1	2.50 A	2.39 A
	Configuration 2	1.79 A	1.62 A

Table 3.7: Three-Phase Inverter Simulation Run Time

Model	Run time (ms)
SSA	67.0
Configuration 1	246
Configuration 2	612
Detailed	5610

The run times of the SSA model, the two configurations of the GAM model, and the detailed model are shown in Table 3.7. The normalized run times of those models are also shown in Figure 3.12, wherein the run times are normalized by the run time of the detailed model. It can seen that the run times of both configurations of the GAM model are much smaller (approximately 10–20 times smaller) than the run time of the detailed model. The run time of Configuration 1 of the GAM model is less than 4 times larger than that of the SSA model. It can be noted that the run-time advantages of the GAM models are less pronounced than those in the single-phase inverter. It can also be noted that the inclusion of more generalized averaging components (i.e., the sidebands of 20 kHz in Configuration 2) has a relatively higher cost compared with including more components in the single-phase inverter GAM models. The source of these differences between the single- and three-phase inverters is related to the dynamics of the grid-tied three-phase inverter system with open-loop control. This system is very lightly damped and causes significantly longer settling times, resulting in longer generalized averaging simulation run times. The open-loop system is considered in simulation to demonstrate the method, but it would be impractical to operate such a system without more damping. In such a more practical situation, simulation run times for the GAM models are expected to decrease further, and the relative run-time penalty of including more generalized averaging components is expected to decrease as well.

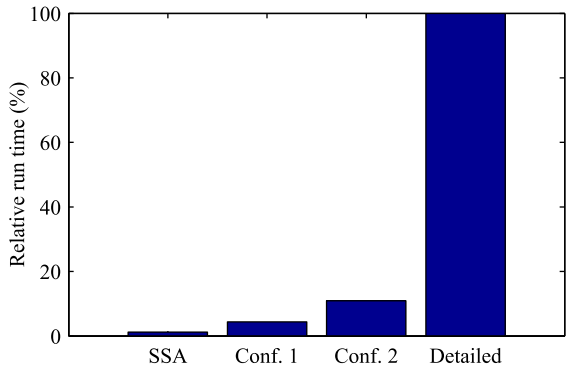

Figure 3.12: Normalized three-phase inverter simulation run time. Conf. 1 and Conf. 2 indicate Configuration 1 and Configuration 2 of the three-phase GAM model, respectively.

3.4 Experimental Results

To demonstrate the proposed GAM model, it is compared with experimental measurements in this section. A flexible prototype inverter is controlled using a TMS320F28335 microcontroller. The sampling rates of the analog-to-digital converter and the controller are 100 kHz. The waveforms are sampled using an oscilloscope with a 20-MHz sampling rate. The experimental setup is shown in Figure 3.13. The prototype inverter box contains three IGBT modules (Powerex CM200DY-24A modules) and drives, the microcontroller, sensors, a power supply, and an interface board. The filter box contains two three-phase inductors and a three-phase capacitor. Single- and three-phase experiments are conducted by changing the connections among the IGBT modules, the capacitor, and the inductors.

3.4.1 Single-phase experimental results

For the single-phase inverter experiment, a grid-tied single-phase inverter setup is used. The output of the inverter is connected to the grid through an L filter. This setup corresponds to the circuit shown in Figure 3.3 with the parallel capacitor C and resistor R replaced by a grid voltage source v_g. Due to grid voltage distortion, a

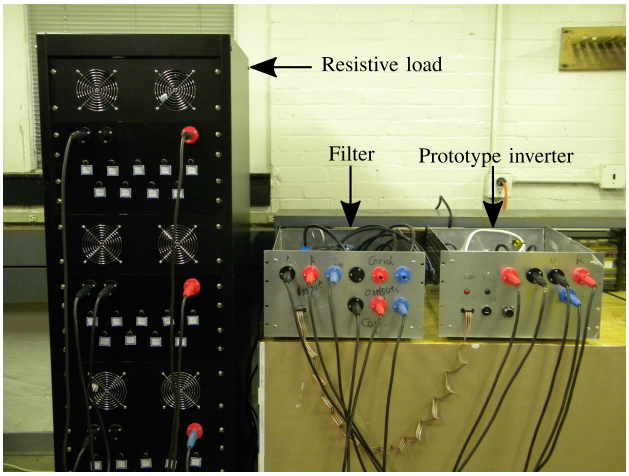

Figure 3.13: Experimental setup

PI controller is used to ensure that the output current follows the reference current. The control equation is given by

$$m = k_p(i^* - \bar{i}) + k_i \int (i^* - \bar{i})dt + \frac{L\frac{di^*}{dt} + v_g^*}{V_{dc}}, \tag{3.37}$$

where $\bar{i}$ is the output current filtered by a second-order low-pass filter with a time constant of 37.9 µs. The parameters for the single-phase inverter are listed in Table 3.8. The grid phase information is obtained by a phase-locked loop based on a second-order generalized integrator [90]. A step change in reference current i^* is studied. Because the second-order low-pass filter is used to filter the ripple of the inductor current, the effect of high-frequency inductor current harmonics on the modulation signal is considered negligible. The GAM model of the PI controller only includes the 60-Hz component of the inductor current. The QFS components of the switching function are calculated from the modulation signal output from the PI controller. Figure 3.14 (a) shows the inductor current predicted by the GAM model compared with that measured experimentally. Figure 3.14 (b) shows these waveforms in closer proximity to the modulation signal step change. The GAM model inductor current shown in Figure 3.14 is represented by a 60-Hz fundamental component, a 10-kHz

Table 3.8: Single-Phase Inverter Experimental Parameters

Input voltage, V_{dc}	220 V
Grid voltage, v_g	$\sqrt{2}\,125\cos(\bar{\omega}t)$ V
Inductance of L filter, L	1.352 mH
Inductor resistance, R_L	0.05 Ω
Proportional gain, k_p	0.05 A^{-1}
Integral gain, k_i	5 $A^{-1}s^{-1}$
Grid reference voltage, v_g^*	$\sqrt{2}\,125\cos(\bar{\omega}t)$ V
Switching frequency, $\hat{f}$	10 kHz
Grid voltage frequency, $\bar{f}$	60 Hz
Initial reference current, i^*	$\sqrt{2}\,25\cos(\bar{\omega}t)$ A
Final reference current, i^*	$\sqrt{2}\,15\cos(\bar{\omega}t + \frac{\pi}{6})$ A
Reference current step time	16.7 ms

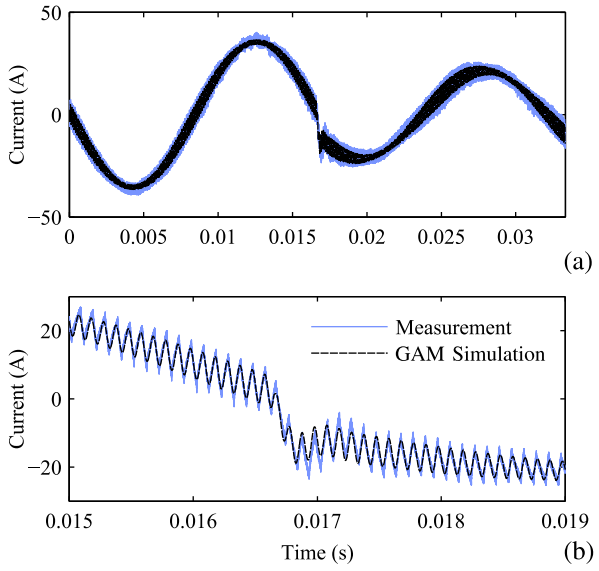

Figure 3.14: Single-phase inverter inductor current

switching frequency component, and 9.88-kHz and 10.12-kHz sideband components, corresponding to Configuration 2 in Subsection 3.3.1. It can be seen that the magnitude of the inductor current ripple predicted by the GAM model follows the variation that was observed experimentally during the steady state and transient.

The maximum absolute deviation of the inductor current following the step reference signal change is determined from the experimental data, from a detailed simulation, and by estimation. The results are presented in Table 3.9. It can be seen that

Table 3.9: Single-Phase Maximum Absolute Deviation of Steady-State Inductor Current

Variable	Maximum absolute deviation		
	Experiment	Simulation	Estimate
Inductor current	5.49 A	2.23 A	1.89 A

the estimate corresponds well with the detailed simulation result. However, it can be seen that measurement noise, unmodeled switching transient behavior, and unmodeled grid voltage harmonics can cause the estimate (and the detailed simulation) to underpredict the maximum absolute deviation.

3.4.2 Three-phase experimental results

For the three-phase experiment, a three-phase inverter setup is connected with a three-phase LC filter to a wye-connected resistive load. This setup corresponds to the circuit shown in Figure 3.4 with the three-phase grid voltage sources v_{as}, v_{bs}, and v_{cs} replaced with three-phase wye-connected parallel capacitors C and resistors R. The parameters of the three-phase inverter are listed in Table 3.10. A step change in three-phase modulation signal is studied. Figs. 3.15 (a) and 3.16 (a) show the inductor currents and line-to-line capacitor voltages predicted by the GAM model compared with those measured experimentally. Figs. 3.15 (b) and 3.16 (b) show these waveforms in closer proximity to the modulation signal step change. It is noted that the line-to-line capacitor voltage is also the line-to-line load voltage because the three-phase capacitor and three-phase resistor are parallel connected. The GAM model waveforms shown in Figs. 3.15 and 3.16 are represented by a 60-Hz fundamental component, 4.88-kHz and 5.12-kHz sideband components of the switching frequency, and 9.94-kHz and 10.06-kHz sideband components of double the switching frequency, corresponding to Configuration 2 in Subsection 3.3.2. It can be seen that the magnitude of the inductor current ripple predicted by the GAM model follows the variation that was observed experimentally during the steady state and transient. It also can be seen that the

Table 3.10: Three-Phase Inverter Experimental Parameters

Input voltage, V_{dc}	170 V
Inductance of LC filter, L	0.276 mH
Inductor resistance, R_L	0.05 Ω
Capacitance of LC filter, C	24 µF
Load resistance, R	2.2 Ω
Switching frequency, $\hat{f}$	5 kHz
Modulation signal frequency, $\bar{f}$	60 Hz
Initial modulation signal of a phase	$0.8\cos(\bar{\omega}t)$
Final modulation signal of a phase	$0.5\cos(\bar{\omega}t - \pi/6)$
Modulation signal step time	16.7 ms

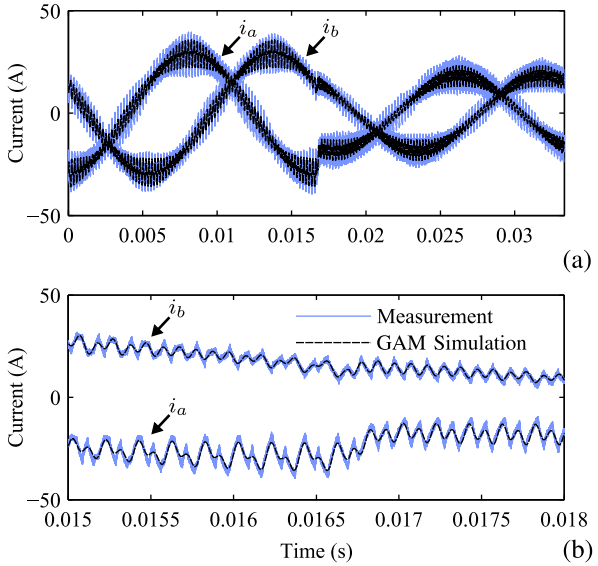

Figure 3.15: Three-phase inverter inductor currents

line-to-line capacitor voltages predicted by the GAM model match those measured experimentally.

After the step modulation signal change, the maximum absolute deviations of the inductor currents and the line-to-line capacitor voltages are determined from the experimental data, a detailed simulation, and the estimation technique, and the results are shown in Table 3.11. As seen in the single-phase case, the estimates match the deviations observed between the detailed model and the GAM model. However, measurement noise and unmodeled switching dynamics can cause both the estimates and the detailed simulation results to underpredict the maximum absolute deviations.

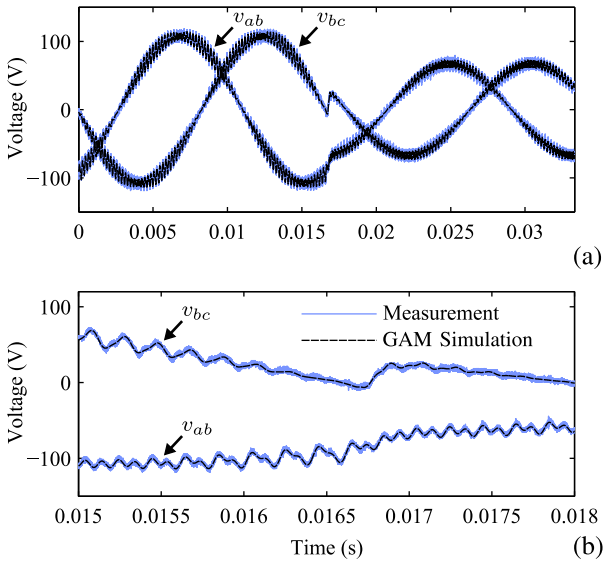

Figure 3.16: Three-phase inverter line-to-line capacitor (load) voltages

Table 3.11: Three-Phase Maximum Absolute Deviations of Inductor Currents and Line-to-Line Capacitor Voltages

Variable	Maximum absolute deviation		
	Experiment	Simulation	Estimate
a-phase inductor current	6.12 A	2.55 A	2.34 A
b-phase inductor current	4.98 A	2.55 A	2.34 A
a-to-b-phase capacitor voltage	8.59 V	1.54 V	1.53 V
b-to-c-phase capacitor voltage	8.52 V	1.54 V	1.53 V

3.5 Conclusion

Herein, GAM models for single- and three-phase PWM inverters are proposed. These models are based on a QFS representation of the switching functions that includes fundamental and switching frequency components as well as sideband components of the switching frequency. These models are compared with the detailed model and the SSA model in simulations, and it is found that the use of sideband components allows accurate representation of the variation in switching ripple magnitude that occurs in the steady state. Furthermore, because the state variables in the GAM models are constant in the steady state, the GAM models are found to have significantly faster simulation speeds than those associated with detailed models and slightly slower

simulation speeds than those associated with SSA models. These models are also demonstrated experimentally, and it is found that the simulation results from the GAM models match the experiment measurements in the steady state and transient. Therefore, the proposed GAM models are suitable for simulation applications in which both accuracy (in terms of both fundamental and switching behavior) and fast run times are required (e.g., long simulation times, systems with multiple converters, and repeated simulations).

Chapter 4

Three-Phase Inverter Modeling using Generalized Average Method with Third-Harmonic Injection

The QFS representation for the switching functions of three-phase PWM inverters with third-harmonic injection is provided in this chapter. The work described in this chapter has been published in [91]. This representation is used to construct an GAM model of three-phase inverters with third-harmonic injection. In the proposed GAM model, the state variables are represented using the fundamental and third harmonic components of the modulation signal, the components corresponding to multiples of the switching frequency and the sideband components of multiples of the switching frequency. The proposed model is demonstrated in simulation and found to accurately predict both the fundamental and the switching behavior of the three-phase inverter. Furthermore, since the proposed GAM model is time invariant, state variables in this model are constant in the steady state and the simulation speed of the GAM model is significantly faster than that of the detailed model. The contributions of this work are (1) the QFS representation of the switching function of three-phase

PWM inverters with third-harmonic injection, (2) the proposal of an GAM model for PWM three-phase inverters with third-harmonic injection, and (3) the demonstration of the proposed GAM model in simulation.

The remainder of this chapter is organized as follows. The QFS representation of the switching function of three-phase PWM inverters with third-harmonic injection is described in Section 4.1. In Section 4.2, the GAM model for three-phase inverters is proposed. The proposed three-phase inverter GAM model is compared with a detailed model in Section 4.3. Finally, conclusions are drawn in Section 4.4.

4.1 Generalized Average Method Model

Herein, the QFS representation of the state variables in three-phase PWM inverters with third-harmonic injection is studied. By assuming the modulation signal is a sinusoidal waveform with third-harmonic injection, the modulation signal can be expressed by

$$m(t) = m_1 \cos(\bar{\omega}t + \bar{\phi}_0) + m_3 \cos(3\bar{\omega}t + \bar{\phi}_{30}), \tag{4.1}$$

where $\bar{\omega}$ is the angular frequency of the modulation signal, m_1 and m_3 are the magnitude of the fundamental modulation signal and third-harmonic injection, respectively, and $\bar{\phi}_0$ and $\bar{\phi}_{30}$ are the phase angle of the fundamental modulation signal and third-harmonic injection, respectively. The instantaneous switch duty cycle can be expressed as

$$D = \frac{1}{2}(m(t) + 1). \tag{4.2}$$

The instantaneous switching function is generated by comparing the switch duty cycle D with the double-edge triangular carrier signal $c(t)$ as in the following relationship:

$$q(t) = \begin{cases} 1, & D \geq c(t) \\ 0, & \text{otherwise} \end{cases}. \tag{4.3}$$

The general periodic switching function for constant duty cycle D can be expressed as the following Fourier series:

$$q(t) = D + \frac{2}{\pi}\sum_{n=1}^{\infty}\frac{\sin(n\pi D)}{n}\cos(n\hat{\omega}t + n\hat{\phi}), \tag{4.4}$$

where $\hat{\omega}$ is the angular frequency of switching function and $\hat{\phi}$ is the phase angle of the switching function. In [53], it states that the same switching function expression can be used with the time-varying duty cycle for the slowly varying duty cycle. It is assumed that the modulation signal changes more slowly than the switching signal. By substituting (4.1) and (4.2) into (4.4), it can be shown that the general QFS representation of the switching function for sinusoidal modulation signal with third-harmonic injection can be given by

$$\begin{aligned} q(t) = {} & q_{0,0} + q_{0,1c}\cos(\bar{\omega}t) + q_{0,1s}\sin(\bar{\omega}t) + q_{0,3c}\cos(3\bar{\omega}t) + q_{0,3s}\sin(3\bar{\omega}t) \\ & + \sum_{n=1}^{\infty}\sum_{i=-\infty}^{\infty} q_{n,ic}\cos(n\hat{\omega}t + i\bar{\omega}t) + \sum_{n=1}^{\infty}\sum_{i=-\infty}^{\infty} q_{n,is}\sin(n\hat{\omega}t + i\bar{\omega}t), \end{aligned} \tag{4.5}$$

where

$$q_{0,0} = \frac{1}{2} \tag{4.6}$$

$$q_{0,1c} = \frac{1}{2}m_1\cos(\bar{\phi}_0) \tag{4.7}$$

$$q_{0,1s} = -\frac{1}{2}m_1\sin(\bar{\phi}_0) \tag{4.8}$$

$$q_{0,3c} = \frac{1}{2}m_3\cos(\bar{\phi}_{30}) \tag{4.9}$$

$$q_{0,3s} = -\frac{1}{2}m_3\sin(\bar{\phi}_{30}) \tag{4.10}$$

$$q_{n,ic} = \sum_{j=-\infty}^{\infty} \frac{2}{n\pi} J_{i-3j}\left(\frac{n\pi m_1}{2}\right) J_j\left(\frac{n\pi m_3}{2}\right) \sin\left(\frac{(n+i-2j)\pi}{2}\right)$$
$$\cos\left(n\hat{\phi} + (i-3j)\bar{\phi}_0 + j\bar{\phi}_{30}\right) \tag{4.11}$$
$$q_{n,is} = -\sum_{j=-\infty}^{\infty} \frac{2}{n\pi} J_{i-3j}\left(\frac{n\pi m_1}{2}\right) J_j\left(\frac{n\pi m_3}{2}\right) \sin\left(\frac{(n+i-2j)\pi}{2}\right)$$
$$\sin\left(n\hat{\phi} + (i-3j)\bar{\phi}_0 + j\bar{\phi}_{30}\right) \tag{4.12}$$

The function $J_y(x)$ is the Bessel function of the first kind of integer order y. The analyses of the harmonic spectrum of PWM waveforms with third-harmonic injection can also be found in [51].

Discrete Fourier transformations are used to find the magnitudes of the components of the switching functions. Two switching functions are generated by comparing a 10-kHz carrier signal with two different a-phase 60-Hz modulation signals which are sampled at 30 MHz. The magnitude of the third-harmonic injection m_3 is set to $-m_1/6$ to allow for a wider voltage range without overmodulation. Figure 4.1 shows the most important components of the switching functions. It can be seen that all harmonic amplitudes of the switching functions except for the dc component amplitude change when the magnitudes of the fundamental modulation signal and third-harmonic injection change. When the sum $n+i$ is even, the $\sin((n+i-2j)\pi/2)$ terms in (4.11) and (4.12) are equal to zero, resulting in vanishing of the corresponding components of the switching functions. So, there are no 9.94 kHz, 10.06 kHz, 20 kHz, 19.88 kHz and 20.12 kHz harmonics in Figure 4.1. The harmonic amplitudes shown in Figure 4.1 can also be calculated by using (4.5)–(4.12).

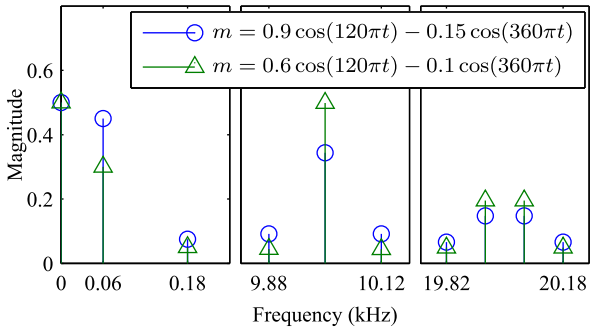

Figure 4.1: Discrete Fourier transform of switching functions

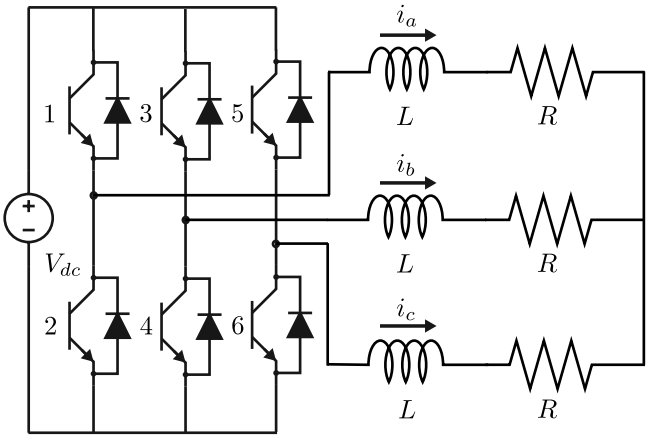

Figure 4.2: Three-phase inverter

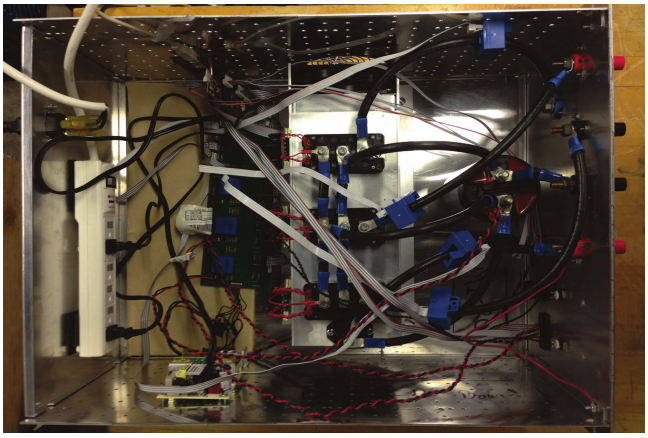

Figure 4.3: Three-phase inverter prototype

All of the state variables of the PWM inverter can be expressed using a QFS representation similar to that of the switching function. The instantaneous state

variables can be approximated by the QFS representation as

$$x(t) \approx \mathbf{C}(t)\mathbf{x}, \tag{4.13}$$

where

$$\mathbf{x} = [x_{0,0}\ x_{n_1,i_1c}\ x_{n_1,i_1s}\ \ldots\ x_{n_o,i_oc}\ x_{n_o,i_os}]^{\mathrm{T}}, \tag{4.14}$$

$$\mathbf{C}(t) = \begin{bmatrix} 1 \\ \cos(n_1\hat{\omega}t + i_1\bar{\omega}t) \\ \sin(n_1\hat{\omega}t + i_1\bar{\omega}t) \\ \vdots \\ \cos(n_o\hat{\omega}t + i_o\bar{\omega}t) \\ \sin(n_o\hat{\omega}t + i_o\bar{\omega}t) \end{bmatrix}^{\mathrm{T}}, \tag{4.15}$$

$x_{0,0}$, x_{n_1,i_1c}, x_{n_1,i_1s}, $\ldots$ x_{n_o,i_oc} and x_{n_o,i_os} are index-0, index-n_1i_1c, index-n_1i_1s, $\ldots$ index-n_oi_oc, and index-n_oi_os QFS coefficients of the Fourier series of state variables, respectively, and n_k is the order of the kth selected $\hat{\omega}$ component and i_k is the corresponding order of kth selected $\bar{\omega}$ component for $k \in \{1, 2, \ldots o\}$. It can be seen that the average vector $\mathbf{x}$ is constructed by the QFS coefficients and has $2o + 1$ elements.

4.2 Inverter Generalized Average Method Model

The three-phase grid-tie inverter is shown in Figure 4.2. For each branch, the switching function is equal to 1 when the corresponding upper switch is on and is equal to 0 when the corresponding lower switch is on. The state equations for the detailed

model are given by

$$\frac{di_a(t)}{dt} = \frac{V_{dc}}{L}\left(\frac{2}{3}q_a(t) - \frac{1}{3}q_b(t) - \frac{1}{3}q_c(t)\right) - \frac{R}{L}i_a(t) \tag{4.16}$$

$$\frac{di_b(t)}{dt} = \frac{V_{dc}}{L}\left(\frac{2}{3}q_b(t) - \frac{1}{3}q_a(t) - \frac{1}{3}q_c(t)\right) - \frac{R}{L}i_b(t) \tag{4.17}$$

$$\frac{di_c(t)}{dt} = \frac{V_{dc}}{L}\left(\frac{2}{3}q_c(t) - \frac{1}{3}q_a(t) - \frac{1}{3}q_b(t)\right) - \frac{R}{L}i_c(t). \tag{4.18}$$

where $q_a(t)$, $q_b(t)$ and $q_c(t)$ are the three-phase switching functions. By using average vectors instead of instantaneous values of the state variables and switching functions, (4.16)–(4.18) become

$$\frac{d\mathbf{i}_a}{dt} = \frac{V_{dc}}{L}\left(\frac{2}{3}\mathbf{q}_a - \frac{1}{3}\mathbf{q}_b - \frac{1}{3}\mathbf{q}_c\right) - \left(\mathbf{T} + \frac{R}{L}\mathbf{I}\right)\mathbf{i}_a \tag{4.19}$$

$$\frac{d\mathbf{i}_b}{dt} = \frac{V_{dc}}{L}\left(\frac{2}{3}\mathbf{q}_b - \frac{1}{3}\mathbf{q}_a - \frac{1}{3}\mathbf{q}_c\right) - \left(\mathbf{T} + \frac{R}{L}\mathbf{I}\right)\mathbf{i}_b \tag{4.20}$$

$$\frac{d\mathbf{i}_c}{dt} = \frac{V_{dc}}{L}\left(\frac{2}{3}\mathbf{q}_c - \frac{1}{3}\mathbf{q}_a - \frac{1}{3}\mathbf{q}_b\right) - \left(\mathbf{T} + \frac{R}{L}\mathbf{I}\right)\mathbf{i}_c, \tag{4.21}$$

where $\mathbf{q}_a$, $\mathbf{q}_b$ and $\mathbf{q}_c$ are the average vectors of the three-phase switching functions, and $\mathbf{i}_a$, $\mathbf{i}_b$ and $\mathbf{i}_c$ are the average vectors of the three-phase inductor currents, $\mathbf{I}$ is the identity matrix and $\mathbf{T}$ is a $(2o+1) \times (2o+1)$ matrix that is constructed such that all elements are zero except for the $(2k, 2k+1)$ elements with values $n_k\hat{\omega} + i_k\bar{\omega}$ and the $(2k+1, 2k)$ elements with values $-(n_k\hat{\omega} + i_k\bar{\omega})$ for $k \in \{1, 2, \ldots o\}$.

To achieve the maximum output voltage without overmodulation [51], the three-phase modulation signals with third-harmonic injection are given by

$$m_a = m_1 \cos(\bar{\omega}t + \bar{\phi}_a) - \frac{m_1}{6}\cos(3\bar{\omega}t + 3\bar{\phi}_a) \tag{4.22}$$

$$m_b = m_1 \cos(\bar{\omega}t + \bar{\phi}_a - \frac{2\pi}{3}) - \frac{m_1}{6}\cos(3\bar{\omega}t + 3\bar{\phi}_a) \tag{4.23}$$

$$m_c = m_1 \cos(\bar{\omega}t + \bar{\phi}_a + \frac{2\pi}{3}) - \frac{m_1}{6}\cos(3\bar{\omega}t + 3\bar{\phi}_a). \tag{4.24}$$

where $\bar{\phi}_a$ is the phase angle of the a-phase fundamental modulation signal. It is noticed that if such three-phase modulations are compared with the same PWM carrier, the components corresponding to multiples of the switching frequency (i.e., $q_{n,0c}$ and $q_{n,0s}$) for the three-phase switching functions are equal. These components can be canceled in (4.19)-(4.21). As a result, no components corresponding to multiples of the switching frequency exist in the inductor currents. It can be seen from (4.6)-(4.10) that the magnitudes of the fundamental and third harmonic components for three-phase switching functions are equal to each other. From (4.11) and (4.12), the magnitudes of high frequency components can be given by

$$\sqrt{q_{n,ic}^2 + q_{n,is}^2} = \sum_{j=-\infty}^{\infty} \frac{2}{n\pi} J_{i-3j}\left(\frac{n\pi m_1}{2}\right) J_j\left(\frac{n\pi m_3}{2}\right) \sin\left(\frac{(n+i-2j)\pi}{2}\right), \quad (4.25)$$

which means that the magnitudes of high frequency components of three-phase switching functions on the same frequency are also equal in the balanced system. Therefore, three-phase switching functions have the same significant harmonic components.

4.3 Simulation Results

In order to examine the proposed inverter GAM model, simulation of the three-phase inverter is discussed in this section. The model is simulated by the ode32tb Simulink solver with a default relative tolerance of 10^{-3} in MATLAB 2013a. The Bessel function of the first kind is implemented using the MATLAB interpreter. The simulation time for each simulation study is 2 s. The run time of the simulation is reported as the mean run time over 100 simulations. The initial values of the state variables in the simulation are equal to the corresponding steady state values.

The structure of the three-phase inverter for the simulation is shown in Figure 4.2. The parameters of the three-phase inverter are listed in the Table 4.1. A modulation signal step change is considered. Two configurations of three-phase inverter GAM

model are studied. In Configuration 1, the switching functions and state variables of the GAM model are represented using 60-Hz components and 9.88-kHz and 10.12-kHz components that are sidebands to the 10-kHz switching frequency. In Configuration 2, the switching functions and state variables of the GAM model are represented using not only all of components in Configuration 1 but also 19.94-kHz and 20.06-kHz components that are sidebands to double the switching frequency. Two configurations are compared with a detailed model that models every switching action. From (4.5)–(4.12), it is can be seen that the coefficients of the switching functions for a given harmonic are an infinite sum except for the dc, fundamental, and third-harmonic injection components. However, these coefficients are approximated by several terms. In particular, the 9.88-kHz component is approximated by the sum of terms with $j \in \{-1, 0\}$. The 10.12-kHz component is approximated by the sum of terms with $j \in \{0, 1\}$. The 19.94-kHz and 20.06-kHz components are approximated by the sum of terms with $j \in \{-1, 0, 1\}$. Because $J_{-y}(x) = (-1)^y J_y(x)$, only four Bessel function evaluations are needed for Configuration 1 of the GAM model and nine Bessel function evaluations are needed for Configuration 2 of the GAM model. The magnitudes of harmonic components of a-phase switching function given by the approximation and the fast Fourier transform (FFT) are compared in Table 4.2. The sampling frequency of a-phase switching function for the FFT is 30 MHz. As mentioned in Section 4.2, the magnitudes of harmonic components of three-phase switching functions on same frequency are equal to each other. So, the magnitudes of harmonic components for b-phase and c-phase switching functions given by the approximation and the FFT have the same results. From Table 4.2, it can be seen that the approximations of QFS coefficients have high accuracy.

Three-phase inductor currents during the first two fundamental periods predicted by the detailed model and by Configuration 1 of the GAM model are shown in Figure 4.4 (a). Three-phase inductor currents near the step modulation signal change

Table 4.1: Three-Phase Inverter Simulation Parameters

Input voltage, V_{dc}	220 V
Inductance of L filter, L	0.276 mH
Load resistance, R	2.2 Ω
Switching frequency, $\hat{f}$	10 kHz
Phase angle of switching function, $\hat{\phi}$	0 rad
Modulation signal frequency, $\bar{f}$	60 Hz
Initial modulation signal, $m_a(t)$ (initial)	$0.9\cos(\bar{\omega}t) - 0.15\cos(3\bar{\omega}t)$
Final modulation signal, $m_a(t)$ (final)	$0.6\cos(\bar{\omega}t + \pi/2) - 0.1\cos(3\bar{\omega}t + 3\pi/2)$
Modulation signal step time	16.7 ms

Table 4.2: Magnitude of A-phase Switching Function Harmonics from Approximation and Fast Fourier Transform

Harmonic frequency			9.88 kHz	10.12 kHz	19.94 kHz	20.06 kHz
Harmonic magnitude	$m_a(t)$ (initial)	FFT	0.0917	0.0917	0.1472	0.1472
		Approximation	0.0917	0.0917	0.1475	0.1475
	$m_a(t)$ (final)	FFT	0.0442	0.0442	0.1953	0.1953
		Approximation	0.0442	0.0442	0.1953	0.1953

are shown in Figure 4.4 (b). From Figure 4.4, it can be seen that the inductor currents predicted by Configuration 1 of the GAM model match the inductor currents predicted by the detailed model during both steady-state and transient conditions.

Three-phase inductor currents during the first two fundamental periods predicted by the detailed model and by Configuration 2 of the GAM model are shown in Figure 4.5 (a). Three-phase inductor currents near the step modulation signal change are shown in Figure 4.5 (b). From Figure 4.5, it can be seen that the inductor currents predicted by Configuration 2 of the GAM model also match the inductor currents predicted by the detailed model.

It can be seen that the accuracy of Configuration 2 of the GAM model is increased (with respect to Configuration 1) by including more sideband components. Furthermore, the accuracy of Configuration 1 of the GAM model noticeably suffers after the modulation signal step change (e.g., i_c at approximately 17 ms). This decrease in accuracy can be understood from Figure 4.1. In Figure 4.1, the magnitudes of the 9.88-kHz and 10.12-kHz sideband components are smaller than the magnitudes

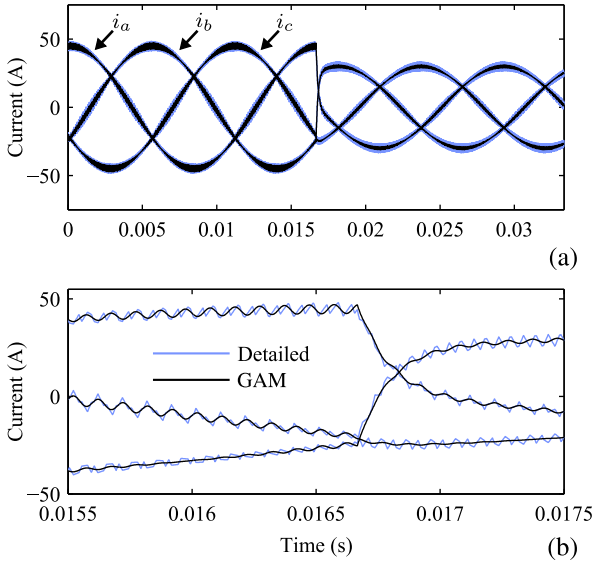

Figure 4.4: Configuration 1 three-phase inverter inductor currents

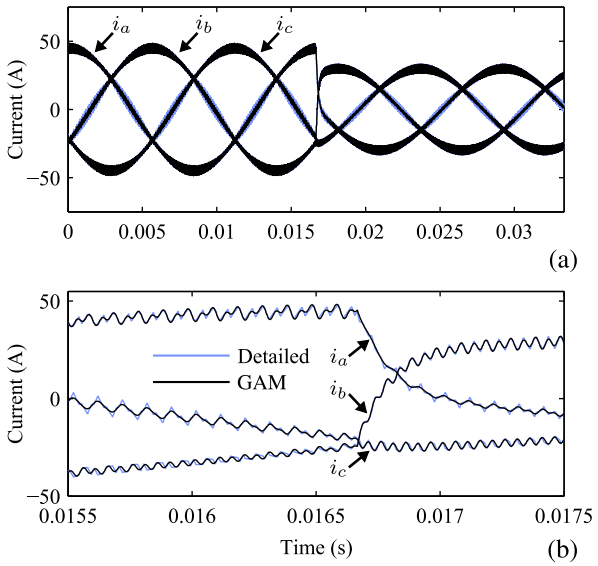

Figure 4.5: Configuration 2 three-phase inverter inductor currents

of the 19.94-kHz and 20.06-kHz sideband components when the magnitude of the fundamental component m_1 is equal to 0.6 (as it is after the step change).

The run times of the detailed model and both configurations of the GAM model are listed in Table 4.3. It can be seen that the average simulation run time of detailed model is more than 67 times larger than that of Configuration 1 of the GAM model.

Table 4.3: Three-Phase Inverter Simulation Run Time

Model	Run time (ms)
Detailed	5162
Configuration 1	76
Configuration 2	140

Table 4.4: Mean Deviation of Three-Phase Inverter Inductor Currents

Model	Inductor current mean deviation (A)		
	a phase	b phase	c phase
Configuration 1	1.131	1.131	1.131
Configuration 2	0.482	0.482	0.482

The average simulation run time of detailed model is more than 35 times larger than that of Configuration 2 of the GAM model. To compare the accuracy of different configurations of the GAM model, the mean deviation between the inductor current of the GAM model and that of the detailed model is defined by

$$\frac{1}{T}\int_0^T \sqrt{(i_{GAM}(t) - i_{detailed}(t))^2}, \tag{4.26}$$

where T is the simulation time, i_{GAM} is the inductor current predicted by the GAM model and $i_{detailed}$ is the inductor current predicted by the detailed model. The mean deviations of three-phase inductor currents are listed in Table 4.4. It can also be seen that the Configuration 2 of the GAM model has better accuracy than Configuration 1 of the GAM model. So, there is a trade-off between the simulation speed and accuracy in the GAM model for three-phase inverters.

4.4 Conclusion

Achieving the proper balance between accuracy and computational efficiency is necessary in any simulation application. Models based on averaging have been used widely with numerous benefits. GAM techniques have been used to predict both average and

switching behavior of converters while retaining the faster simulation speed associated with average-value models. Herein, an GAM model for three-phase PWM inverters with third-harmonic injection is proposed. The QFS representation of the switching functions with third-harmonic injection are necessary for constructing three-phase inverter GAM model. The QFS representation of the switching functions includes fundamental components, third harmonic components, components corresponding to multiples of the switching frequency and sideband components of multiples of the switching frequency. Due to the third harmonic components and components corresponding to multiples of the switching frequency do not exist in the state variables of three-phase inverters, the sideband components of multiples of the switching frequency cause the variations in inductor current ripple magnitude. The accuracy of the GAM model of three-phase inverter can be improved by including more sideband components in average vectors, but the simulation run time will increase. The simulation results show the GAM model have high accuracy and simulation run times that are significantly faster than those associated with detailed models.

Chapter 5

Generalized Average Method in Reference Frame with Varying Modulation Signal Frequency

Herein, the GAM is extended to model PWM inverters with varying fundamental frequency in the reference frame. The QFS representation for the switching function with varying modulation signal frequency is studied. The transformation matrix is used to find the QFS representations of the switching functions in the reference frame. The GAM model in the reference frame can be constructed based on the QFS representations of waveforms and the detailed model state equations in the reference frame. The proposed models are demonstrated both in simulation and experimentally and are found to accurately portray the behavior of the inverter in the reference frame when the magnitude and frequency of the modulation signal are varying. Furthermore, the simulation speed of the GAM model is significantly faster than that of the detailed model in the rotor reference frame. The contributions of this work are (1) the QFS representation of the switching function of three-phase PWM inverters in the reference frame with varying modulation frequency, (2) the proposal

of an GAM model for three-phase PWM inverter with a permanent magnet brushless dc motor in the rotor reference frame, and (3) the demonstration of the proposed GAM model in simulation and experimentally.

The remainder of this chapter is organized as follows. The general approach to constructing the QFS representation of the switching functions of PWM inverters in the reference frame with varying fundamental frequency described in Section 5.1. In Section 5.2, the GAM model for the three-phase inverter with permanent magnet brushless dc motor is proposed. The proposed GAM models are compared with the detailed model in the simulation in Section 5.3. In Section 5.4, the GAM models are demonstrated by comparing their simulation results with experimentally measured waveforms. Finally, conclusions are drawn in Section 5.5.

5.1 Generalized Averaging Method for Inverters in Reference Frame

The general approach for constructing GAM model for PWM inverter with *abc* variables has been described in the previous chapter. For a PWM inverter, a waveform $x(t)$ with varying fundamental frequency is represented as

$$x(t) = x_{0,0} + x_{0,1c}\cos(\bar{\phi}(t)) + x_{0,1s}\sin(\bar{\phi}(t)) + \sum_{n=1}^{\infty}\sum_{i=-\infty}^{\infty} x_{n,ic}\cos(n\hat{\omega}t + i\bar{\phi}(t)) + \sum_{n=1}^{\infty}\sum_{i=-\infty}^{\infty} x_{n,is}\sin(n\hat{\omega}t + i\bar{\phi}(t)), \quad (5.1)$$

where

$$\bar{\phi}(t) = \int_0^t \bar{\omega}(t)dt \quad (5.2)$$

$\hat{\omega}$ is the angular switching frequency and $\bar{\omega}(t)$ is the angular modulation signal frequency. It is noticed that the switching frequency is a constant value and the frequency of the modulation signal is a function of time.

As before, the instantaneous value of the waveform can be approximated as

$$x(t) \approx \mathbf{C}(t)\mathbf{x}, \tag{5.3}$$

where

$$\mathbf{x} = [x_{0,0}\ x_{n_1,i_1c}\ x_{n_1,i_1s}\ \ \ldots\ \ x_{n_o,i_oc}\ x_{n_o,i_os}]^{\mathrm{T}}, \tag{5.4}$$

$$\mathbf{C}(t) = \begin{bmatrix} 1 \\ \cos(n_1\hat{\omega}t + i_1\bar{\phi}(t)) \\ \sin(n_1\hat{\omega}t + i_1\bar{\phi}(t)) \\ \vdots \\ \cos(n_o\hat{\omega}t + i_o\bar{\phi}(t)) \\ \sin(n_o\hat{\omega}t + i_o\bar{\phi}(t)) \end{bmatrix}^{\mathrm{T}}. \tag{5.5}$$

It can be seen that if the frequency of the modulation signal changes, the frequencies of sine and cosine functions in $\mathbf{C}(t)$ also change. The mathematical properties of signals approximated by QFS representations are unchanged. The summary of relevant QFS relationships is already given in Table 3.1.

In order to model PWM inverters, the QFS representation of the switching functions of the PWM inverters with varying modulation frequency is necessary. It is assumed that the modulation signal for the inverter is a sinusoidal waveform with varying frequency. The modulation signal with varying frequency can be expressed by

$$m(t) = m_{0,1c}\cos(\bar{\phi}(t)) + m_{0,1s}\sin(\bar{\phi}(t)) \tag{5.6}$$

$$= m_{0,1}\cos(\bar{\phi}(t) + \bar{\phi}_0), \tag{5.7}$$

where

$$m_{0,1} = \sqrt{m_{0,1c}^2 + m_{0,1s}^2} \tag{5.8}$$

$$\bar{\phi}_0 = \arg(m_{0,1c} - jm_{0,1s}). \tag{5.9}$$

It is noticed that $m_{0,1c}$ and $m_{0,1s}$ are real-valued QFS coefficients. The instantaneous duty cycle can be found from the modulation signal by

$$d(t) = \frac{1}{2}(m(t) + 1). \tag{5.10}$$

It has been shown in [53] that for relatively slowly varying duty cycle, the general periodic switching function can be expressed as the following Fourier series:

$$q(t) = d(t) + \frac{2}{\pi}\sum_{n=1}^{\infty}\frac{\sin(n\pi d(t))}{n}\cos(n\hat{\omega}t + n\hat{\phi}_0), \tag{5.11}$$

where $\hat{\phi}_0$ is the initial phase angle of the switching function. It is assumed that $\bar{\omega}(t)$ is always much less than $\hat{\omega}$ and modulation signal changes slowly with respect to the switching frequency. By expanding (5.11), the general QFS representation of the switching function for sinusoidal modulation signals with varying fundamental frequency can be expressed by

$$\begin{aligned} q(t) = q_{0,0} + q_{0,1c}\cos(\bar{\phi}(t)) + q_{0,1s}\sin(\bar{\phi}(t)) + \sum_{n=1}^{\infty}\sum_{i=-\infty}^{\infty} q_{n,ic}\cos(n\hat{\omega}t + i\bar{\phi}(t)) \\ + \sum_{n=1}^{\infty}\sum_{i=-\infty}^{\infty} q_{n,is}\sin(n\hat{\omega}t + i\bar{\phi}(t)), \end{aligned} \tag{5.12}$$

where

$$q_{0,0} = \frac{1}{2} \tag{5.13}$$

$$q_{0,1c} = \frac{1}{2} m_{0,1c} \tag{5.14}$$

$$q_{0,1s} = \frac{1}{2} m_{0,1s} \tag{5.15}$$

$$q_{n,ic} = \frac{2}{n\pi} \sin\left(\frac{\pi(n+i)}{2}\right) J_i(\frac{nm_{0,1}\pi}{2}) \cos(n\hat{\phi}_0 + i\bar{\phi}_0) \tag{5.16}$$

$$q_{n,is} = -\frac{2}{n\pi} \sin\left(\frac{\pi(n+i)}{2}\right) J_i(\frac{nm_{0,1}\pi}{2}) \sin(n\hat{\phi}_0 + i\bar{\phi}_0). \tag{5.17}$$

Above QFS representation also can be represented by

$$q(t) = q_{0,0} + q_{0,1}(t) + \sum_{n=1}^{\infty} \sum_{i=-\infty}^{\infty} q_{n,i}(t), \tag{5.18}$$

where

$$q_{n,i}(t) = q_{n,i} \cos(\theta_{n,i}(t)) \tag{5.19}$$

$$q_{0,0} = \frac{1}{2} \tag{5.20}$$

$$q_{0,1} = \frac{1}{2} m_{0,1} \tag{5.21}$$

$$q_{n,i} = \frac{2}{n\pi} \sin\left(\frac{\pi(n+i)}{2}\right) J_i(\frac{nm_{0,1}\pi}{2}) \tag{5.22}$$

$$\theta_{n,i}(t) = n\hat{\omega}t + n\hat{\phi}_0 + i\bar{\phi}(t) + i\bar{\phi}_0 \tag{5.23}$$

In a balanced three-phase system, the three-phase modulation signals can be given by

$$m_a(t) = m \cos(\theta(t)) \tag{5.24}$$

$$m_b(t) = m \cos(\theta(t) - \frac{2\pi}{3}) \tag{5.25}$$

$$m_c(t) = m \cos(\theta(t) + \frac{2\pi}{3}) \tag{5.26}$$

where

$$\theta(t) = \bar{\phi}(t) + \bar{\phi}_0. \tag{5.27}$$

By using (5.18), the harmonic components for three-phase switching functions can be found by

$$q_{a,n,i}(t) = q_{n,i}\cos(\theta_{n,i}(t)) \tag{5.28}$$

$$q_{b,n,i}(t) = q_{n,i}\cos(\theta_{n,i}(t) - \frac{2\pi}{3}i) \tag{5.29}$$

$$q_{c,n,i}(t) = q_{n,i}\cos(\theta_{n,i}(t) + \frac{2\pi}{3}i). \tag{5.30}$$

The general QFS representation of the switching function in the reference frame can be found from the general QFS representation of the switching function for *abc* variables by using the transformation matrix. The transformation matrix for the reference frame is defined by

$$\mathbf{K} = \frac{2}{3}\begin{bmatrix} \cos(\theta_{ref}(t)) & \cos(\theta_{ref}(t) - \frac{2\pi}{3}) & \cos(\theta_{ref}(t) + \frac{2\pi}{3}) \\ \sin(\theta_{ref}(t)) & \sin(\theta_{ref}(t) - \frac{2\pi}{3}) & \sin(\theta_{ref}(t) + \frac{2\pi}{3}) \\ \frac{1}{2} & \frac{1}{2} & \frac{1}{2} \end{bmatrix}, \tag{5.31}$$

where

$$\theta_{ref}(t) = \int_0^t \omega_{ref}(t)dt + \phi_{0,ref} = \phi_{ref}(t) + \phi_{0,ref}, \tag{5.32}$$

$\phi_{0,ref}$ is the initial phase angle of the reference frame. The harmonic components of switching functions in the reference frame are related with those for *abc* variables by the following equation:

$$\begin{bmatrix} q_{q,n,i}(t) \\ q_{d,n,i}(t) \\ q_{0,n,i}(t) \end{bmatrix} = \mathbf{K}\begin{bmatrix} q_{a,n,i}(t) \\ q_{b,n,i}(t) \\ q_{c,n,i}(t) \end{bmatrix}. \tag{5.33}$$

By simplifying (5.33), the harmonic components of switching functions in the reference frame can be found by

$$q_{q,n,i}(t) = \begin{cases} 0, & i = 3x \\ q_{n,i}\cos(\theta_{n,i}(t) - \theta_{ref}(t)), & i = 3x+1 \\ q_{n,i}\cos(\theta_{n,i}(t) + \theta_{ref}(t)), & i = 3x+2 \end{cases} \tag{5.34}$$

$$q_{d,n,i}(t) = \begin{cases} 0, & i = 3x \\ -q_{n,i}\sin(\theta_{n,i}(t) - \theta_{ref}(t)), & i = 3x+1 \\ q_{n,i}\sin(\theta_{n,i}(t) + \theta_{ref}(t)), & i = 3x+2 \end{cases} \tag{5.35}$$

$$q_{0,n,i}(t) = \begin{cases} q_{n,i}\cos(\theta_{n,i}(t)), & i = 3x \\ 0, & i = 3x+1 \\ 0, & i = 3x+2 \end{cases} \tag{5.36}$$

where x is an integer. It can be seen that the QFS coefficients of the switching functions in the reference frame vary with the index i. The QFS representations of switching functions in the reference frame can be found by

$$\begin{aligned} q_y(t) = q_{y,0,0} &+ q_{y,0,1c}\cos(\bar{\phi}(t) + f(i)\phi_{ref}(t)) \\ &+ q_{y,0,1s}\sin(\bar{\phi}(t) + f(i)\phi_{ref}(t)) \\ &+ \sum_{n=1}^{\infty}\sum_{i=-\infty}^{\infty} q_{y,n,ic}\cos(n\hat{\omega}t + i\bar{\phi}(t) + f(i)\phi_{ref}(t)) \\ &+ \sum_{n=1}^{\infty}\sum_{i=-\infty}^{\infty} q_{y,n,is}\sin(n\hat{\omega}t + i\bar{\phi}(t) + f(i)\phi_{ref}(t)), \end{aligned} \tag{5.37}$$

where

$$f(i) = \begin{cases} 0, & i = 3x \\ -1, & i = 3x+1 \\ 1, & i = 3x+2 \end{cases}, \tag{5.38}$$

Table 5.1: Quasi-Fourier Series Coefficients of Switching Function in Reference Frame

i	$3x$	$3x+1$	$3x+2$
$q_{q,n,ic}$	0	$q_{n,i}\cos(n\hat{\phi}_0 + i\bar{\phi}_0 - \phi_{0,ref})$	$q_{n,i}\cos(n\hat{\phi}_0 + i\bar{\phi}_0 + \phi_{0,ref})$
$q_{q,n,is}$	0	$-q_{n,i}\sin(n\hat{\phi}_0 + i\bar{\phi}_0 - \phi_{0,ref})$	$-q_{n,i}\sin(n\hat{\phi}_0 + i\bar{\phi}_0 + \phi_{0,ref})$
$q_{d,n,ic}$	0	$-q_{n,i}\sin(n\hat{\phi}_0 + i\bar{\phi}_0 - \phi_{0,ref})$	$q_{n,i}\sin(n\hat{\phi}_0 + i\bar{\phi}_0 + \phi_{0,ref})$
$q_{d,n,is}$	0	$-q_{n,i}\cos(n\hat{\phi}_0 + i\bar{\phi}_0 - \phi_{0,ref})$	$q_{n,i}\cos(n\hat{\phi}_0 + i\bar{\phi}_0 + \phi_{0,ref})$
$q_{0,n,ic}$	$q_{n,i}\cos(n\hat{\phi}_0 + i\bar{\phi}_0)$	0	0
$q_{0,n,is}$	$-q_{n,i}\sin(n\hat{\phi}_0 + i\bar{\phi}_0)$	0	0

$$q_{y,0,0} = \begin{cases} 0, & y = q \\ 0, & y = d \\ q_{0,0}, & y = 0 \end{cases} . \tag{5.39}$$

The QFS coefficients of switching function in the reference frame are listed in Table 5.1.

The most significant components of the Fourier spectrum for *abc* variables are discussed in the previous chapter. It can be seen from (5.19), (5.34), (5.35), and (5.36) that the magnitudes of harmonic components of switching functions in the reference frame are equal to those for *abc* variables. As a result, the same significant components can be selected to construct the average vector for the GAM model in the reference frame.

5.2 Inverter Generalized Averaging Method Models in Reference Frame

The three-phase inverter with a permanent magnet brushless dc motor is shown in Figure 5.1. The detailed model state equations in the rotor reference frame are given

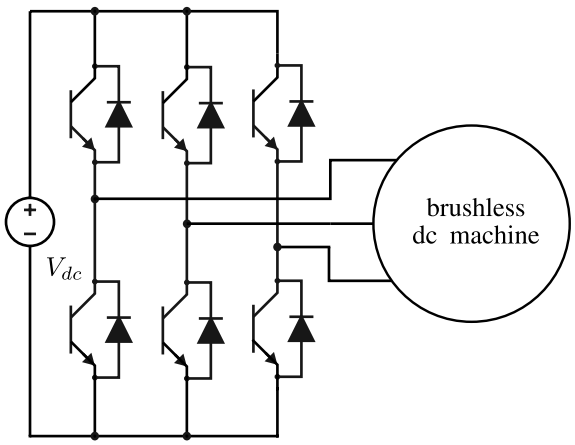

Figure 5.1: Three-phase inverter with brushless dc motor

by

$$L_q \frac{di^r_{qs}(t)}{dt} = V_{dc} q^r_{qs}(t) - r_s i^r_{qs}(t) - \omega_r L_d i^r_{ds}(t) - \omega_r \lambda'^r_m \tag{5.40}$$

$$L_d \frac{di^r_{ds}(t)}{dt} = V_{dc} q^r_{ds}(t) - r_s i^r_{ds}(t) + \omega_r L_q i^r_{qs}(t) \tag{5.41}$$

$$L_{ls} \frac{di^r_{0s}(t)}{dt} = V_{dc} q^r_{0s}(t) - r_s i^r_{0s}(t). \tag{5.42}$$

where λ_m is the flux linkage due to the permanent magnet, L_q is the q-axis inductance, L_d is the d-axis inductance, and r_s is the stator resistance. The instantaneous switching functions in the rotor reference frame can be found by

$$\begin{bmatrix} q^r_{qs}(t) \\ q^r_{ds}(t) \\ q^r_{0s}(t) \end{bmatrix} = \mathbf{K}^r \left(\begin{bmatrix} q_a(t) \\ q_b(t) \\ q_c(t) \end{bmatrix} - \frac{1}{3}(q_a(t) + q_b(t) + q_c(t)) \right) \tag{5.43}$$

$$= \begin{bmatrix} q^r_{qs}(t) \\ q^r_{ds}(t) \\ 0 \end{bmatrix}, \tag{5.44}$$

where $\mathbf{K}^r$ is the transformation matrix for the rotor reference frame. It can be seen that the harmonic components in $q^r_{0s}(t)$ are canceled in the balanced three-phase

system. The state equations can be simplified to

$$L_q \frac{di^r_{qs}(t)}{dt} = V_{dc} q^r_{qs}(t) - r_s i^r_{qs}(t) - \omega_r L_d i^r_{ds}(t) - \omega_r \lambda'^r_m \tag{5.45}$$

$$L_d \frac{di^r_{ds}(t)}{dt} = V_{dc} q^r_{ds}(t) - r_s i^r_{ds}(t) + \omega_r L_q i^r_{qs}(t) \tag{5.46}$$

By representing $i_z(t)$ with $\mathbf{i}_z$, $q_z(t)$ with $\mathbf{q}_z$, where $z \in \{qs, ds\}$, the following state equations for the GAM model in the reference frame are found:

$$L_q \frac{d\mathbf{i}^r_{qs}}{dt} = V_{dc} \mathbf{q}^r_{qs} - (r_s \mathbf{I} + L_q \mathbf{T}) \mathbf{i}^r_{qs} - \omega_r L_d \mathbf{i}^r_{ds} - \omega_r \lambda'^r_m \mathbf{I} \tag{5.47}$$

$$L_d \frac{d\mathbf{i}^r_{ds}}{dt} = V_{dc} \mathbf{q}^r_{ds} - (r_s \mathbf{I} + L_d \mathbf{T}) \mathbf{i}^r_{ds} + \omega_r L_q \mathbf{i}^r_{qs} \tag{5.48}$$

where $\mathbf{I}$ is the identity matrix and $\mathbf{T}$ is a $(2o+1)\times(2o+1)$ matrix in which all elements are zero except for the $(2k, 2k+1)$ elements with values $n_k\hat{\omega}+i_k\bar{\omega}(t)+f(i_k)\omega_{ref}(t)$ and the $(2k+1, 2k)$ elements with values $-(n_k\hat{\omega}+i_k\bar{\omega}(t)+f(i_k)\omega_{ref}(t))$ for $k \in \{1, 2, \ldots o\}$. It has been shown in Figure 3.2 that the most significant components of the switching function include dc, the fundamental frequency $\bar{\omega}(t)$, the switching frequency $\hat{\omega}$, and the second-order sideband components of the switching frequency $\hat{\omega} \pm 2\bar{\omega}(t)$. The dc and switching frequency $\hat{\omega}$ components can be canceled if their initial values are equal to zero. For Configuration 1, the average vectors can be given by

$$\mathbf{x} = [x_{0,1c}\ x_{0,1s}\ x_{1,-2c}\ x_{1,-2s}\ x_{1,2c}\ x_{1,2s}]^{\mathrm{T}} \tag{5.49}$$

where $x \in \{i_{qs}, i_{ds}, q_{qs}, q_{ds}\}$ and $\mathbf{x}$ is the corresponding average vector. This representation is referred to as Configuration 1 in Section 5.3 below.

For Configuration 2, the first-order sideband components of double the switching frequency $2\hat{\omega} \pm \bar{\omega}(t)$ is also included, the average vectors can be given by

$$\mathbf{x} = [x_{0,1c}\ x_{0,1s}\ x_{1,-2c}\ x_{1,-2s}\ x_{1,2c}\ x_{1,2s}\ x_{2,-1c}\ x_{2,-1s}\ x_{2,1c}\ x_{2,1s}]^{\mathrm{T}}, \tag{5.50}$$

Table 5.2: Three-phase Inverter Simulation Parameter

Input voltage, V_{dc}	250 V
Switching frequency, $\hat{f}$	10 kHz
Switching function phase, $\hat{\phi}_0$	0 rad
Rotor reference frame initial phase, $\phi_{0,ref}$	0.9 rad

This representation is referred to as Configuration 2 in Section 5.3 below.

5.3 Simulation Results

In order to examine the proposed inverter GAM model in the reference frame, simulations of three-phase inverters in the reference frame are discussed in this section. As before, all of the models are simulated by the ode32tb Simulink solver with a default relative tolerance of 10^{-3} in MATLAB 2013a. The Bessel function of the first kind is implemented using the MATLAB interpreter. The simulation time for each simulation study is 2 s. In each simulation study, a detailed model and two configurations of the GAM model in the reference frame are compared. Plots comparing simulation waveforms on the order of the fundamental period and on the order of the switching period are shown. The run time of the simulation is reported as the mean run time over 100 simulations. The initial values of the state variables in all of the simulations are equal to the corresponding steady state values. It is noticed that the frequency of rotor reference frame ω_r is always equal to the frequency of modulation signal $\bar{\omega}(t)$ in all of the simulations. The structure of the three-phase inverter with a permanent magnet brushless dc motor is shown in Figure 5.1. The parameters of the three-phase inverter are listed in Table 5.2 and the parameters of the permanent magnet brushless dc motor are listed in Table 5.3.

Two configurations of the GAM model in the reference frame are considered. In Configuration 1, the waveforms of the GAM model are represented using fundamental frequency $\bar{\omega}(t)$ components and $\hat{\omega} \pm 2\bar{\omega}(t)$ components that are sidebands to the

Table 5.3: Brushless dc Motor Parameter

Number of poles, P	6
Flux linkage due to permanent magnet, λ_m	0.277 Wb
q-axis inductance, L_q	1.297 mH
d-axis inductance, L_d	1.316 mH
Stator resistance, r_s	0.1 Ω

switching frequency. In Configuration 2, the components of Configuration 1 are used as well as $2\hat{\omega} \pm \bar{\omega}(t)$ components that are sidebands to double the switching frequency. Each of these configurations is compared with a detailed model that models the detailed behavior of each switch.

5.3.1 Simulation results of modulation signal magnitude change

A step change for the magnitude of the modulation signal is considered. The modulation signal steps from $0.82\cos(120\pi t + 1)$ to $0.85\cos(120\pi t + 1)$ at 0.0167 s.

Figure 5.2 (a) shows the q-axis currents during the first five fundamental periods predicted by the detailed model and Configuration 1 of the GAM model. Figs. 5.2 (b) and (c) show these waveforms in closer proximity to the modulation signal magnitude change. Figure 5.3 (a) shows the d-axis currents during the first five fundamental periods predicted by the detailed model and Configuration 1 of the GAM model. Figs. 5.3 (b) and (c) show these waveforms in closer proximity to the modulation signal magnitude change. It can be seen that the current ripple predicted by Configuration 1 of the GAM model in the rotor reference frame matches that predicted by the detailed model in the rotor reference frame during the steady state and transient conditions.

Figure 5.4 (a) shows the q-axis currents during the first five fundamental periods predicted by the detailed model and Configuration 2 of the GAM model. Figs. 5.4 (b) and (c) show these waveforms in closer proximity to the modulation signal magnitude change. Figure 5.5 (a) shows the d-axis currents during the first five fundamental

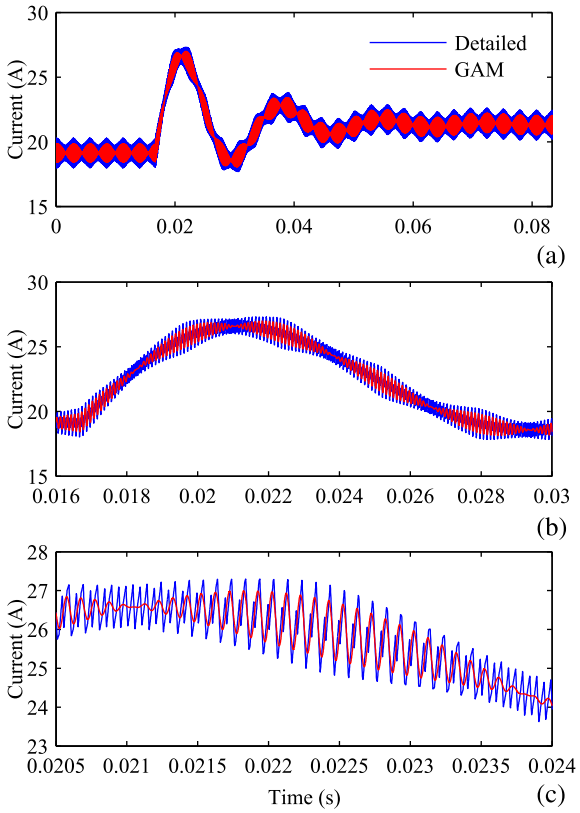

Figure 5.2: Configuration 1 q-axis current with modulation signal magnitude step change

periods predicted by the detailed model and Configuration 2 of the GAM model. Figs. 5.5 (b) and (c) show these waveforms in closer proximity to the modulation signal magnitude change. It can be seen that the current ripple predicted by Configuration 2 of the GAM model in the rotor reference frame matches that predicted by the detailed model during the steady state and transient conditions.

The run times of Configurations 1 and 2 of the GAM model and the detailed model are shown in Table 5.4. It can be seen that the simulation speed of Configurations 1 of the GAM model is more than 24 times faster than that of the detailed model. Both configurations of the GAM model in the reference frame predict the switching ripple components of the waveforms like the detailed model, but Configuration 2 provides

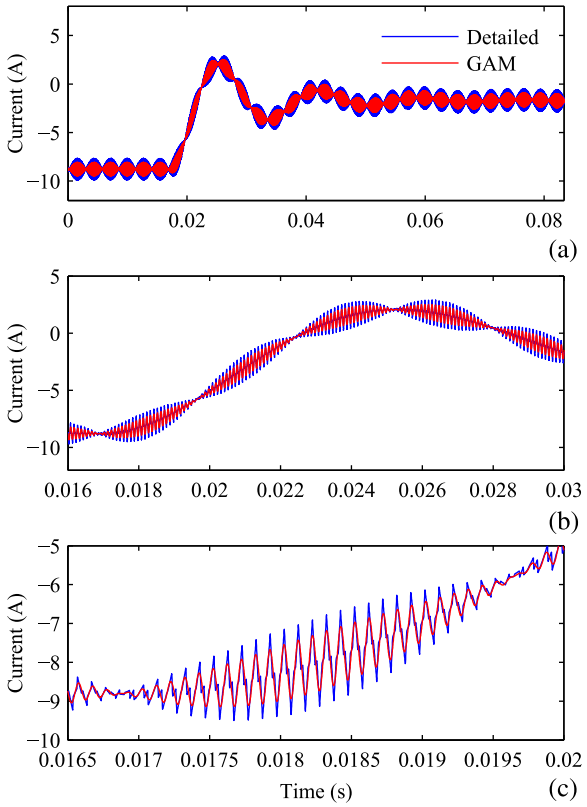

Figure 5.3: Configuration 1 d-axis current with modulation signal magnitude step change

Table 5.4: Simulation Run Time for Stepping Modulation Signal Magnitude

Model	Run time (ms)
Configuration 1	246
Configuration 2	1224
Detailed	6030

better predictions of these components. The run time of Configuration 2 of the GAM model in the reference frame is larger than the run time of Configuration 1 in the reference frame because of the additional complexity associated with including the sideband components.

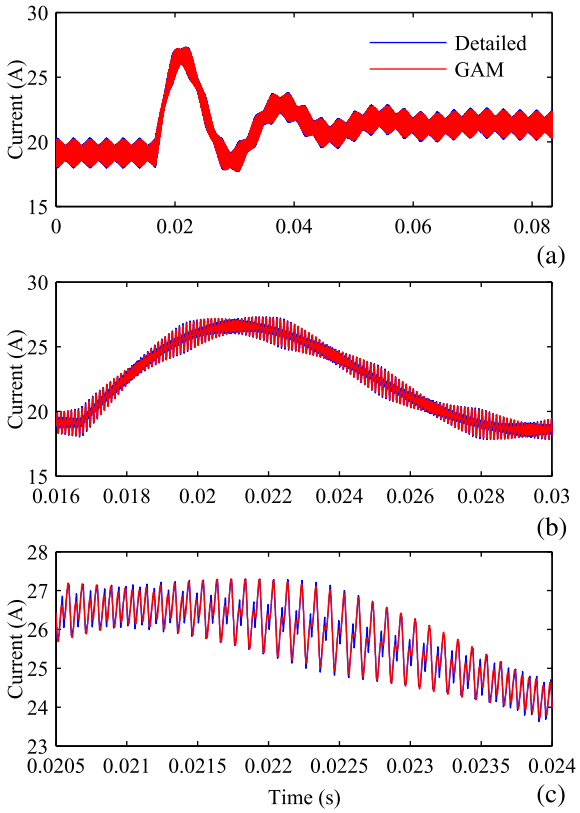

Figure 5.4: Configuration 2 q-axis current with modulation signal magnitude step change

5.3.2 Simulation results of modulation signal speed change

A step change for the speed of the modulation signal is considered. The initial modulation signal is $0.82\cos(120\pi t + 1)$. At 0.0167 s, the speed of the modulation signal step to 110π rad/s.

Figure 5.6 (a) shows the q-axis currents during the first five fundamental periods predicted by the detailed model and Configuration 1 of the GAM model. Figs. 5.6 (b) and (c) show these waveforms in closer proximity to the modulation signal frequency change. Figure 5.7 (a) shows the d-axis currents during the first five fundamental periods predicted by the detailed model and Configuration 1 of the GAM model. Figs. 5.7 (b) and (c) show these waveforms in closer proximity to the modulation signal

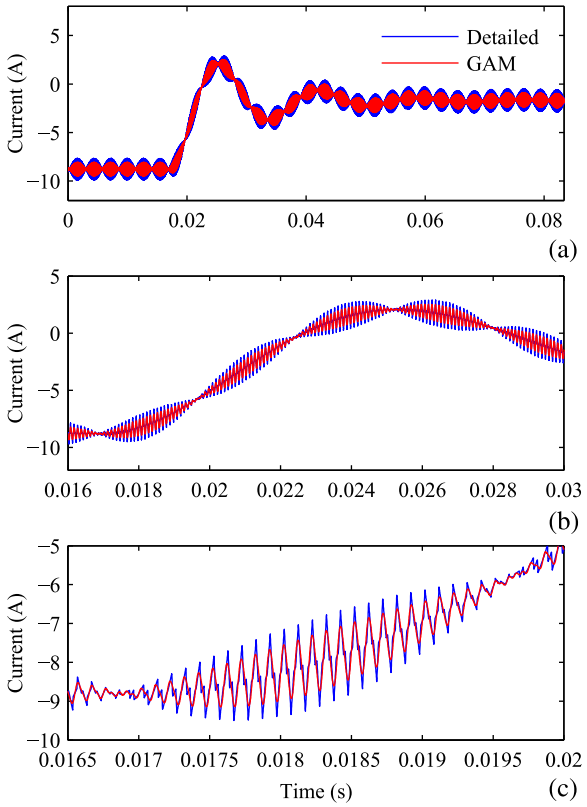

Figure 5.5: Configuration 2 d-axis current with modulation signal magnitude step change

frequency change. It can be seen that the current ripple predicted by Configuration 1 of the GAM model in the rotor reference frame matches that predicted by the detailed model during the steady state and transient conditions.

Figure 5.8 (a) shows the q-axis currents during the first five fundamental periods predicted by the detailed model and Configuration 2 of the GAM model. Figs. 5.8 (b) and (c) show these waveforms in closer proximity to the modulation signal frequency change. Figure 5.9 (a) shows the d-axis currents during the first five fundamental periods predicted by the detailed model and Configuration 2 of the GAM model. Figs. 5.9 (b) and (c) show these waveforms in closer proximity to the modulation signal frequency change. It can be seen that the current ripple predicted by Configuration 2

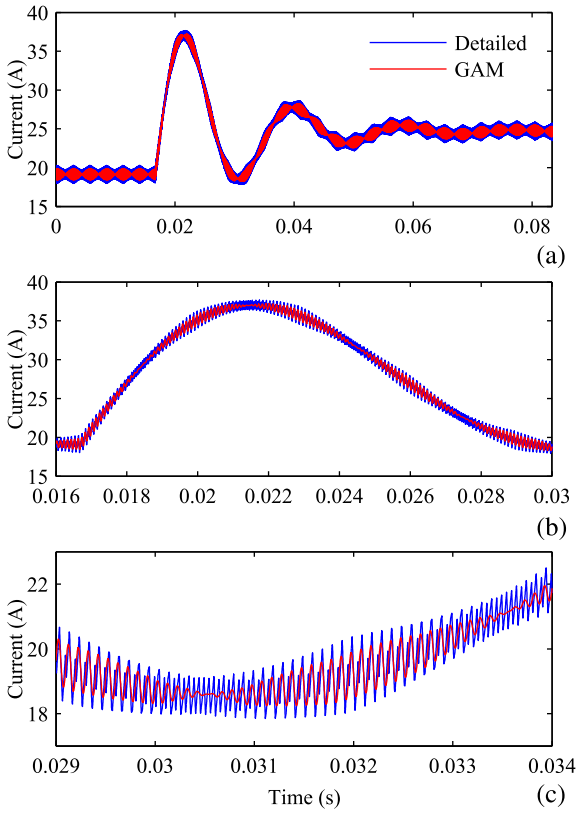

Figure 5.6: Configuration 1 q-axis current with rotor speed step change

of the GAM model in the rotor reference frame matches that predicted by the detailed model during the steady state and transient conditions. By comparing 5.6 (c) and 5.8 (c), it can be seen that Configurations 2 of the GAM model has better accuracy than Configurations 1 of the GAM model.

The run times of Configurations 1 and 2 of the GAM model and the detailed model are shown in Table 5.5. It can be seen that the simulation speed of Configurations 1 of the GAM model is more than 100 times faster than that of the detailed model. And the simulation speed of Configurations 2 of the GAM model is more than 20 times faster than that of the detailed model.

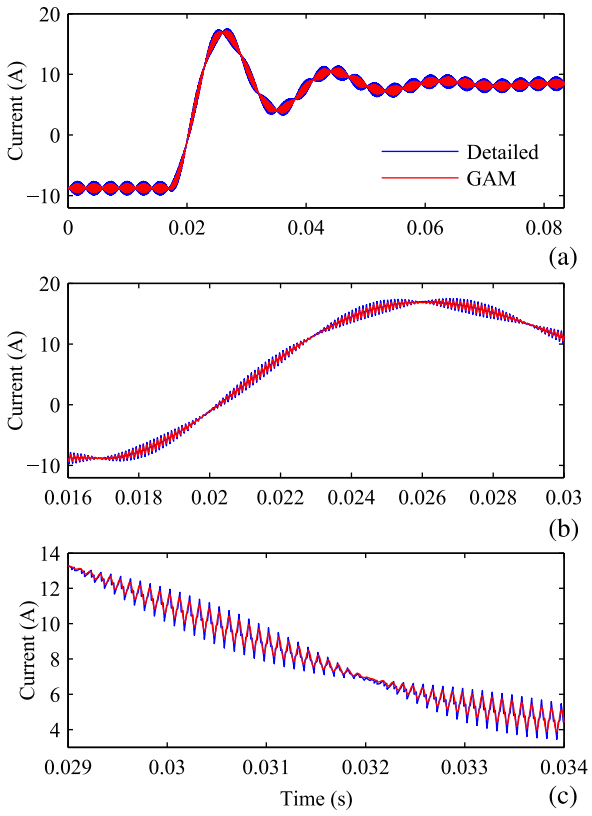

Figure 5.7: Configuration 1 *d*-axis current with rotor speed step change

Table 5.5: Simulation Run Time for Stepping Modulation Signal Frequency

Model	Run time (ms)
Configuration 1	41
Configuration 2	236
Detailed	5814

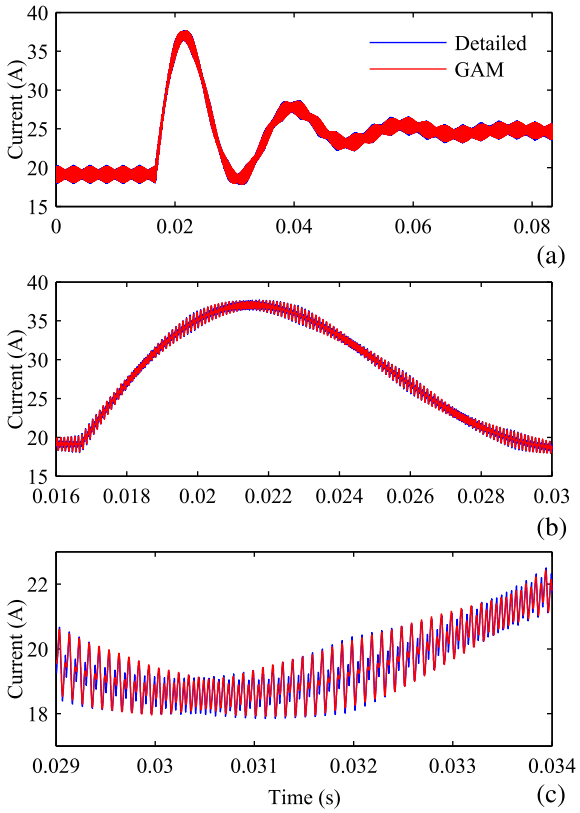

Figure 5.8: Configuration 2 q-axis current with rotor speed step change

5.4 Experimental Results

To demonstrate the proposed GAM model in the reference frame, it is compared with experimental measurements in this section. It is noticed that the waveforms from GAM model shown in Figure 5.10 and Figure 5.11 are simulated in the rotor reference frame and transferred to *abc* waveforms. A prototype inverter is connected with a permanent magnet brushless dc machine. The inverter is controlled by using a TMS320F28335 microcontroller. The sampling rates of the analog-to-digital converter and the controller are 100 kHz. The parameter of the permanent magnet brushless dc motor is shown in Table 5.3. The GAM model and the controller in DSP are implemented in the rotor reference frame.

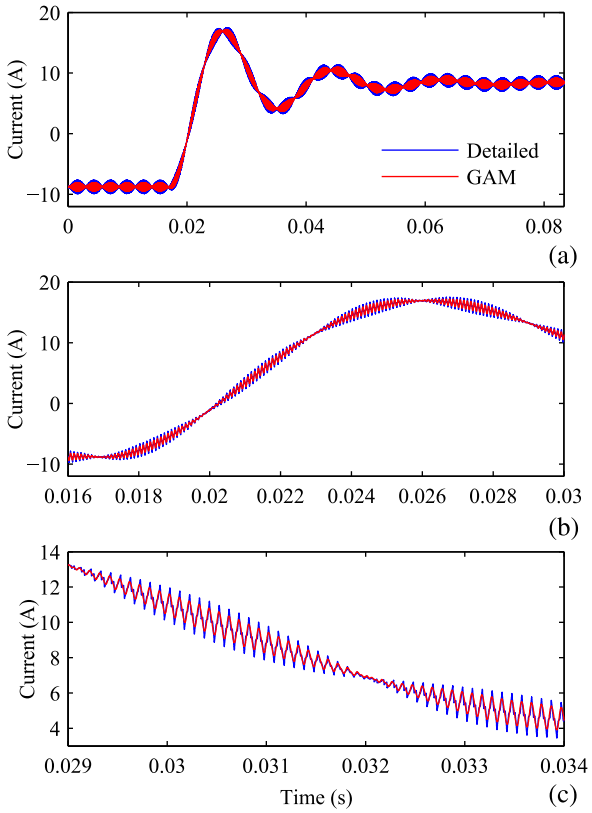

Figure 5.9: Configuration 2 d-axis current with rotor speed step change

5.4.1 Experimental results of current magnitude change

A step change in the reference current i_{qs}^{r*} and i_{ds}^{r*} is studied. The parameters of the inverter are listed in Table 5.6. A PI controller is used to ensure that the output current follows the reference current. The control equations are given by

$$m_q = k_p(i_{qs}^{r*} - \bar{i}_{qs}^{r}) + k_i \int (i_{qs}^{r*} - \bar{i}_{qs}^{r})dt + \frac{2(\omega_r^* L_d i_{ds}^{r*} + \omega_r^* \lambda_m'^{r})}{V_{dc}} \tag{5.51}$$

$$m_d = k_p(i_{ds}^{r*} - \bar{i}_{ds}^{r}) + k_i \int (i_{ds}^{r*} - \bar{i}_{ds}^{r})dt - \frac{2\omega_r^* L_q i_{qs}^{r*}}{V_{dc}}, \tag{5.52}$$

Table 5.6: Inverter Experimental Parameters for Current Magnitude Change

Input voltage, V_{dc}	250 V
Proportional gain, k_p	0.09 A^{-1}
Integral gain, k_i	8.6 $A^{-1}s^{-1}$
Switching frequency, $\hat{f}$	10 kHz
Rotor speed, ω_r	120π rad/s
Initial q-axis reference current, i_{qs}^{r*}	15 A
Final q-axis reference current, i_{qs}^{r*}	10 A
Initial d-axis reference current, i_{ds}^{r*}	0 A
Final d-axis reference current, i_{ds}^{r*}	0 A

where $\bar{i}_{qs}^{r}$ and $\bar{i}_{ds}^{r}$ are the q-axis and d-axis motor current filtered by a second-order low-pass filter in the rotor reference frame with a time constant of 53.1 µs. The rotor speed and rotor angle are obtained by an electrical rotor position observor based on the information from the Hall-effect sensors. Because the second-order low-pass filter is used to filter the ripple of the q-axis and d-axis motor current, the effect of high-frequency motor current harmonics on the modulation signal is considered negligible. The GAM model of the PI controller only includes the $\bar{\omega}(t)$ component of the q-axis and d-axis motor current. The QFS components of the switching function in the rotor reference frame are calculated from the output from the PI controller.

Fig. 5.10 (a) shows the motor currents predicted by the GAM model compared with those measured experimentally. Fig. 5.10 (b) shows these waveforms in closer proximity to the reference current step change. The waveforms are sampled at 20 MHz. In Figure 5.10, the motor currents predicted by the GAM model is represented by the Configuration 2 of GAM model in Section 5.3. It can be seen that the magnitude of the motor current ripple predicted by the GAM model follows the variation that was observed experimentally during the steady state and transient.

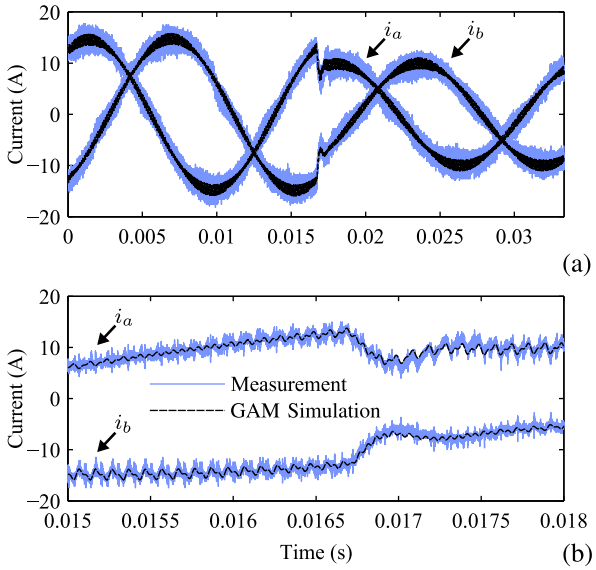

Figure 5.10: Motor current with reference current magnitude change

Table 5.7: Inverter Experimental Parameters for Rotor Speed Change

Input voltage, V_{dc}	250 V
Proportional gain, k_p	0.09 A^{-1}
Integral gain, k_i	8.6 $A^{-1}s^{-1}$
Switching frequency, $\hat{f}$	10 kHz
q-axis reference current, i_{qs}^{r*}	15 A
d-axis reference current, i_{qs}^{r*}	0 A

5.4.2 Experimental results of rotor speed change

An incremental change in the rotor speed ω_r is studied in this subsection. The parameters of the inverter are listed in Table 5.7.

As before, A PI controller is used. However, the PI controller does not have the feed-forward term in this experiment. The PI control equations are given by

$$\begin{aligned} m_q &= k_p(i_{qs}^{r*} - \bar{i}_{qs}^{r}) + k_i \int (i_{qs}^{r*} - \bar{i}_{qs}^{r})dt \\ m_d &= k_p(i_{ds}^{r*} - \bar{i}_{ds}^{r}) + k_i \int (i_{ds}^{r*} - \bar{i}_{ds}^{r})dt, \end{aligned} \tag{5.53}$$

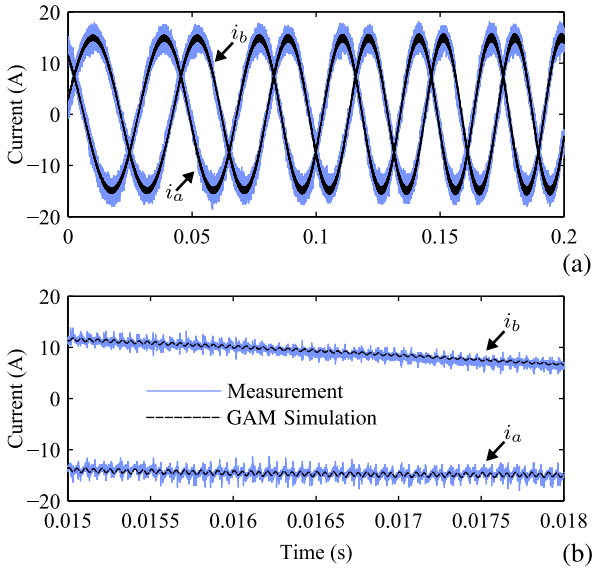

Figure 5.11: Motor current with rotor speed change

A second-order low-pass filter with a time constant of 53.1 µs is used to filter the motor current ripple in the rotor reference frame. The GAM model of the PI controller only includes the $\bar{\omega}(t)$ component of the q-axis and d-axis motor current. The QFS components of the switching function in the rotor reference frame are calculated from the output from the PI controller.

Figs. 5.11 (a) shows the motor currents predicted by the GAM model compared with those measured experimentally. Figs. 5.11 (b) shows these waveforms in closer proximity to the rotor speed change. The waveforms are sampled at 5 MHz. In Figure 5.11, the motor currents predicted by the GAM model are represented by the Configuration 2 of GAM model in Section 5.3. It can be seen that the magnitude of the motor current ripple predicted by the GAM model follows the variation that was observed experimentally when the rotor speed is increasing.

5.5 Conclusion

Herein, GAM models in the reference frame for three-phase PWM inverters with varying fundamental frequency are proposed. Those models are based on the QFS representations of the switching functions in the reference frame. Those models are compared with the detailed model in the reference frame in simulations, and it is found that the GAM models match the detailed model in the reference frame when the frequency of modulation signal is varying. Furthermore, the GAM models are found to have significantly faster simulation speeds than those associated with the detailed model in the reference frame. These models are also demonstrated experimentally, and it is found that the simulation results from the GAM model match the experimental measurements in the steady state and transient.

Chapter 6

Reactive Power Control Methods for Photovoltaic Inverters to Mitigate Short-Term Voltage Magnitude Fluctuations

In this chapter, several reactive power control methods of the form proposed in [80] are proposed. The work described in this chapter has been published in [92]. The primary developments of this chapter with respect to [80] are (1) the consideration of unbalanced reactive power injection, (2) the demonstration of the proposed methods with a more complex system (123 buses vs. 5 buses), and (3) the demonstration of the proposed reactive power control methods with multiple PV sources.

The contributions of this work are (1) the proposal of various reactive power control methods for mitigation of short-term voltage magnitude fluctuations, (2) the definition of performance metrics to assess the performance of the reactive power control methods, and (3) the demonstration of the reactive power control methods over several cases on a well-defined test system. The remainder of this chapter is

organized as follows. The reactive power control methods are described in Section 6.1. In Section 6.2, performance metrics are defined for assessment of the reactive power controller performance. The controllers are demonstrated and their performance is assessed in the presence of single and multiple PV sources in Section 6.3. Finally, conclusions are presented in Section 6.4.

6.1 Reactive Power Control Methods

At a given bus, various reactive power control methods are proposed to allow a three-phase PV inverter to adjust its three-phase reactive power injections in response to fluctuations in solar power. These controllers can be expressed in the form

$$\mathbf{Q} = \mathbf{Q}^* + \boldsymbol{\beta}\Delta P_s, \tag{6.1}$$

where

$$\Delta P_s = P_s - P_s^*, \tag{6.2}$$

P_s is the solar power, P_s^* is the reference solar power, $\mathbf{Q} \in \mathbb{R}^3$ is a vector of the three-phase reactive power injections of the PV inverter, $\mathbf{Q}^* \in \mathbb{R}^3$ is a vector of the three-phase reference reactive power injections of the PV inverter, and $\boldsymbol{\beta} \in \mathbb{R}^3$ is a vector containing control parameters, which are called the substitution rates, that are specific to the given reactive power control method. The objective of this controller is to mitigate against system voltage magnitude variations caused by fluctuating PV real power injection. Alternative methods of choosing the control parameters contained in $\boldsymbol{\beta}$ are studied herein.

All else being equal, the magnitudes of the system voltages can be expressed as a function of the three-phase PV real and reactive power injections at a given bus:

$$\mathbf{V} = \mathbf{f}(\mathbf{P}, \mathbf{Q}), \tag{6.3}$$

where $\mathbf{V} \in \mathbb{R}^m$ is a vector containing bus voltage magnitudes, m is equal to the number of system buses, and $\mathbf{P} \in \mathbb{R}^3$ is a vector containing the three-phase real power injections of the PV inverter. Herein, each phase of a polyphase bus is treated as a separate bus. If Taylor series expansion is performed about the operating point $(\mathbf{P}^*, \mathbf{Q}^*)$, (6.3) can be approximated as

$$\Delta\mathbf{V} \approx \boldsymbol{\alpha}_P \Delta\mathbf{P} + \boldsymbol{\alpha}_Q \Delta\mathbf{Q}, \tag{6.4}$$

where

$$\Delta\mathbf{V} = \mathbf{V} - \mathbf{V}^* = \mathbf{f}(\mathbf{P}, \mathbf{Q}) - \mathbf{f}(\mathbf{P}^*, \mathbf{Q}^*) \tag{6.5}$$

$$\Delta\mathbf{P} = \mathbf{P} - \mathbf{P}^* \tag{6.6}$$

$$\Delta\mathbf{Q} = \mathbf{Q} - \mathbf{Q}^* = \boldsymbol{\beta}\Delta P_s \tag{6.7}$$

$$\boldsymbol{\alpha}_P = \left.\frac{\partial \mathbf{f}}{\partial \mathbf{P}}\right|_{(\mathbf{P},\mathbf{Q})=(\mathbf{P}^*,\mathbf{Q}^*)} \tag{6.8}$$

$$\boldsymbol{\alpha}_Q = \left.\frac{\partial \mathbf{f}}{\partial \mathbf{Q}}\right|_{(\mathbf{P},\mathbf{Q})=(\mathbf{P}^*,\mathbf{Q}^*)}. \tag{6.9}$$

The partial derivative terms $\boldsymbol{\alpha}_P$ and $\boldsymbol{\alpha}_Q$ are called sensitivity factors which can be estimated using small perturbations [80] or calculated by the power flow algorithm at the operating point. The real power injections of the PV inverter are assumed to be balanced. Furthermore, it is assumed that a sufficiently fast MPPT algorithm is

applied that the three-phase real power injections can be expressed as

$$\mathbf{P} = \frac{1}{3}\begin{bmatrix}1 & 1 & 1\end{bmatrix}^{\mathrm{T}} P_s. \tag{6.10}$$

Similarly, the three-phase reference real power injections are expressed as

$$\mathbf{P}^* = \frac{1}{3}\begin{bmatrix}1 & 1 & 1\end{bmatrix}^{\mathrm{T}} P_s^*, \tag{6.11}$$

and substitution of (6.10) and (6.11) into (6.6) yields the following expression for the three-phase incremental real power injections:

$$\Delta\mathbf{P} = \frac{1}{3}\begin{bmatrix}1 & 1 & 1\end{bmatrix}^{\mathrm{T}} \Delta P_s. \tag{6.12}$$

By substitution of (6.7) and (6.12) into (6.4), the incremental magnitudes of the system voltages can be approximated as

$$\Delta\mathbf{V} \approx \left(\frac{1}{3}\boldsymbol{\alpha}_P \begin{bmatrix}1 & 1 & 1\end{bmatrix}^{\mathrm{T}} + \boldsymbol{\alpha}_Q\boldsymbol{\beta}\right)\Delta P_s. \tag{6.13}$$

It can be seen that choice reactive power control method, i.e., choice of $\boldsymbol{\beta}$, can influence the response of the system voltage magnitudes to solar power fluctuations. Each reactive power control method discussed herein is defined by selecting a scope, an objective, and a domain. The possible scopes, objectives, and domains are described below.

6.1.1 Local vs. Global Scope

The scope of a method indicates the buses at which the voltage magnitudes are considered by the method. Each of the methods can be applied with respect to either the local bus voltage (i.e., the bus at which the PV inverter is located) or across all of

the bus voltages in the system. Without loss of generality, it is assumed that the PV inverter is located at buses n, $n+1$, and $n+2$, the three phases of the three-phase bus. If the local scope is used, only the voltage magnitudes at these three buses are considered. A selector matrix $\mathbf{S} \in \mathbb{R}^{3\times m}$ is constructed such that all elements are zero except for the $(1,n)$, $(2,n+1)$, and $(3,n+2)$ elements, which are unity. A local bus voltage magnitude vector is then constructed as

$$\mathbf{V}_l = \mathbf{S}\mathbf{V}. \tag{6.14}$$

Similarly, local sensitivity factors can be calculated:

$$\boldsymbol{\alpha}_{Pl} = \mathbf{S}\boldsymbol{\alpha}_P \tag{6.15}$$

$$\boldsymbol{\alpha}_{Ql} = \mathbf{S}\boldsymbol{\alpha}_Q. \tag{6.16}$$

A method with local scope uses the local bus voltage magnitude vector and the local sensitivity factors, while a method with global scope uses the global bus voltage magnitude vector and the global sensitivity factors.

6.1.2 Sensitivity Minimization vs. Violation Optimization Objective

The objective of a method indicates what criterion is used to select $\boldsymbol{\beta}$. The sensitivity minimization objective is to minimize the response of the considered bus voltage magnitudes to solar power perturbations. From (6.13), this can be accomplished by selecting

$$\boldsymbol{\beta} = \arg\min_{\boldsymbol{\beta}} \left\| \frac{1}{3}\boldsymbol{\alpha}_P \begin{bmatrix} 1 & 1 & 1 \end{bmatrix}^{\mathrm{T}} + \boldsymbol{\alpha}_Q\boldsymbol{\beta} \right\|. \tag{6.17}$$

The violation optimization objective is to maximize the magnitude of solar power perturbation for which none of the considered bus voltage magnitudes leaves its ac-

ceptable range. The considered bus voltage magnitudes are required to fall within a range:

$$\mathbf{V}_- \leq \mathbf{V} \leq \mathbf{V}_+, \tag{6.18}$$

where $\mathbf{V}_-$ is a vector containing the voltage magnitude lower limits of the considered buses and $\mathbf{V}_+$ is a vector containing the voltage magnitude upper limits of the considered buses. It is assumed that this requirement is satisfied at the operating point $(\mathbf{P}^*, \mathbf{Q}^*)$. The voltage magnitude constraint corresponds to a requirement on the incremental bus voltage magnitudes:

$$\Delta\mathbf{V}_- \leq \Delta\mathbf{V} \leq \Delta\mathbf{V}_+, \tag{6.19}$$

where

$$\Delta\mathbf{V}_- = \mathbf{V}_- - \mathbf{V}^* \tag{6.20}$$

$$\Delta\mathbf{V}_+ = \mathbf{V}_+ - \mathbf{V}^*. \tag{6.21}$$

The voltage optimization objective can be accomplished by substituting (6.13) into (6.19):

$$\begin{aligned} &\boldsymbol{\beta} = \arg\max_{\boldsymbol{\beta}} |\Delta P_s| \\ &\text{such that } \Delta\mathbf{V}_- \leq \left(\frac{1}{3}\boldsymbol{\alpha}_P \begin{bmatrix} 1 & 1 & 1 \end{bmatrix}^{\mathrm{T}} + \boldsymbol{\alpha}_Q\boldsymbol{\beta}\right)\Delta P_s \leq \Delta\mathbf{V}_+. \end{aligned} \tag{6.22}$$

6.1.3 Balanced vs. Unbalanced Domain

The domain of a method indicates what values of $\boldsymbol{\beta}$ are considered in meeting the objective of the method. The balanced domain allows for injection of equal amounts

of reactive power into each of the PV inverter's phases. In this case, the vector of substitution rates can be expressed as

$$\boldsymbol{\beta} = \beta \begin{bmatrix} 1 & 1 & 1 \end{bmatrix}^{\mathrm{T}}. \tag{6.23}$$

The unbalanced domain allows for unbalanced injection of reactive power, so the vector of substitution rates to be arbitrary. It should be noted that three-phase, four-wire inverters are assumed throughout. This permits either balanced or unbalanced reactive power injection despite voltage imbalances.

6.1.4 Method Integration

Each of the methods below is described in terms of global vectors (e.g., $\mathbf{V}$) and sensitivity factors ($\boldsymbol{\alpha}_P$ and $\boldsymbol{\alpha}_Q$), which is appropriate for methods with a global scope. If a method has a local scope, the selector matrix $\mathbf{S}$ is used, and all global vectors and sensitivity factors are replaced with local vectors (e.g., $\mathbf{V}_l$) and local sensitivity factors ($\boldsymbol{\alpha}_{Pl}$ and $\boldsymbol{\alpha}_{Ql}$).

For a method with the sensitivity minimization objective and the balanced domain, substitution of (6.23) into (6.17) yields the following substitution rate:

$$\beta = \arg\min_{\beta} \left\| \frac{1}{3}\boldsymbol{\alpha}_P \begin{bmatrix} 1 & 1 & 1 \end{bmatrix}^{\mathrm{T}} + \beta \boldsymbol{\alpha}_Q \begin{bmatrix} 1 & 1 & 1 \end{bmatrix}^{\mathrm{T}} \right\| \tag{6.24}$$

$$= -\frac{1}{3} \left(\boldsymbol{\alpha}_Q \begin{bmatrix} 1 & 1 & 1 \end{bmatrix}^{\mathrm{T}} \right)^{\dagger} \boldsymbol{\alpha}_P \begin{bmatrix} 1 & 1 & 1 \end{bmatrix}^{\mathrm{T}}, \tag{6.25}$$

where † denotes the Moore-Penrose pseudoinverse.

For a method with the sensitivity minimization objective and the unbalanced domain, the vector of substitution rates is determined from (6.17):

$$\boldsymbol{\beta} = -\frac{1}{3}\boldsymbol{\alpha}_Q^{\dagger}\boldsymbol{\alpha}_P \begin{bmatrix} 1 & 1 & 1 \end{bmatrix}^{\mathrm{T}}. \tag{6.26}$$

For a method with the violation optimization objective and the balanced domain, substitution of (6.23) into (6.22) yields the following problem:

$$\beta = \arg\max_{\beta} |\Delta P_s| \tag{6.27}$$
$$\text{such that } \Delta \mathbf{V}_- \leq \left(\frac{1}{3}\boldsymbol{\alpha}_P \begin{bmatrix} 1 & 1 & 1 \end{bmatrix}^{\mathrm{T}} + \beta \boldsymbol{\alpha}_Q \begin{bmatrix} 1 & 1 & 1 \end{bmatrix}^{\mathrm{T}} \right) \Delta P_s \leq \Delta \mathbf{V}_+.$$

This problem can be solved using a line search method.

For a method with the violation optimization objective and the unbalanced domain, (6.22) can be solved using grid-based search techniques.

The methods herein are denoted using three letters. The first letter indicates the scope: 'L' is local, and 'G' is global. The second letter indicates the objective: 'S' is sensitivity minimization, and 'V' is violation optimization. The third letter indicates the domain: 'B' is balanced, and 'U' is unbalanced. For example, the global, sensitivity minimization, balanced method is denoted by GSB. As a benchmark, the method 0 indicates that no reactive power control is performed, i.e., $\boldsymbol{\beta} = \mathbf{0}$.

For the LSU method, there is generally a unique solution to

$$\frac{1}{3}\boldsymbol{\alpha}_P \begin{bmatrix} 1 & 1 & 1 \end{bmatrix}^{\mathrm{T}} + \boldsymbol{\alpha}_Q \boldsymbol{\beta} = \mathbf{0}. \tag{6.28}$$

If (6.4) remains a good approximation of the bus voltage magnitudes under changing solar power, the local bus voltage magnitudes will not change for any solar power variation. This means that the same value of $\boldsymbol{\beta}$ would result in the allowable ΔP_s being infinite in the LVU method. Therefore, the solutions to the LSU and LVU methods are identical, and the performance of both of these methods is identical as well.

6.2 Performance Metrics

To study the performance of the PV reactive power control methods on distribution system voltages, several performance metrics are employed. The performance metrics are calculated for buses in the set $M = \{1, 2, \ldots, m\}$ over the time interval $[0, T]$. All of the performance metrics are calculated with voltage magnitudes converted to a 120-V scale. To aid in defining the performance metrics, some functions are defined below. The absolute voltage magnitude violation of bus i at time t is

$$V_{vi}(t) = \max\{V_i(t) - V_{+i}, V_{-i} - V_i(t), 0\}, \tag{6.29}$$

where $V_i(t)$ is the voltage magnitude of bus i at time t and V_{+i} and V_{-i} are the upper and lower voltage magnitude limits of bus i, respectively. The violation indicator function for bus i, which is 1 if bus i is experiencing a voltage magnitude violation at time t and 0 otherwise, is defined as

$$q_i(t) = \begin{cases} 0 & \text{if } V_{vi}(t) = 0 \\ 1 & \text{if } V_{vi}(t) > 0. \end{cases} \tag{6.30}$$

The global violation indicator function can be expressed as

$$q(t) = 1 - \prod_{i=1}^{m}(1 - q_i(t)), \tag{6.31}$$

is 1 if any bus is experiencing a voltage magnitude violation at time t, and is 0 otherwise.

The performance metrics can be divided into two classes: those related to system voltage magnitude violations, violation metrics, and those related to system voltage magnitude deviations from the reference system voltage magnitudes, sensitivity metrics.

The following global violation metrics are employed in this study. The number of violated buses is the number of buses that experience a voltage magnitude violation, i.e.,

$$|\{i \in M : \exists t(i) \in [0,T] \text{ such that } q_i(t) = 1\}|. \tag{6.32}$$

The violation time is the time during which at least one bus experiences a voltage magnitude violation, i.e.,

$$\int_0^T q(t)\ dt. \tag{6.33}$$

The mean violation time indicates the mean over the buses of the time during which each bus experiences a voltage magnitude violation, i.e.,

$$\frac{1}{m}\sum_{i=1}^{m}\int_0^T q_i(t)\ dt. \tag{6.34}$$

The mean violation refers to the mean over the buses of the mean absolute voltage magnitude violation experienced by each bus, i.e.,

$$\frac{1}{m}\sum_{i=1}^{m}\frac{1}{T}\int_0^T V_{vi}(t)\ dt. \tag{6.35}$$

The maximum violation indicates the maximum absolute voltage magnitude violation experienced at any time by any bus, i.e.,

$$\max_{i\in\{1,2,\ldots,m\}}\ \max_{t\in[0,T]} V_{vi}(t). \tag{6.36}$$

Two global sensitivity metrics are defined below for use in this study. The mean variation is given by

$$\frac{1}{T}\int_0^T \sqrt{\frac{1}{m}\sum_{i=1}^{m}(V_i(t) - V_i^*)^2}\ dt, \tag{6.37}$$

where V_i^* is the reference voltage magnitude of bus i. The maximum variation is given by

$$\max_{t\in[0,T]} \sqrt{\frac{1}{m}\sum_{i=1}^{m}(V_i(t) - V_i^*)^2}. \tag{6.38}$$

Each of the performance metrics described above are global metrics, which means that they consider each of the bus voltage magnitudes in the system. It is also possible to consider the performance at only a given local bus. Two local sensitivity metrics are defined for analyzing the local performance. The local mean variation is given by

$$\frac{1}{T}\int_0^T \sqrt{\frac{1}{3}\sum_{i=1}^{3}(V_{li}(t) - V_{li}^*)^2}\ dt. \tag{6.39}$$

where $V_{li}(t)$ is the voltage magnitude of local bus i at time t and V_{li}^* is the reference voltage magnitude of local bus i. The local maximum variation is given by

$$\max_{t\in[0,T]} \sqrt{\frac{1}{3}\sum_{i=1}^{3}(V_{li}(t) - V_{li}^*)^2}. \tag{6.40}$$

The local mean and maximum variations are local analogs to the mean and maximum variation global sensitivity metrics.

6.3 Simulation Results

In order to investigate the performance of the various reactive power control methods, three cases based on the IEEE 123-bus feeder distribution system [93] are studied. The structure of IEEE 123-bus feeder distribution system is shown in Figure 6.1 [93]. The system nominal voltage is 4.16 kV, and it contains four voltage regulators, four capacitor banks, and unbalanced loads [93]. It is also known to have voltage drop problems that must be carefully managed [93]. A number of buses associated with open and closed switchgear are excluded from the global bus voltage magnitude

vector **V** because the buses are unloaded or have identical characteristics to adjacent buses. These buses are 135, 149, 152, 160, 197, 251, 350, 451, and 610. The three cases involve various levels of PV penetration located at various locations within the system. In the first case, a large PV source is concentrated at a single three-phase bus. In the second case, ten smaller PV sources are distributed in a fairly uniform manner throughout the system. In the final case, the ten smaller PV sources are more concentrated.

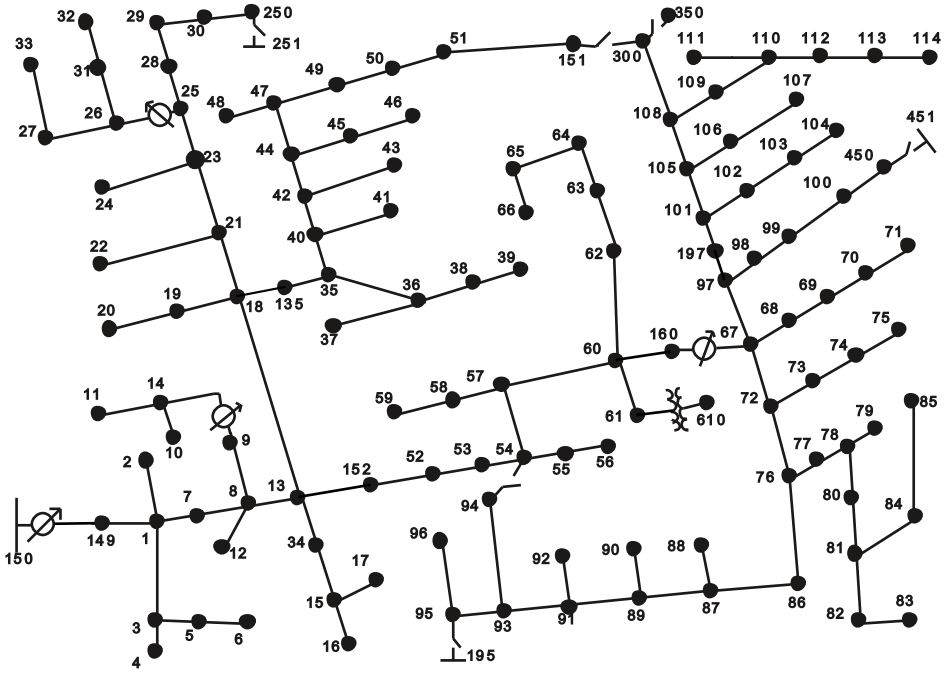

Figure 6.1: IEEE 123 Node Test Feeder [93]

The system is simulated for 15 minutes using PV output power derived from the global horizontal irradiance data collected at the National Renewable Energy Laboratory Solar Measurement Grid in Oahu, Hawaii. This measurement grid collects data at various nearby locations at 1-s intervals. The various sites at which data are collected are labeled DH1 through DH10, each corresponding to a different irradiance sensor placed in a different position. For the studies described herein, data from March 1, 2011 between 11:00 am and 11:15 am are used. The irradiance from several

of the sites is shown in Figure 6.2. It can be seen that the irradiance at these sites exhibits varying degrees of correlation on different time scales, and this correlation is expected in distribution systems in which the PV sources are near each other. It can also be seen that the irradiance can exhibit very rapid fluctuations due to cloud transients. This is consistent with previous observations of nearly 60%/s changes in irradiance [27]. Because MPPT algorithms are capable of converging to the correct maximum power point very quickly [94], it is appropriate to consider the effect of such rapid transients on distribution system voltages.

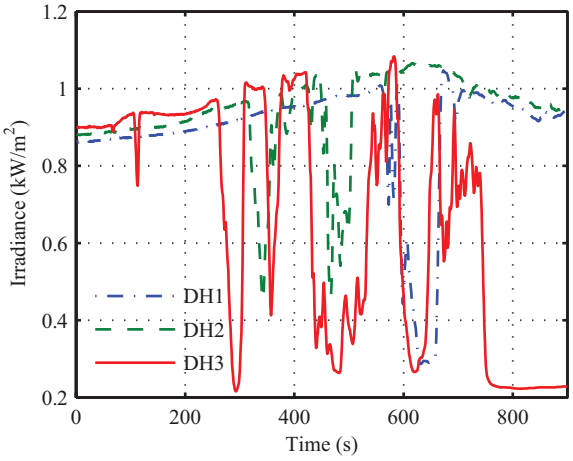

Figure 6.2: Sample irradiance data from studied interval

The parameters of the PV sources for the three cases are listed in Table 6.1. The solar power of a PV source is modeled by

$$P_s = \frac{S}{1000 \text{ W/m}^2} P_r, \tag{6.41}$$

where S is the irradiance and P_r is the rated solar power of the PV source when the irradiance is equal to 1000 W/m^2. The rated solar power for each PV source is listed in Table 6.1. During the 15-minute interval, the reference solar power P_s^* is taken to be the average solar power. This means that the reference solar power is

assumed to be correct over the interval and that any deviations ΔP_s are due solely to rapid solar fluctuations during the interval. By (6.11), the reference real power injection in each phase is one third of the reference PV solar power. While injecting reactive power on slower time scales has been proven to improve distribution system performance [72–78], the reference reactive power $\mathbf{Q}^*$ is assumed to be zero for these studies.

Table 6.1: Photovoltaic Source Parameters

Case	Source Number	Bus Location	Rated Solar Power	Irradiance Data Source
1	1	100	600 kW	DH3
2	1	1	200 kW	DH1
	2	21	200 kW	DH2
	3	35	200 kW	DH3
	4	49	200 kW	DH4
	5	55	200 kW	DH5
	6	63	200 kW	DH6
	7	76	200 kW	DH7
	8	82	200 kW	DH8
	9	93	200 kW	DH9
	10	101	200 kW	DH10
3	1	1	200 kW	DH1
	2	7	200 kW	DH2
	3	8	200 kW	DH3
	4	13	200 kW	DH4
	5	18	200 kW	DH5
	6	52	200 kW	DH6
	7	53	200 kW	DH7
	8	54	200 kW	DH8
	9	55	200 kW	DH9
	10	56	200 kW	DH10

Table 6.2: Voltage Regulator Tap Settings

Bus	150	9	25		160		
Phase	a,b,c	a	a	c	a	b	c
Case 1	7	-2	0	-1	8	2	3
Case 2	6	-3	0	-2	7	0	4
Case 3	5	0	1	0	8	3	5

The upper and lower voltage limits are assumed to be 126 V and 118 V, respectively, on a 120-V scale. Because PV sources are added in the distribution system, the tap settings of the voltage regulators must be adjusted to ensure that the system voltages are acceptable at the reference operating point. There are four voltage regulators in the distribution system. One of the regulators, at bus 150, regulates each of the three phases in a ganged manner. The other regulators control each phase independently. The regulators at buses 9, 25, and 160, affect one, two, and three phases, respectively. They are capable of 0.625% steps. The tap settings for the different regulators and the different cases are listed in Table 6.2. The reference voltages are calculated by using a modified version of the ladder iterative technique [95] and by assuming that the injected real and reactive power of PV sources are $\mathbf{P}^*$ and $\mathbf{Q}^*$, respectively. The sensitivity factors at the operating point are also calculated by using a modified version of the ladder iterative technique. When calculating the sensitivity factors for one phase of a PV source, the other two phases and the remaining PV sources are treated as constant (negative) PQ loads at the operating point. It is noted that the sensitivity factors and $\mathbf{V}^*$ are only calculated once for each of the 15 min simulations.

For each of the three cases, the system is simulated using the data given in Table 6.1. The solar power is calculated according to (6.41). The real and reactive power injections of each PV source are calculated using (6.10) and (6.1), respectively. The substitution rates $\boldsymbol{\beta}$ are calculated using each of the methods described above. The voltages at each time step are determined using a modified version of the ladder iterative technique [95]. Each of the global performance metrics defined above are calculated for each method. For Case 1, the local sensitivity performance metrics defined above are also calculated. The results from the cases are described in detail below.

6.3.1 Case 1

In Case 1, only one large PV source exists in the system. The performance metrics for this case are shown in Table 6.3. It can be seen that without the reactive power controller, the solar power variations cause significant effects in the distribution system. These effects include both significant voltage magnitude violations and significant deviations from the reference voltage magnitudes. Five buses experience voltage magnitude violations, and at least one bus experiences a voltage magnitude violation during more than half of the duration of the study. In terms of the violation performance metrics, it can be seen that the GVU method has the greatest improvement in performance, preventing any voltage magnitude violations from occurring. In terms of the sensitivity performance metrics, it can be seen that the GSU method performs the best; it reduces both the mean and maximum variations by more than 93%. For this case, which only has one PV source, the local sensitivity metrics described above are also calculated at the local three-phase bus associated with the PV source. For the local sensitivity metrics, the LSU method, which has identical performance to the LVU method as described above, is best. These methods reduce the mean local variation by more than 99% and the maximum local variation by more than 98%.

Table 6.3: Simulation Results for Case 1

Method	Number of Violated Buses	Violation Time (s)	Mean Violation Time (s)	Mean Violation (mV)	Maximum Violation (mV)	Mean Variation (mV)	Maximum Variation (mV)	Mean Local Variation (mV)	Maximum Local Variation (mV)
0	5	522	8.98	1.46	448	201	330	343	562
LSB	1	520	2.16	7.15×10^{-2}	49.0	25.7	43.8	25.7	42.5
LSU	1	519	2.15	4.35×10^{-2}	29.0	20.9	36.1	3.36	7.53
LVB	1	519	2.15	6.23×10^{-2}	42.4	25.2	42.3	26.1	41.9
LVU	1	519	2.15	4.35×10^{-2}	29.0	20.9	36.1	3.36	7.53
GSB	1	519	2.15	5.48×10^{-2}	37.1	25.0	41.6	27.4	42.8
GSU	1	110	0.456	2.16×10^{-4}	0.671	13.0	21.7	27.7	44.6
GVB	1	155	0.643	1.58×10^{-3}	3.41	32.8	51.3	54.1	86.2
GVU	0	0	0	0	0	13.2	22.9	25.5	40.5

6.3.2 Case 2

In Case 2, there are ten PV sources distributed throughout the system. When the substitution rates $\boldsymbol{\beta}$ for one of PV sources are calculated, the other PV sources are treated as negative constant PQ loads at the operating point. The performance metrics for this case are shown in Table 6.4. It can be seen that without the reactive power controller three buses experience voltage magnitude violations and at least one bus experiences a voltage magnitude violation during more than 64% of the duration of the study. In terms of the violation performance metrics, the four violation optimization methods have good performance. For these methods, no voltage violation is experienced by any bus. In terms of the sensitivity performance metrics, the GSU method has the best performance; it reduces the mean variation by more than 94% and the maximum variation by more than 95%.

Table 6.4: Simulation Results for Case 2

Method	Number of Violated Buses	Violation Time (s)	Mean Violation Time (s)	Mean Violation (mV)	Maximum Violation (mV)	Mean Variation (mV)	Maximum Variation (mV)
0	3	578	4.00	5.30×10^{-1}	376	172	605
LSB	1	1	0.00415	2.51×10^{-6}	0.545	26.7	90.7
LSU	0	0	0	0	0	15.9	49.6
LVB	0	0	0	0	0	26.9	91.9
LVU	0	0	0	0	0	15.9	49.6
GSB	1	2	0.00830	6.27×10^{-6}	0.764	25.7	90.7
GSU	1	3	0.0124	4.45×10^{-6}	0.648	9.77	29.5
GVB	0	0	0	0	0	38.6	114
GVU	0	0	0	0	0	24.8	74.8

6.3.3 Case 3

There are also ten PV sources in Case 3, but they are concentrated within the distribution system. As before, the other PV sources are treated as PQ loads when the substitution rates $\boldsymbol{\beta}$ for a given PV source are calculated. The performance metrics are shown in Table 6.5. Without the reactive power controller, 14 buses experience voltage magnitude violation. In terms of the violation performance metrics, it can be seen that the two global violation methods have good performance. For the global violation methods, only one bus experiences a voltage magnitude violation. Also, the

violation time is reduced by nearly 50%. The GVU method has the best performance for the violation metrics, reducing the maximum violation by more than 99% and the mean violation by more than 99.9%. The mean variation is reduced by the sensitivity minimization methods. The GSU method has the least mean variation, which is less than 3% of mean variation without reactive power control. The maximum variation is reduced by more than 98% by the GSU method.

Table 6.5: Simulation Results for Case 3

Method	Number of Violated Buses	Violation Time (s)	Mean Violation Time (s)	Mean Violation (mV)	Maximum Violation (mV)	Mean Variation (mV)	Maximum Variation (mV)
0	14	305	6.54	1.27	542	111	385
LSB	4	306	2.62	1.36×10^{-1}	137	25.3	89.5
LSU	1	374	1.55	1.31×10^{-2}	13.8	4.49	8.80
LVB	3	327	1.98	7.38×10^{-2}	90.5	27.4	93.8
LVU	1	374	1.55	1.31×10^{-2}	13.8	4.49	8.80
GSB	4	305	2.49	1.23×10^{-1}	129	25.2	89.0
GSU	1	374	1.55	6.63×10^{-3}	5.89	3.17	5.04
GVB	1	155	0.643	1.07×10^{-3}	3.77	41.8	141
GVU	1	146	0.606	9.41×10^{-4}	3.55	18.1	30.1

The voltage variation of the a phase of three-phase bus 65 with three different methods is shown in Figure 6.3 (a). Without reactive power control, the a phase of bus 65 has the largest maximum violation, dipping significantly below the 118-V lower limit. It can be seen that both the GVU and GSU methods keep the voltage magnitude very close to 118 V. Figure 6.3 (b) shows the voltage magnitude variation of these two methods more closely. It can be seen that the GSU method exhibits more frequent and more severe voltage magnitude violations, which corresponds to the results in Table 6.5. It can also be seen that the GSU actually increases the violation time, which is also consistent with Table 6.5.

6.3.4 Analysis

Several trends exist among the performance of the different reactive power control methods with respect to the various performance metrics. For the global violation performance metrics, i.e., number of violated buses, violation time, mean violation time, mean violation, and maximum violation, the methods with global scope and

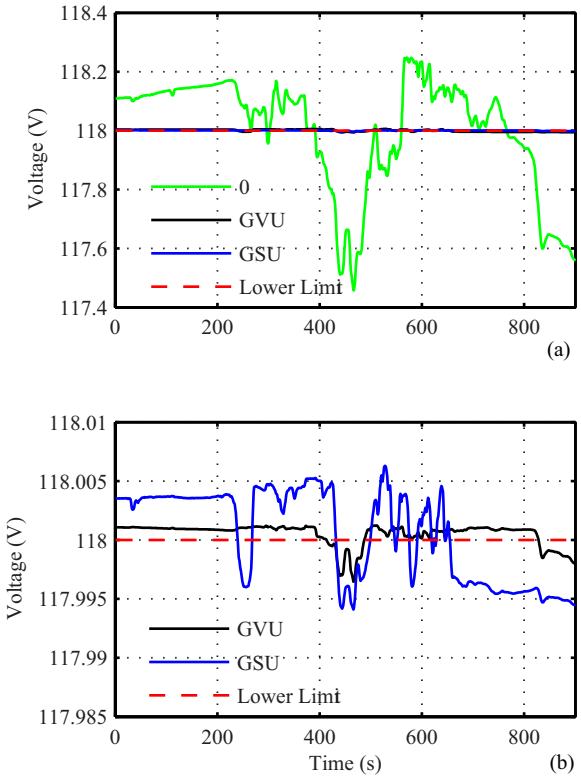

Figure 6.3: Case 3 bus 65 a-phase voltage magnitude. (a) 0, GVU and GSU methods; (b) GVU and GSU methods

violation optimization objective outperform the corresponding methods with either local scope or sensitivity minimization objective. Furthermore, GVU outperforms GVB. These relationships are illustrated in Figure 6.4. In this and the subsequent figures, an arrow indicates that the method at the origin outperforms the method at the destination. These relationships hold for each of the global violation performance metrics in each of the three cases as seen in Tables 6.3–6.5.

When the global sensitivity metrics, i.e., mean variation and maximum variation, are considered, the methods with global scope and sensitivity minimization objective outperform the corresponding methods with either local scope or the violation optimization objective. Once again, the method with unbalanced domain (GSU) exceeds

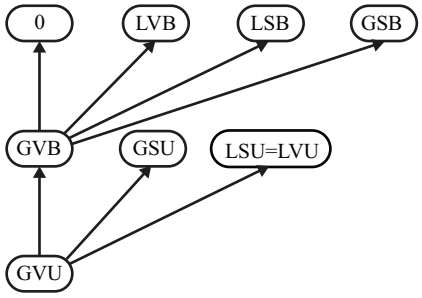

Figure 6.4: Global violation performance metrics relationships

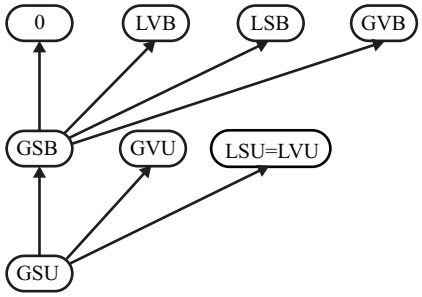

Figure 6.5: Global sensitivity performance metrics relationships

the performance of the method with balanced domain (GSB). The relationships of the methods for the global sensitivity metrics are shown in Figure 6.5. These relationships also hold for both of the global sensitivity performance metrics in each of the three cases as seen in Tables 6.3–6.5.

For the local sensitivity metrics, i.e., local mean variation and local maximum variation, the methods with local scope and sensitivity minimization objective outperform the corresponding methods with either global scope or the violation optimization objective. This excludes the relationship between the LSU and LVU methods, which are equal and have equal performance. The performance of the unbalanced LSU method is better than that of the balanced LSB method. The relationships for these metrics are presented in Figure 6.6. The local sensitivity metrics are not evaluated in Cases 2 and 3 because these cases have multiple PV sources. However, it can be seen in Table 6.3 that these relationships hold for both local sensitivity metrics in Case 1.

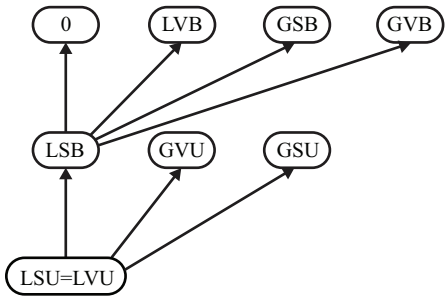

Figure 6.6: Local sensitivity performance metrics relationships

6.4 Conclusion

Various reactive power control methods that substitute reactive power output for real power output during solar power fluctuation are presented. These methods are intended to mitigate against voltage magnitude fluctuations due to short-term solar power variability. These methods are characterized by local or global scope, sensitivity minimization or violation optimization objective, and balanced or unbalanced domain. The various controllers are studied using the IEEE 123-bus feeder distribution system with three different cases, involving different degrees and distributions of PV penetration. Various global violation, global sensitivity, and local sensitivity metrics are considered. It is found that the reactive power control methods can effectively reduce voltage magnitude violation frequency and severity and voltage magnitude variation. Furthermore, it is seen that the best choice of reactive power control method depends on the choice of performance metric. Improvement of global violation performance metrics requires the use of global, violation optimization methods. If global sensitivity performance metrics are chosen, the use of global, sensitivity minimization methods are recommended. If only local sensitivity performance metrics are considered, local methods can be used. In all cases, it is found that the methods with unbalanced domain have better performance than the methods with balanced domain. Overall, it is found that the use of the proposed reactive power control methods can mitigate distribution system voltage magnitude fluctuations.

Chapter 7

Hybrid Position Observer for Brushless DC Motor Drives with Improved Noise Immunity

In this chapter, a noise immunity improvement for the hybrid position observer is proposed to address experimentally observed Hall-effect sensor noise. The work described in this chapter has been published in [96]. A finite state machine is used to detect Hall-effect sensor transitions to determine if these transitions are true transitions or the result of momentary glitches. This filter causes a delay in the detection of the Hall-effect sensors that is compensated in the proposed observer. The proposed observer is compared in simulations with the original hybrid position observer under both non-noisy and noisy conditions for both constant and variable speed operation. The simulation results show that the hybrid observer with noise immunity has good performance even under high noise and variable speed conditions.

The remainder of this chapter is organized as follows. A brief review of hybrid observer for brushless dc machines and the proposed noise immunity improvement

are described in Section 7.1. In Section 7.2, the proposed noise immunity method is compared with the original hybrid observer. A brief conclusion is given in Section 7.3.

7.1 Hybrid Observer with Noise Immunity

To introduce the noise immunity improvement for the hybrid position observer for brushless dc machines, a brief review of the hybrid observer [34] is described first. An example of the outputs of Hall-effect sensors 1–3 (HS1–3, respectively), the sine of the electrical rotor position s, and the cosine of the electrical rotor position c for a three-phase brushless dc machine are shown in Figure 7.1. It can be seen that there are six Hall-effect sensor states in one period, and s and c have specific values corresponding to each Hall-effect sensor transition. As a result, the exact value of the sine and cosine of the electrical rotor position can be determined at the moment of each Hall-effect sensor transition. Between the transitions, the instantaneous sine and cosine of the electrical rotor position can be estimated by

$$\frac{d\hat{c}}{dt} = -\hat{\omega}_r \hat{s} \tag{7.1}$$

$$\frac{d\hat{s}}{dt} = \hat{\omega}_r \hat{c}, \tag{7.2}$$

where $\hat{\omega}_r$ is the estimated electrical rotor speed, and $\hat{s}$ and $\hat{c}$ are the estimated sine and cosine of the electrical rotor position, respectively. By assuming the electrical rotor speed is a constant during each Hall-effect sensor state, $\hat{\omega}_r$ is estimated by

$$\hat{\omega}_r = \frac{\Delta\theta_r}{\Delta t}, \tag{7.3}$$

where $\Delta\theta_r$ is the electrical rotor angle difference between the current and previous transitions of the Hall-effect sensors and Δt is the time interval between the current and previous transitions. The values of s and c can be bounded in each sensor state

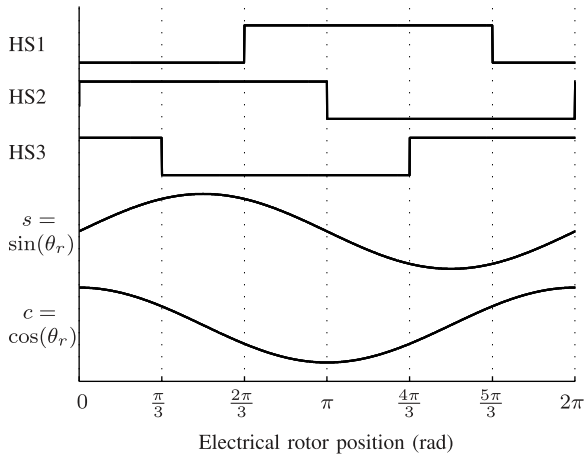

Figure 7.1: Relationship among Hall-effect sensor states and sine and cosine of electrical rotor position

to limit the estimation error between transitions, and the boundaries corresponding to each state can be obtained from Figure 7.1.

The hybrid observer has been shown to have good performance when no noise exists in the output of the binary Hall-effect sensors. However, once one of the output of Hall-effect sensors has a short glitch, the hybrid observer cannot estimate the rotor position correctly. Without any new glitches, this incorrect estimation takes several Hall-effect sensor transitions to disappear. Such sensor noise has been observed experimentally. In particular, the output of one of the Hall-effect sensors for an 8-hp brushless dc motor is shown in Figure 7.2 (a). It can be seen that a glitch occurs at approximately 85 ms, and this glitch is shown in closer proximity to the glitch in Figure 7.2 (b). This glitch lasts approximately 40 µs and can cause errors in rotor position estimation without an improvement in noise immunity.

Herein, a finite state machine is used to filter noise from a given Hall-effect sensor. The finite state machine maintains a Hall-effect state and a counter. The Hall-effect sensor output is sampled with a sampling time of t_{sample}. If the output is high, the counter is incremented, and the counter is decremented if the output is low. If the Hall-effect state was previously low and the counter reaches N, the Hall-effect state

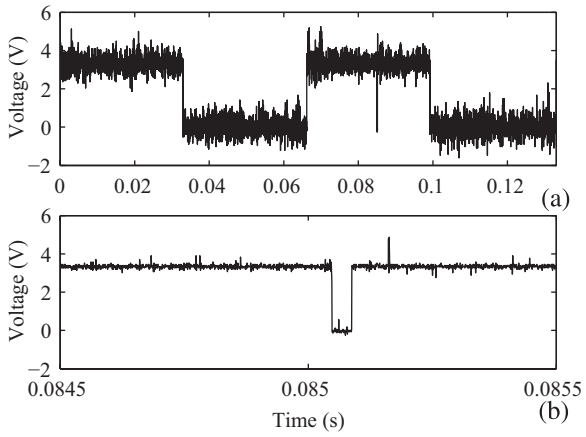

Figure 7.2: Experimentally observed Hall-effect sensor noise

transitions to high. Likewise, if the Hall-effect state was previously high and the counter reaches zero, the Hall-effect state transitions to low. The value of N is given by

$$N = \frac{t_g}{t_{sample}}. \tag{7.4}$$

In this way, detection of a Hall-effect state transition is delayed (on average by t_g), but false transitions are ignored. Such a state machine is implemented for each of the Hall-effect sensors.

The implementation of the state machines will reduce the effects of false Hall-effect sensor transitions, but it will also increase the delay of detecting true transitions. The hybrid position observer can be modified to compensate for this delay. In particular, the values to which the estimates of the sine and cosine of the rotor position should be reset must be adjusted based on the average transition delay t_g. If s^* and c^* represent the values of the sine and cosine at rotor position θ^* corresponding to a given Hall-effect sensor transition, the reset values when this transition is detected (i.e., t_g later than the actual transition) are calculated as

$$\hat{s} := \sin(\theta^* + \hat{\omega}_r t_g) \approx s^* + c^* \hat{\omega}_r t_g \tag{7.5}$$

$$\hat{c} := \cos(\theta^* + \hat{\omega}_r t_g) \approx c^* - s^* \hat{\omega}_r t_g, \tag{7.6}$$

Table 7.1: Reset Values

Transition	HS1	HS2	HS3	$\hat{s}$	$\hat{c}$
HS1	x	0	1	$-\frac{\sqrt{3}}{2}+\frac{1}{2}\hat{\omega}_r t_g$	$\frac{1}{2}+\frac{\sqrt{3}}{2}\hat{\omega}_r t_g$
HS1	x	1	0	$\frac{\sqrt{3}}{2}-\frac{1}{2}\hat{\omega}_r t_g$	$-\frac{1}{2}-\frac{\sqrt{3}}{2}\hat{\omega}_r t_g$
HS2	0	x	1	$\hat{\omega}_r t_g$	1
HS2	1	x	0	$-\hat{\omega}_r t_g$	-1
HS3	0	1	x	$\frac{\sqrt{3}}{2}+\frac{1}{2}\hat{\omega}_r t_g$	$\frac{1}{2}-\frac{\sqrt{3}}{2}\hat{\omega}_r t_g$
HS3	1	0	x	$-\frac{\sqrt{3}}{2}-\frac{1}{2}\hat{\omega}_r t_g$	$-\frac{1}{2}+\frac{\sqrt{3}}{2}\hat{\omega}_r t_g$

Table 7.2: Boundary of the Hall-effect Sensor State

State			$\hat{s}_{max}$	$\hat{s}_{min}$	$\hat{c}_{max}$	$\hat{c}_{min}$
HS1	HS2	HS3				
0	1	1	$\frac{\sqrt{3}}{2}+\frac{1}{2}\lvert\hat{\omega}_r\rvert t_g$	$-\lvert\hat{\omega}_r\rvert t_g$	1	$\frac{1}{2}-\frac{\sqrt{3}}{2}\lvert\hat{\omega}_r\rvert t_g$
0	1	0	1	$\frac{\sqrt{3}}{2}-\frac{1}{2}\lvert\hat{\omega}_r\rvert t_g$	$\frac{1}{2}+\frac{\sqrt{3}}{2}\lvert\hat{\omega}_r\rvert t_g$	$-\frac{1}{2}-\frac{\sqrt{3}}{2}\lvert\hat{\omega}_r\rvert t_g$
1	1	0	$\frac{\sqrt{3}}{2}+\frac{1}{2}\lvert\hat{\omega}_r\rvert t_g$	$-\lvert\hat{\omega}_r\rvert t_g$	$-\frac{1}{2}+\frac{\sqrt{3}}{2}\lvert\hat{\omega}_r\rvert t_g$	-1
1	0	0	$\lvert\hat{\omega}_r\rvert t_g$	$-\frac{\sqrt{3}}{2}-\frac{1}{2}\lvert\hat{\omega}_r\rvert t_g$	$-\frac{1}{2}+\frac{\sqrt{3}}{2}\lvert\hat{\omega}_r\rvert t_g$	-1
1	0	1	$-\frac{\sqrt{3}}{2}+\frac{1}{2}\lvert\hat{\omega}_r\rvert t_g$	-1	$\frac{1}{2}+\frac{\sqrt{3}}{2}\lvert\hat{\omega}_r\rvert t_g$	$-\frac{1}{2}-\frac{\sqrt{3}}{2}\lvert\hat{\omega}_r\rvert t_g$
0	0	1	$\lvert\hat{\omega}_r\rvert t_g$	$-\frac{\sqrt{3}}{2}-\frac{1}{2}\lvert\hat{\omega}_r\rvert t_g$	1	$\frac{1}{2}-\frac{\sqrt{3}}{2}\lvert\hat{\omega}_r\rvert t_g$

where the first-order approximations are suitable for microcontroller implementation because t_g is small. The values of $\hat{s}$ and $\hat{c}$ at each Hall-effect sensor transition are listed in Table 7.1, where x denotes the sensor in which a transition occurs.

In a similar way, the boundaries for $\hat{s}$ and $\hat{c}$ for each Hall-effect sensor state must be enlarged to account for the delay in detecting the transition to the next state. In particular, the electrical rotor position can be expected to exceed the boundary by $|\hat{\omega}_r|t_g$ before the next transition is detected. This boundary expansion is applied for both counterclockwise and clockwise rotation. The new boundaries for each Hall-effect sensor state can be estimated using a similar first-order approximation to that given in (7.5) and (7.6), and these boundaries are listed in Table 7.2, where $\hat{s}_{max}$ and $\hat{s}_{min}$ are the maximum and minimum value of estimated sine of electrical rotor position for each Hall-effect sensor state, respectively, and $\hat{c}_{max}$ and $\hat{c}_{min}$ are the maximum and minimum value of estimated cosine of electrical rotor position for each Hall-effect sensor state, respectively.

7.2 Simulation Results

Simulations of the responses of the original hybrid position observer and the proposed hybrid position observer are performed. The electrical rotor position θ_r is assumed to be differentiable. The true outputs of HS1–3 are high when $\cos(\theta_r - \frac{7\pi}{6})$, $\cos(\theta_r - \frac{\pi}{2})$, and $\cos(\theta_r - \frac{11\pi}{6})$ are positive, respectively. The sampling time for both observers is 100 kHz, and N for the proposed observer is 16. The initial value of the state variables $\hat{s}$, $\hat{c}$ are set to the correct initial values (i.e., those corresponding to the initial rotor position).

Two sets of studies are performed. In the first set, the rotor speed is constant, and the performance of the two observers is compared for both non-noisy and noisy conditions. In the second set, the rotor speed varies, and the performance is again compared for non-noisy and noisy conditions. The noise is modeled by the following process, which is applied independently to each of the three Hall-effect sensors. Glitches arrive according to an exponential distribution with mean time between the conclusion of the previous glitch and the arrival of the following glitch of 3 ms. The duration of each glitch is modeled by a uniform distribution between 0 ms and 0.15 ms. During a glitch, the observed output of the glitched Hall-effect sensor is the logical complement of the true output. In all of the simulation result figures, HS1–3 indicate the Hall-effect sensor outputs. s and c indicate the true sine and cosine of the electrical rotor position. $\hat{s}$ and $\hat{c}$ indicate the estimates of the sine and cosine of the electrical rotor position produced by the proposed observer. $\hat{s}_0$ and $\hat{c}_0$ indicate the estimates of the sine and cosine of the electrical rotor position produced by the original observer.

7.2.1 Steady-state performance

In the first set of studies, the electrical rotor speed is constant at 120π rad/s. The observers are simulated for two electrical periods. The results of the non-noisy case are shown in Figure 7.3. It can be seen that the sine and cosine estimates of the electrical rotor position from both hybrid observers are essentially identical and essentially identical with the true sine and cosine of the electrical rotor position in this case. The implementation of the proposed method has no detrimental effect on observer performance in this case. In particular, the delay in detecting the Hall-effect sensor transitions does not negatively affect the performance.

The simulation results under noisy conditions are shown in Figure 7.4. It can be seen that the original hybrid observer struggles with the noisy conditions throughout the simulation duration, producing estimates that are neither smooth nor correct at many times. It can also be seen that the sine and cosine estimates of the electrical rotor position by the proposed hybrid observer match the true values under these noisy conditions.

7.2.2 Transient performance

In the second set of studies, the electrical rotor speed is increased linearly from 40π rad/s to 160π rad/s over the 0.1-s simulation time. The results of the non-noisy case are shown in Figure 7.5. It can be seen that the sine and cosine estimates of the electrical rotor position from both hybrid observers are essentially identical. It can be seen that small errors exist between the two observers and the true sine and cosine of the electrical rotor position at lower speeds. These errors are unlikely to affect drive performance significantly.

The simulation results under noisy conditions are shown in Figure 7.6. The original hybrid observer cannot find the correct electrical rotor position during the transient

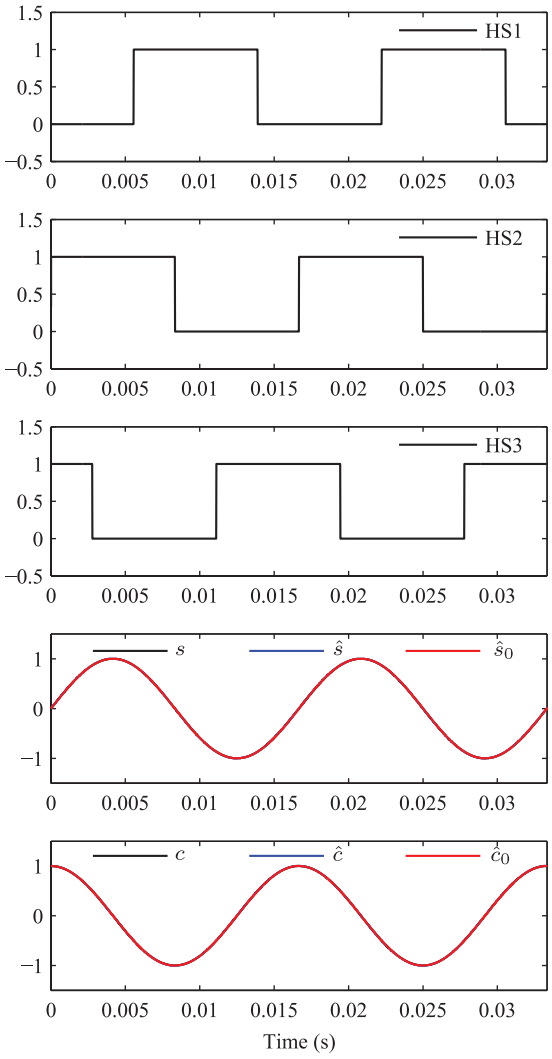

Figure 7.3: Simulation results with constant rotor speed and non-noisy conditions

at many times. The sine and cosine estimates of electrical rotor position estimated by proposed hybrid observer has good performance under these noisy conditions, matching the performance under non-noisy conditions.

7.3 Conclusion

A noise immunity improvement for hybrid position observers for brushless dc motor drives is proposed in this chapter. The proposed approach using finite state machines allows short glitches in the output of the Hall-effect sensors to be ignored. This

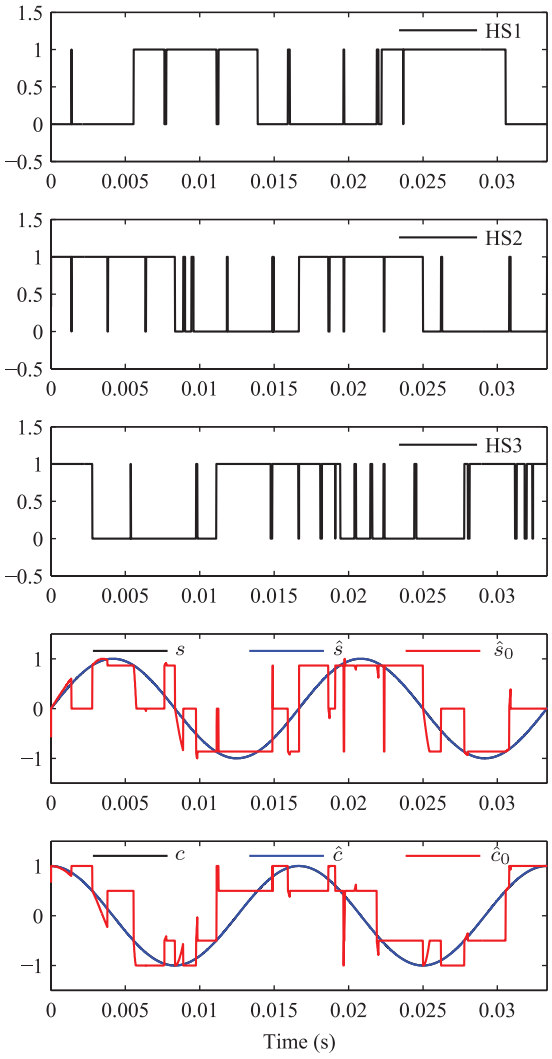

Figure 7.4: Simulation results with constant rotor speed and noisy conditions

improves noise immunity, but it also delays detection of Hall-effect sensor transitions, which is compensated in the proposed observer. The simulation results show that the proposed method has good performance under high noise conditions during steady-state and transient operation.

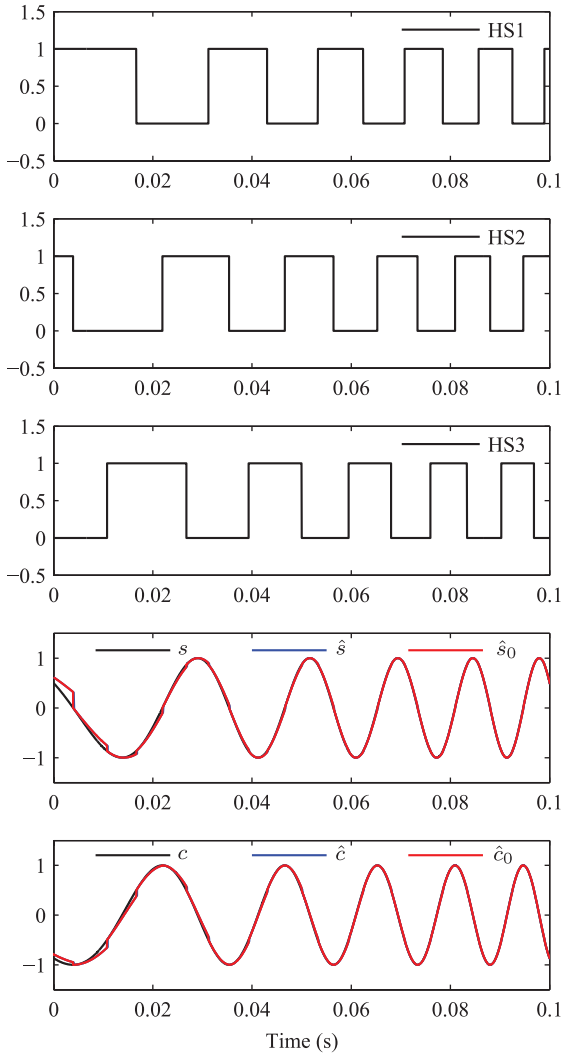

Figure 7.5: Simulation results with varying rotor speed and non-noisy conditions

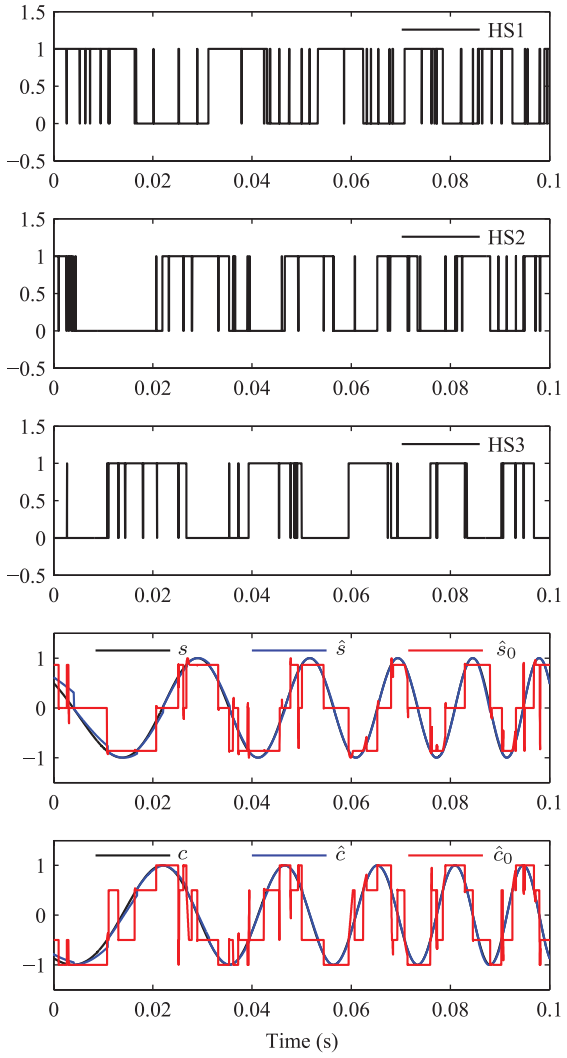

Figure 7.6: Simulation results with varying rotor speed and noisy conditions

Chapter 8

Conclusion and Future Work

8.1 Conclusion

In this dissertation, several topics about inverter control and modeling are discussed. The first three topics are about the implementation of GAM models for PWM inverters with different modulation signals in the *abc* variables and reference frames. The fourth topic is about controlling the reactive power output of the PV inverter system to reduce the grid voltage magnitude variations and violations due to the solar irradiance fluctuations. The fifth topic provides a noise immunity improvement for the Hall-effect sensor based electrical rotor position observer.

In Chapter 3, the GAM model for single- and three-phase PWM inverter is proposed. The average vector that contains the QFS coefficients of a waveform in the detailed model is used to represent the characteristics of such waveform in the GAM model. The QFS representation of switching functions and waveforms contains not only the fundamental component of the modulation signal and components corresponding to multiples of the switching frequency, but also sideband components of multiples of the switching frequency. The most significant harmonic components of the switching function can be found from the Fourier spectrum of the switching func-

tion. Because the QFS representation of switching function is known, the accuracy of the GAM model can be estimated based on the transfer function from the switching function to the signal of interest. Different configurations of GAM models are constructed by including different significant components to the average vector. Those configurations of GAM models are compared with the detailed models and SSA models in simulations. It is found that the simulation run times of GAM models are significantly smaller than those of detailed models and slightly larger than those of SSA models. The GAM models can portray the dynamic response of the fundamental components and switching frequency components of state variables. Experimental results are provided to demonstrate those models, and it is found that the simulation results from the GAM models match the experimental measurements in the steady state and transient.

In Chapter 4, a GAM model for three-phase PWM inverters with third-harmonic injection is proposed. The QFS representation of the switching functions with third-harmonic injection is provided. It is found that even the third-harmonic components are canceled in the balanced three-phase system, the third-harmonic injection changes the QFS coefficients of high-frequency components of state variables. Since QFS coefficients of high-frequency components of switching functions are the infinite sum, several terms are used to approximate the selected QFS coefficients of switching functions. The GAM model for the three-phase PWM inverter with third-harmonic injection is compared with a detailed model in simulations. It is found that the waveforms predicted by the GAM models match those predicted by the detailed model when the third harmonic is injected in the modulation signals. It is also found that the simulation run times of the GAM models are significantly faster than those associated with detailed models.

In Chapter 5, a GAM model in the reference frame for three-phase PWM inverters with varying modulation signal frequency is proposed. The QFS representation of

the switching functions with varying modulation signal frequency for *abc* variables is provided. And the QFS representation of the switching functions for the reference frame is derived from the transformation matrix and the QFS representation of the switching functions for *abc* variables. It is found that this transformation does not change the magnitude of the harmonic components. So, the significant components are selected to construct the average vector based on the Fourier spectrum of the switching function for *abc* variables. Two configurations of GAM models are compared with the detailed model in the rotor reference frame in simulations, and it is found that the *q*- and *d*-axis motor currents predicted by the GAM models match those predicted by the detailed model in the reference frame when the frequency and magnitude of the modulation signal are varying. Furthermore, the GAM models are found to have significantly faster simulation speeds than those associated with the detailed model in the reference frame. Hardware test results are also provided to demonstrate the proposed models, and it is found that the simulation results from the GAM model in the reference frame match the experimental measurements when the motor speed and reference current change.

In Chapter 6, different reactive power control methods that vary the reactive power output of the PV inverter system to mitigate voltage magnitude fluctuations due to short-term solar power variability are presented. The relationship among the variation of voltage magnitudes, the real output power of the PV inverter, and the reactive output power of the PV inverter is given by Taylor series expansion of voltage magnitude equations at the operating point. Based on this relationship, the reactive power control methods vary the reactive output power of PV inverter to reduce the voltage magnitude variation and violations. The reactive power control methods are defined by local or global scope, sensitivity minimization or violation optimization objective, and balanced or unbalanced domain to meet different performance requirements. To measure the system performance, various global violation, global sensitivity, and local

sensitivity metrics are provided. The reactive power control methods are implemented in the IEEE 123-bus feeder distribution system with three different cases, involving various numbers of PV sources and PV source locations. It is found that the reactive power control methods can effectively reduce voltage magnitude violation frequency by using the violation optimization methods. By using the sensitivity minimization methods, the voltage magnitude variation can be reduced. It is also found that the unbalanced domain methods are better than the balanced domain methods based on the performance metrics.

In Chapter 7, a hybrid position observer for brushless dc motor drives with a noise immunity improvement is proposed. The hybrid position observer estimates the electrical rotor position based on the state of the Hall-effect sensors. However, this hybrid position observer is very sensitive to the short glitches in the output of the Hall-effect sensors. The finite state machines are used to find the true state of the Hall-effect sensors and filter the short glitches. This improves noise immunity, but it causes a delay between detection of Hall-effect sensor transitions and the true Hall-effect sensor transitions. The reset value when the transitions are detected and the boundary of sine and cosine functions of electrical rotor position for each Hall-effect sensor state are modified to compensate this delay. This improvement is compared with the original observer in simulations. The simulation results show that the proposed method can find the correct electrical rotor position under high noise conditions during steady-state and transient operation.

8.2 Future Work

For the current source inverter, the state equation has the term that is a multiplication of the state variable and switching function. As mentioned before, the cross-coupling effect of the switching ripple can cause offsets in the low frequency components of the

state variable. In [53], the multiplication of the state variable and switching function for the GAM model of the boost converter are approximated by multiplying the dc and fundamental harmonic components of the state variable with those of the switching function. In the GAM model for the PWM inverter, this multiplication can cause offsets in the fundamental and switching frequency components of the state variable. However, the significant components in the inverter GAM model contain not only the fundamental component of the modulation signal and components corresponding to multiples of the switching frequency, but also sideband components of multiples of the switching frequency. The effect of this multiplication must be carefully considered for the current source inverter. The GAM model could be constructed for the current source inverter and can have significantly higher accuracy than the SSA model.

The finite element analysis (FEA) is commonly used to analyze and predict the behavior of the electrical machine [97–100]. It has high accuracy and is a useful tool to approximate the efficiency of the electrical machine. However, running the FEA is time consuming. It requires a large amount of computation for design optimization. In [101], a block model order reduction is implemented to reduce the simulation time of the FEA. The GAM inverter model can be used to generate the current waveform for the FEA. By doing this, simulation run time for the whole process can be reduced. Furthermore, the GAM may be applied to the finite element model. As a result, this FEA can provide an accurate approximation with fast simulation run time. However, the GAM must be adopted to model the nonlinearity of magnetic material and the cross-coupling effects in the magnetic field.

For reactive power control methods described in Chapter 6, the reactive power operating point for all of the PV sources are set to zero. The reactive power operating point can be set to a non-zero value. By using a non-zero value operating point, the average voltage magnitude of the distribution system can be changed and the power loss in the distribution system can be reduced. As a result, the reactive power control

methods can be used to improve the distribution system performance and reduce the voltage violation at the same time. Also, the reactive power operating point for each phase of each PV source could be different. By setting reactive power operating point for all PV sources, better performance can be achieved. The adaptive control method could be applied to find the substitution rates if the penetration of the PV panel is high. The substitution rates can be calculated by using the recursive least square method from previous electrical power changes and corresponding voltage magnitude changes.

Bibliography

[1] R. J. Wai and W. H. Wang, "Grid-connected photovoltaic generation system," *IEEE Trans. Circuits Syst. I, Reg. Papers*, vol. 55, no. 3, pp. 953–964, April 2008.

[2] C. Y. Yang, C. Y. Hsieh, F. K. Feng, and K. H. Chen, "Highly efficient analog maximum power point tracking AMPPT in a photovoltaic system," *IEEE Trans. Circuits Syst. I, Reg. Papers*, vol. 59, no. 7, pp. 1546–1556, July 2012.

[3] B. Liu, M. Su, J. Yang, D. Song, D. He, and S. Song, "Combined reactive power injection modulation and grid current distortion improvement approach for h6 transformer-less photovoltaic inverter," *IEEE Transactions on Energy Conversion*, vol. PP, no. 99, pp. 1–1, 2017.

[4] J. Giacomini, L. Michels, H. Pinheiro, and C. Rech, "Active damping scheme for leakage current reduction in transformerless three-phase grid-connected pv inverters," *IEEE Transactions on Power Electronics*, vol. PP, no. 99, pp. 1–1, 2017.

[5] D. S. Maric, S. Hiti, C. C. Stancu, J. M. Nagashima, and D. B. Rutledge, "An application of a constrained adaptive lattice-structure allpass-based notch filter for advanced control of surface-mounted permanent-magnet synchronous drives," *IEEE Trans. Circuits Syst. I, Fundam. Theory Appl.*, vol. 46, no. 12, pp. 1513–1516, Dec 1999.

[6] J. Zhang, J. Zhao, D. Zhou, and C. Huang, "High-performance fault diagnosis in PWM voltage-source inverters for vector-controlled induction motor drives," *IEEE Trans. Power Electron.*, vol. 29, no. 11, pp. 6087–6099, Nov 2014.

[7] G. Liu and K. Mao, "A novel power failure compensation control method for active magnetic bearings used in high-speed permanent magnet motor," *IEEE Trans. Power Electron.*, vol. 31, no. 6, pp. 4565–4575, June 2016.

[8] M. Hagiwara, K. Nishimura, and H. Akagi, "A medium-voltage motor drive with a modular multilevel pwm inverter," *IEEE Transactions on Power Electronics*, vol. 25, no. 7, pp. 1786–1799, July 2010.

[9] R. Gupta and A. Ghosh, "Frequency-domain characterization of sliding mode control of an inverter used in DSTATCOM application," *IEEE Trans. Circuits Syst. I, Reg. Papers*, vol. 53, no. 3, pp. 662–676, March 2006.

[10] J. D. Mondol, Y. G. Yohanis, and B. Norton, "Comparison of measured and predicted long term performance of grid a connected photovoltaic system," *Energ. Convers. Manage.*, vol. 48, no. 4, pp. 1065 – 1080, 2007.

[11] E. Mollerstedt and B. Bernhardsson, "Out of control because of harmonics-an analysis of the harmonic response of an inverter locomotive," *IEEE Control Syst. Mag.*, vol. 20, no. 4, pp. 70–81, Aug 2000.

[12] A. M. Cramer, X. Liu, Y. Zhang, J. D. Stevens, and E. L. Zivi, "Early-stage shipboard power system simulation of operational vignettes for dependability assessment," in *Electric Ship Technologies Symp. (ESTS), 2015 IEEE*, June 2015, pp. 382–387.

[13] S. Chiniforoosh, J. Jatskevich, A. Yazdani, V. Sood, V. Dinavahi, J. Martinez, and A. Ramirez, "Definitions and applications of dynamic average models for analysis of power systems," *IEEE Trans. Power Del.*, vol. 25, no. 4, pp. 2655–2669, Oct 2010.

[14] X. Liu, P. Wang, and P. C. Loh, "A hybrid ac/dc micro-grid," in *2010 Conf. Proc. IPEC*, Oct 2010, pp. 746–751.

[15] T. Mok, H. Liu, Y. Ni, F. F. Wu, and R. Hui, "Tuning the fuzzy damping controller for UPFC through genetic algorithm with comparison to the gradient descent training," *Int. J. Elec. Power*, vol. 27, no. 4, pp. 275–283, May 2005.

[16] R. Middlebrook and S. Ćuk, "A general unified approach to modelling switching-converter power stages," in *IEEE Power Electron. Specialists Conf.*, June 1976, pp. 18–34.

[17] A. Davoudi and J. Jatskevich, "Realization of parasitics in state-space average-value modeling of PWM dc-dc converters," *IEEE Transactions on Power Electronics*, vol. 21, no. 4, pp. 1142–1147, July 2006.

[18] A. Davoudi, J. Jatskevich, and T. D. Rybel, "Numerical state-space average-value modeling of PWM dc-dc converters operating in DCM and CCM," *IEEE Transactions on Power Electronics*, vol. 21, no. 4, pp. 1003–1012, July 2006.

[19] H. Kanaan, K. Al-Haddad, and F. Fnaiech, "Modelling and control of three-phase/switch/level fixed-frequency PWM rectifier: state-space averaged model," *IEE Proceedings - Electric Power Applications*, vol. 152, no. 3, pp. 551–557, May 2005.

[20] J. Mahdavi, A. Emadi, and H. A. Toliyat, "Application of state space averaging method to sliding mode control of pwm dc/dc converters," in *Industry Applications Conference, 1997. Thirty-Second IAS Annual Meeting, IAS '97., Conference Record of the 1997 IEEE*, vol. 2, Oct 1997, pp. 820–827 vol.2.

[21] N. Hoffmann, F. W. Fuchs, M. P. Kazmierkowski, and D. Schrder, "Digital current control in a rotating reference frame - part i: System modeling and the discrete time-domain current controller with improved decoupling capabilities," *IEEE Transactions on Power Electronics*, vol. 31, no. 7, pp. 5290–5305, July 2016.

[22] R. Bojoi, F. Farina, A. Tenconi, F. Profumi, and E. Levi, "Dual three-phase induction motor drive with digital current control in the stationary reference frame," *Power Engineer*, vol. 20, no. 3, pp. 40–43, June 2006.

[23] S. Shinnaka, "New sensorless vector control using minimum-order flux state observer in a stationary reference frame for permanent-magnet synchronous motors," *IEEE Transactions on Industrial Electronics*, vol. 53, no. 2, pp. 388–398, April 2006.

[24] R. Bojoi, E. Levi, F. Farina, A. Tenconi, and F. Profumo, "Dual three-phase induction motor drive with digital current control in the stationary reference frame," *IEE Proceedings - Electric Power Applications*, vol. 153, no. 1, pp. 129–139, Jan 2006.

[25] P. C. Krause, O. Wasynczuk, S. D. Sudhoff, and S. Pekarek, *Analysis of Electric Machinery and Drive Systems*. Piscataway, New Jersey: Wiley-IEEE Press, 2013.

[26] M. Lave, J. Kleissl, and E. Arias-Castro, "High-frequency irradiance fluctuations and geographic smoothing," *Solar Energy*, vol. 86, no. 8, pp. 2190–2199, 2012.

[27] W. Jewell and T. Unruh, "Limits on cloud-induced fluctuation in photovoltaic generation," *IEEE Trans. Energy Convers.*, vol. 5, no. 1, pp. 8–14, 1990.

[28] A. Darba, F. De Belie, and J. Melkebeek, "Sensorless commutation and speed control of brushless dc-machine drives based on the back-emf symmetric threshold-tracking," in *IEEE Int. Electric Machines Drives Conf.*, May 2013, pp. 492–497.

[29] P. Champa, P. Somsiri, P. Wipasuramonton, and P. Nakmahachalasint, "Initial rotor position estimation for sensorless brushless dc drives," *IEEE Trans. Ind. Appl.*, vol. 45, no. 4, pp. 1318–1324, July 2009.

[30] S. Bolognani, L. Ortombina, F. Tinazzi, and M. Zigliotto, "Model sensitivity of fundamental-frequency based position estimators for sensorless pm and reluctance synchronous motor drives," *IEEE Transactions on Industrial Electronics*, vol. PP, no. 99, pp. 1–1, 2017.

[31] G. Liu, S. Chen, S. Zheng, and X. Song, "Sensorless low-current start-up strategy of 100-kw bldc motor with small inductance," *IEEE Transactions on Industrial Informatics*, vol. 13, no. 3, pp. 1131–1140, June 2017.

[32] E. Zerdali and M. Barut, "The comparisons of optimized extended kalman filters for speed-sensorless control of induction motors," *IEEE Transactions on Industrial Electronics*, vol. 64, no. 6, pp. 4340–4351, June 2017.

[33] M. Harke, G. De Donato, F. Capponi, T. Tesch, and R. Lorenz, "Implementation issues and performance evaluation of sinusoidal, surface-mounted pm machine drives with hall-effect position sensors and a vector-tracking observer," *IEEE Trans. Ind. Appl.*, vol. 44, no. 1, pp. 161–173, Jan 2008.

[34] K. Corzine and S. Sudhoff, "A hybrid observer for high performance brushless dc motor drives," *IEEE Trans. Energy Convers.*, vol. 11, no. 2, pp. 318–323, Jun 1996.

[35] S. Morimoto, M. Sanada, and Y. Takeda, "Sinusoidal current drive system of permanent magnet synchronous motor with low resolution position sensor," in *IEEE IAS Annu. Meeting*, vol. 1, Oct 1996, pp. 9–14.

[36] Q. Ni, M. Yang, J. Long, and D. Xu, "Observer-based estimation improvement for servo control of pmsm with binary-type hall sensors," in *2017 IEEE Applied Power Electronics Conference and Exposition (APEC)*, March 2017, pp. 539–545.

[37] Y. Guan, J. M. Guerrero, X. Zhao, J. C. Vasquez, and X. Guo, "A new way of controlling parallel-connected inverters by using synchronous-reference-frame virtual impedance loop–part i: Control principle," *IEEE Transactions on Power Electronics*, vol. 31, no. 6, pp. 4576–4593, June 2016.

[38] P. Cheng and H. Nian, "Direct power control of voltage source inverter in a virtual synchronous reference frame during frequency variation and network unbalance," *IET Power Electronics*, vol. 9, no. 3, pp. 502–511, 2016.

[39] M. Monfared, S. Golestan, and J. M. Guerrero, "Analysis, design, and experimental verification of a synchronous reference frame voltage control for single-phase inverters," *IEEE Transactions on Industrial Electronics*, vol. 61, no. 1, pp. 258–269, Jan 2014.

[40] J. C. Vasquez, J. M. Guerrero, M. Savaghebi, J. Eloy-Garcia, and R. Teodorescu, "Modeling, analysis, and design of stationary-reference-frame droop-controlled parallel three-phase voltage source inverters," *IEEE Transactions on Industrial Electronics*, vol. 60, no. 4, pp. 1271–1280, April 2013.

[41] H. Sarnago, Ó. Lucía, A. Mediano, and J. Burdio, "Analytical model of the half-bridge series resonant inverter for improved power conversion efficiency and performance," *IEEE Trans. Power Electron.*, vol. 30, no. 8, pp. 4128–4143, Aug 2015.

[42] Z. Zou, Z. Wang, and M. Cheng, "Modeling, analysis, and design of multi-function grid-interfaced inverters with output LCL filter," *IEEE Trans. Power Electron.*, vol. 29, no. 7, pp. 3830–3839, July 2014.

[43] X. Ding, J. Poon, I. Čelanović, and A. D. Domínguez-García, "Fault detection and isolation filters for three-phase ac-dc power electronics systems," *IEEE Trans. Circuits Syst. I, Reg. Papers*, vol. 60, no. 4, pp. 1038–1051, April 2013.

[44] T. A. Sakharuk, A. M. Stankovic, G. Tadmor, and G. Eirea, "Modeling of PWM inverter-supplied ac drives at low switching frequencies," *IEEE Trans. Circuits Syst. I, Fundam. Theory Appl.*, vol. 49, no. 5, pp. 621–631, May 2002.

[45] N. Kroutikova, C. Hernandez-Aramburo, and T. Green, "State-space model of grid-connected inverters under current control mode," *IET Electr. Power App.*, vol. 1, no. 3, pp. 329–338, May 2007.

[46] A. Davoudi and J. Jatskevich, "Parasitics realization in state-space average-value modeling of PWM dc-dc converters using an equal area method," *IEEE Trans. Circuits Syst. I, Reg. Papers*, vol. 54, no. 9, pp. 1960–1967, Sept 2007.

[47] V. Moreno-Font, A. E. Aroudi, J. Calvente, R. Giral, and L. Benadero, "Dynamics and stability issues of a single-inductor dual-switching dc-dc converter," *IEEE Trans. Circuits Syst. I, Reg. Papers*, vol. 57, no. 2, pp. 415–426, Feb 2010.

[48] L. Han, J. Wang, and D. Howe, "State-space average modelling of 6- and 12-pulse diode rectifiers," in *2007 European Conference on Power Electronics and Applications*, Sept 2007, pp. 1–10.

[49] H. Behjati, L. Niu, A. Davoudi, and P. Chapman, "Alternative time-invariant multi-frequency modeling of PWM DC-DC converters," *IEEE Trans. Circuits Syst. I, Reg. Papers*, vol. 60, no. 11, pp. 3069–3079, Nov 2013.

[50] Z. Mihajlovic, B. Lehman, and C. Sun, "Output ripple analysis of switching dc-dc converters," *IEEE Trans. Circuits Syst. I, Reg. Papers*, vol. 51, no. 8, pp. 1596–1611, Aug 2004.

[51] D. Holmes and T. Lipo, *Pulse Width Modulation for Power Converters: Principles and Practice*. Piscataway, NJ: Wiley-IEEE Press, 2003.

[52] Y. Xu, Y. Chen, C.-C. Liu, and H. Gao, "Piecewise average-value model of PWM converters with applications to large-signal transient simulations," *IEEE Trans. Power Electron.*, vol. 31, no. 2, pp. 1304–1321, Feb 2016.

[53] V. Caliskan, G. C. Verghese, and A. Stanković, "Multifrequency averaging of dc/dc converters," *IEEE Trans. Power Electron.*, vol. 14, no. 1, pp. 124–133, Jan 1999.

[54] S. Sanders, J. Noworolski, X. Liu, and G. C. Verghese, "Generalized averaging method for power conversion circuits," *IEEE Trans. Power Electron.*, vol. 6, no. 2, pp. 251–259, Apr 1991.

[55] J. Mahdavi, A. Emaadi, M. Bellar, and M. Ehsani, "Analysis of power electronic converters using the generalized state-space averaging approach," *IEEE Trans. Circuits Syst. I, Fundam. Theory Appl.*, vol. 44, no. 8, pp. 767–770, Aug 1997.

[56] H. Qin and J. W. Kimball, "Generalized average modeling of dual active bridge dc-dc converter," *IEEE Trans. Power Electron.*, vol. 27, no. 4, pp. 2078–2084, April 2012.

[57] Z. Lin and H. Ma, "Modeling and analysis of three-phase inverter based on generalized state space averaging method," in *IECON 2013 - 39th Ann. Conf. of the IEEE Ind. Electron Soc.*, Nov 2013, pp. 1007–1012.

[58] C. Bernal, E. Oyarbide, P. Gaudó, and A. Mediano, "Dynamic model of class-E inverter with multifrequency averaged analysis," *IEEE Trans. Ind. Electron.*, vol. 59, no. 10, pp. 3737–3744, Oct 2012.

[59] R. A. Guinee and C. Lyden, "A novel fourier series time function for modeling and simulation of PWM," *IEEE Trans. Circuits Syst. I, Reg. Papers*, vol. 52, no. 11, pp. 2427–2435, Nov 2005.

[60] J. Smith, W. Sunderman, R. Dugan, and B. Seal, "Smart inverter volt/var control functions for high penetration of PV on distribution systems," in *2011 IEEE/PES Power Syst. Conference and Exposition*, 2011, pp. 1–6.

[61] D. Rizy, Y. Xu, H. Li, F. Li, and P. Irminger, "Volt/var control using inverter-based distributed energy resources," in *2011 IEEE Power and Energy Soc. General Meeting*, 2011, pp. 1–8.

[62] P. Jahangiri and D. Aliprantis, "Distributed volt/var control by PV inverters," *IEEE Transactions on Power Systems*, vol. 28, no. 3, pp. 3429–3439, Aug 2013.

[63] "Reactive power control on residential utility-interactive PV power systems," *Electric Power Systems Research*, vol. 51, no. 3, pp. 187 – 199, 1999.

[64] R. Yan, B. Marais, and T. K. Saha, "Impacts of residential photovoltaic power fluctuation on on-load tap changer operation and a solution using DSTATCOM," *Electric Power Systems Research*, vol. 111, no. 0, pp. 185 – 193, 2014.

[65] . Molina-Garca, R. A. Mastromauro, T. Garca-Snchez, S. Pugliese, M. Liserre, and S. Stasi, "Reactive power flow control for pv inverters voltage support in lv distribution networks," *IEEE Transactions on Smart Grid*, vol. 8, no. 1, pp. 447–456, Jan 2017.

[66] H. Li, Y. Xu, S. Adhikari, D. Rizy, F. Li, and P. Irminger, "Real and reactive power control of a three-phase single-stage PV system and PV voltage stability," in *2012 IEEE Power and Energy Soc. General Meeting*, 2012, pp. 1–8.

[67] N. Shah and R. Chudamani, "Single-stage grid interactive PV system using novel fuzzy logic based mppt with active and reactive power control," in *2012 7th IEEE Conference on Ind. Electron. and Applicat.*, 2012, pp. 1667–1672.

[68] S. Adhikari and F. Li, "Coordinated V-f and P-Q control of solar photovoltaic generators with MPPT and battery storage in microgrids," *IEEE Transactions on Smart Grid*, vol. 5, no. 3, pp. 1270–1281, May 2014.

[69] G. Tsengenes and G. Adamidis, "Investigation of the behavior of a three phase grid-connected photovoltaic system to control active and reactive power," *Electric Power Systems Research*, vol. 81, no. 1, pp. 177 – 184, 2011.

[70] A. Cagnano, E. De Tuglie, M. Liserre, and R. Mastromauro, "Online optimal reactive power control strategy of pv inverters," *IEEE Transactions on Industrial Electronics*, vol. 58, no. 10, pp. 4549–4558, Oct 2011.

[71] R. Aggarwal and Y. Pan, "Minimization of real power losses using reactive power control," *Electric Power Systems Research*, vol. 17, no. 2, pp. 153 – 157, 1989.

[72] T. Niknam, A. Ranjbar, and A. R. Shirani, "Impact of distributed generation on volt/var control in distribution networks," in *2003 IEEE Bologna Power Tech. Conference Proc.*, vol. 3, 2003, p. 7.

[73] T. Niknam, A. Ranjbar, A. R. Shirani, and A. Ostadi, "A new approach based on ant algorithm for volt/var control in distribution network considering distributed generators," *Iranian J. of Sci. & Technology, Trans. B, Eng.,*, vol. 29, no. B4, pp. 385–398, Aug. 2005.

[74] T. Senjyu, Y. Miyazato, A. Yona, N. Urasaki, and T. Funabashi, "Optimal distribution voltage control and coordination with distributed generation," *IEEE Trans. Power Del.*, vol. 23, no. 2, pp. 1236–1242, 2008.

[75] T. Niknam, "A new approach based on ant colony optimization for daily volt/var control in distribution networks considering distributed generators," *Energy Conversion and Manage.*, vol. 49, no. 12, pp. 3417–3424, 2008.

[76] T. Niknam, B. B. Firouzi, and A. Ostadi, "A new fuzzy adaptive particle swarm optimization for daily volt/var control in distribution networks considering distributed generators," *Applied Energy*, vol. 87, no. 6, pp. 1919 – 1928, 2010.

[77] S. Deshmukh, B. Natarajan, and A. Pahwa, "Voltage/var control in distribution networks via reactive power injection through distributed generators," *IEEE Trans. Smart Grid*, vol. 3, no. 3, pp. 1226–1234, 2012.

[78] K. Turitsyn, P. Šulc, S. Backhaus, and M. Chertkov, "Distributed control of reactive power flow in a radial distribution circuit with high photovoltaic penetration," in *2010 IEEE Power and Energy Soc. General Meeting*, 2010, pp. 1–6.

[79] S. Weckx, C. Gonzalez, and J. Driesen, "Combined central and local active and reactive power control of PV inverters," *IEEE Transactions on Sustainable Energy*, vol. 5, no. 3, pp. 776–784, July 2014.

[80] X. Liu, A. M. Cramer, and Y. Liao, "Reactive-power control of photovoltaic inverters for mitigation of short-term distribution-system voltage variability," in *2014 IEEE PES T D Conference and Exposition*, April 2014, pp. 1–5.

[81] M. Farivar, C. Clarke, S. Low, and K. Chandy, "Inverter var control for distribution systems with renewables," in *2011 IEEE Int. Conference on Smart Grid Commun.*, 2011, pp. 457–462.

[82] M. Farivar, R. Neal, C. Clarke, and S. Low, "Optimal inverter var control in distribution systems with high PV penetration," in *2012 IEEE Power and Energy Soc. General Meeting*, 2012, pp. 1–7.

[83] G. Pyo, H. W. Kang, and S. Moon, "A new operation method for grid-connected PV system considering voltage regulation in distribution system," in *2008 IEEE Power and Energy Soc. General Meeting - Conversion and Del. of Elect. Energy in the 21st Century*, 2008, pp. 1–7.

[84] K. Turitsyn, P. Šulc, S. Backhaus, and M. Chertkov, "Local control of reactive power by distributed photovoltaic generators," in *2010 First IEEE Int. Conference on Smart Grid Commun.*, 2010, pp. 79–84.

[85] ——, "Options for control of reactive power by distributed photovoltaic generators," *Proc. IEEE*, vol. 99, no. 6, pp. 1063–1073, 2011.

[86] W. Xiao, K. Torchyan, M. El Moursi, and J. Kirtley, "Online supervisory voltage control for grid interface of utility-level PV plants," *IEEE Transactions on Sustainable Energy*, vol. 5, no. 3, pp. 843–853, July 2014.

[87] G. Scelba, G. De Donato, G. Scarcella, F. Capponi, and F. Bonaccorso, "Fault-tolerant rotor position and velocity estimation using binary hall-effect sensors for low-cost vector control drives," *IEEE Trans. Ind. Appl.*, vol. 50, no. 5, pp. 3403–3413, Sept 2014.

[88] Y.-P. Yang and Y.-Y. Ting, "Improved angular displacement estimation based on hall-effect sensors for driving a brushless permanent-magnet motor," *IEEE Trans. Ind. Electron.*, vol. 61, no. 1, pp. 504–511, Jan 2014.

[89] X. Liu, A. M. Cramer, and F. Pan, "Generalized average method for time-invariant modeling of inverters," *IEEE Transactions on Circuits and Systems I: Regular Papers*, vol. 64, no. 3, pp. 740–751, March 2017.

[90] M. Ciobotaru, R. Teodorescu, and F. Blaabjerg, "A new single-phase PLL structure based on second order generalized integrator," in *2006. PESC '06. 37th IEEE Power Electron. Specialists Conf.*, June 2006, pp. 1–6.

[91] X. Liu and A. M. Cramer, "Three-phase inverter modeling using multifrequency averaging with third harmonic injection," in *2016 IEEE Energy Conversion Congress and Exposition (ECCE)*, Sept 2016, pp. 1–6.

[92] X. Liu, A. M. Cramer, and Y. Liao, "Reactive power control methods for photovoltaic inverters to mitigate short-term voltage magnitude fluctuations," *Electric Power Systems Research*, vol. 127, pp. 213 – 220, 2015.

[93] W. Kersting, "Radial distribution test feeders," in *2001. IEEE Power Eng. Soc. Winter Meeting*, vol. 2, 2001, pp. 908–912.

[94] E. Bianconi, J. Calvente, R. Giral, E. Mamarelis, G. Petrone, C. Ramos-Paja, G. Spagnuolo, and M. Vitelli, "A fast current-based mppt technique employing sliding mode control," *IEEE Transactions on Industrial Electronics*, vol. 60, no. 3, pp. 1168–1178, March 2013.

[95] W. Krause, *Distribution System Modeling and Analysis*. Boca Raton, Florida: CRC Press, 2001.

[96] X. Liu and A. M. Cramer, "Hybrid position observer for brushless dc motor drives with improved noise immunity," in *2016 IEEE Power and Energy Society General Meeting (PESGM)*, July 2016, pp. 1–5.

[97] X. Wang, T. D. Strous, D. Lahaye, H. Polinder, and J. A. Ferreira, "Modeling and optimization of brushless doubly-fed induction machines using computationally efficient finite-element analysis," *IEEE Transactions on Industry Applications*, vol. 52, no. 6, pp. 4525–4534, Nov 2016.

[98] Z. Ling, L. Zhou, S. Guo, and Y. Zhang, "Equivalent circuit parameters calculation of induction motor by finite element analysis," *IEEE Transactions on Magnetics*, vol. 50, no. 2, pp. 833–836, Feb 2014.

[99] R. Nasiri-Zarandi and M. Mirsalim, "Finite-element analysis of an axial flux hysteresis motor based on a complex permeability concept considering the saturation of the hysteresis loop," *IEEE Transactions on Industry Applications*, vol. 52, no. 2, pp. 1390–1397, March 2016.

[100] V. Ruuskanen, J. Nerg, M. Rilla, and J. Pyrhnen, "Iron loss analysis of the permanent-magnet synchronous machine based on finite-element analysis over the electrical vehicle drive cycle," *IEEE Transactions on Industrial Electronics*, vol. 63, no. 7, pp. 4129–4136, July 2016.

[101] T. Shimotani, Y. Sato, T. Sato, and H. Igarashi, "Fast finite-element analysis of motors using block model order reduction," *IEEE Transactions on Magnetics*, vol. 52, no. 3, pp. 1–4, March 2016.

Vita

Author's Name

Xiao Liu

Education

Yangtze University, B.S. awarded June 2009

University of Kentucky, M.S. awarded Dec. 2013

Publications

Xiao Liu and Aaron M. Cramer, "Inverter power control to support distribution system voltage variability mitigation," 2014 IEEE Energy Conversion Congress and Exposition (ECCE), Pittsburgh, PA, 2014, pp. 689-694.

Xiao Liu, Aaron M. Cramer and Yuan Liao, "Reactive-power control of photovoltaic inverters for mitigation of short-term distribution-system voltage variability," 2014 IEEE PES TD Conference and Exposition, Chicago, IL, USA, 2014, pp. 1-5.

Xiao Liu, Aaron M. Cramer and Yuan Liao, "Reactive power control methods for photovoltaic inverters to mitigate short-term voltage magnitude fluctuations," Electric Power Systems Research, Volume 127, October 2015, pp. 213-220.

Xiao Liu and Aaron M. Cramer, "Hybrid position observer for brushless dc motor drives with improved noise immunity," 2016 IEEE PES General Meeting, July 2016,

pp. 1–5.

Xiao Liu and Aaron M. Cramer, "Three-phase inverter modeling using multifrequency averaging with third harmonic injection," 2016 IEEE Energy Conversion Congress and Exposition (ECCE), Sept 2016, pp. 1–6.

Xiao Liu, Aaron M. Cramer and Fei Pan, "Generalized average method for time-invariant modeling of inverters," IEEE Transactions on Circuits and Systems I: Regular Papers, vol. 64, no. 3, pp. 740–751, March 2017.

Xiao Liu, Aaron M. Cramer, Vandana Rallabandi, Dan M. Ionel, "Switching Frequency Selection for Ultra-Low-Inductance Machines," 2017 IEEE International Electric Machines and Drives Conference, accepted.

Aaron M. Cramer, Xiao Liu, Yuqi Zhang, John D. Stevens and Edwin L. Zivi, "Early-stage shipboard power system simulation of operational vignettes for dependability assessment," 2015 IEEE Electric Ship Technologies Symposium (ESTS), Alexandria, VA, 2015, pp. 382-387.

Hanling Chen, Aaron M. Cramer and Xiao Liu, "Average-value modeling of hysteresis current controlled three-phase inverters," Electric Power Components and Systems, Volume 44, March 2016, pp. 693-700.